Analyzing and Optimizing the Process of Single Photon Collection

Matthias Manfred Seubert

Munich 2020

Analyzing and Optimizing the Process of Single Photon Collection

Matthias Manfred Seubert

Master-Thesis
at the Faculty of Physics
of the Ludwig-Maximilians-Universität München

Supervised by Prof. Dr. Harald Weinfurter
at the chair of Prof. Dr. Theodor W. Hänsch

handed in by
Matthias Manfred Seubert
born in Aschaffenburg

Munich, 13.06.2020

Analyse und Optimierung der Sammlung von Einzelphotonen

Matthias Manfred Seubert

Masterarbeit
an der Fakultät für Physik
der Ludwig-Maximilians-Universität München

Betreut durch Prof. Dr. Harald Weinfurter
am Lehrstuhl von Prof. Dr. Theodor W. Hänsch

vorgelegt von
Matthias Manfred Seubert
geboren in Aschaffenburg

München, den 13.06.2020

Acknowledgments

First of all I would like to thank Prof. Harald Weinfurter for giving me the opportunity to be part of his group and work on this interesting topic. The atmosphere in his group was very pleasant at all times which led to a close cooperation.
I want to pronounce my deep gratitude to Robert Garthoff. He supported me in all parts of this thesis. It was always a harmonic and complementary collaboration with a lot of revelatory discussions. His valuable contribution led to the current shape of this thesis.
Furthermore, I am deeply grateful for the support of Martin Zeitlmair and the acceptance in his office. Even after several failures in producing a point source, he never resigned. Without his commitment the characterization in the current shape would have been impossible.
A special thank goes to Dr. Wenjamin Rosenfeld. Especially at the early stage of the thesis, he supported me with his expertise in physical understanding. His contribution was the foundation for further development of the collection and coupling efficiency simulation.
Particularly at the final stage of the thesis, Florian Fertig provided valuable feedback on previous drafts of this work. I am truly thankful for his support.
Moreover, I am much obliged to all other group members of the atom experiment: Kai Redeker, Tim van Leent, Wei Zhang, Derya Taray and Sebastian Eppelt. The collaboration was especially marked by a surpassing cooperativeness.
My thanks also goes to my colleagues of the XQP group for an enjoyable time and a productive working environment.
Additionally, I want to thank my fellow students, in particular Maximilian Feil, Martin Grundner, Tim Höhn, Sonja Gerlach and Benjamin Tilmann for their support, honest feedback and the beautiful time.
An indescribable contribution was made by Elisa Linnenbrink. She made always time available for me, encouraged and supported me whenever possible. I am deeply grateful for this.
Finally I would like to express my deep gratitude to my family and friends for their great encouragement and support at every time.

Contents

Chapter 1

Introduction and motivation

The development of quantum mechanics in the 1920s and early 1930s [1, 2] enables a consistent description of the spectrum of black-body radiation [3] or wave-particle dualism [4]. However, this formalism shocked the physical society as it introduced new concepts with no counterpart in classical physics: the uncertainty principle, superposition and entanglement. Especially the abandonment of locality and realism as an inherent property of a physical theory led to controversial discussions. A prominent example are the Bohr-Einstein debates and even more the EPR paradox in 1935 [5]. According to Einstein, Podolsky and Rosen, quantum mechanics is incomplete and must be extended by local hidden variables to maintain local realism. However, in 1964, John Bell proposed the first approach to experimentally distinguish local realistic from other theories by the so-called Bell's inequality [6]. Clauser, Horne, Shimony and Holt reformulated this inequality providing a feasible implementation in experiments. Quite recently, a violation of Bell's inequality was demonstrated closing all major loopholes [7–10].

During the last century, quantum mechanics was established as a fundamental theory to describe the nature on an atomic scale. After the first quantum revolution, scientists started to investigate the enormous potential of the unique features of quantum mechanics and implemented them in a completely new field of research, quantum information science. Physicists like Feynman [11] or Deutsch [12] started to investigate whether quantum systems can be used to perform computations. First quantum algorithms developed by Shor [13] and Grover [14] revealed that a potential quantum computer can perform certain calculations faster than any classical computer. Another application is the concept of quantum cryptography. By the principle of quantum mechanics, it is impossible for an eavesdropper to perfectly copy information [15]. Therefore, quantum key distribution (QKD), implemented for example with BB84 protocol [16], provides for the first time the possibility to measure the potential information an eavesdropper could have and thereby enables a feasible and secure way of communication.

An essential part of all applications of quantum information science is a high degree of controlling single quantum systems. Back in 1952, it was even unimaginable for Schrödinger to handle single particles: "[...] we never experiment with just one electron or atom or (small) molecule. In thought-experiments we sometimes assume that we do; this invariably entails

ridiculous consequences [...]" [17]. However, within a few decades, it was possible to isolate single ions [18] or neutral atoms [19] in magnetic traps. Moreover, the invention of the laser by Theodore Maiman in 1960 provides perhaps the most powerful tool to control quantum systems. Laser cooling techniques and the optical dipole traps (ODTs) set the new benchmark for quantum applications.
To tap the full potential of quantum information science, it is necessary to combine various applications within a quantum network [20]. A quantum network relies on the faithful mapping of quantum information between a stationary quantum memory and a reliable quantum communication channel. By stacking together several quantum memories connected via quantum channels, it is possible to carry out quantum teleportation [21] or quantum communication schemes [22, 23]. Besides nitrogen-vacancy centers [24], quantum dots [25] or ions, neutral atoms isolated in an ODT are an ideal resource of stable storages [10]. Usually, quantum information is transmitted by photons since they can overcome long distances easily by optical fibers or free-space propagation. The information of the quantum state is encoded in photon number, time bins or the polarization state. Due to lack of interaction between photons, long coherence times are guaranteed.
In recent years, scientists pushed the knowledge of nearly every application of quantum information science. Building blocks of quantum networks grew from several meters up to kilometers and more [26, 27]. Chinese scientists launched a satellite to perform QKD between ground states in Austria and China [28, 29]. Multi qubit nodes [30, 31] are investigated to realize quantum repeaters [32] which extend the distance of quantum channels. Hybrid system nodes potentially allow distributed quantum computing to overcome technical difficulties in scaling up the number of qubits [33]. Quantum computing reached a new level by outperforming classical computers for specific tasks [34]. All these investigations aimed towards one dream, a quantum internet [35]. We are right in the middle of the second quantum revolution [36], developing quantum technology towards application.
The experiment described in this thesis represents a building block of a quantum network, where two spatially separated neutral ^{87}Rb atoms operate as quantum memories connected by an optical fiber link. Entanglement between an atomic spin state and photonic polarization state generated by spontaneous decay combines the transmission and storage capability of quantum information. The information transfer between the separated atoms is provided by the entanglement swapping protocol [23]. In this process, the atom-atom entanglement rate limits the distance between both quantum memories. To increase the distance ($\sim 700\,\mathrm{m}$) of the current setup, it is mandatory to analyze and optimize the collection process of the single emitted photons. Hence, a new optical collection setup is implemented, containing a custom designed objective with a numerical aperture of 0.5.
This thesis is structured as follows. First of all, the functionality of the experiment is described in detail and the limitation towards long-distance entanglement is outlined. In Chapter 3, the process of collecting single photons and coupling them into a single-mode fiber is investigated. This leads to the development of a self-made fiber collimator. Since wave aberrations of involved optical systems would restrict the coupling efficiency, the objective and fiber collimator are fully characterized in Chapter 4. Finally in Chapter 5 the implementation of the new setup and its increase of performance is analyzed and discussed.

Chapter 2

Towards long-distance entanglement of atomic qubits

Heralded generation of entanglement between atomic qubits over long distances is a complex process, requiring well controlled quantum systems. This chapter introduces the experimental methods and theoretical concepts, developed in the last 20 years, for achieving entangled single atoms trapped in two separate laboratories 398 m apart. For feasible quantum communication applications, this distance must be extended significantly. Here, the current limitations and prospects of the experiment towards longer distances are described in this chapter.

2.1 The ^{87}Rb quantum system

To obtain long-distance entanglement of two atomic qubits, it is essential that a suitable quantum system satisfies the following requirements [37, 38]:

First of all, involved quantum systems must provide an opportunity to distribute entanglement. It is convenient to entangle a stationary atomic qubit with a flying qubit, whose information is encoded in the polarization state of a single photon. These photons can faithfully be transmitted over long-distances via glass fibers.
During that transportation process, the entanglement between the stationary and flying qubit must persist. Hence, a long atomic coherence time is desirable for long-distance applications.
To prove and implement atom-atom entanglement in future quantum communication applications, a high fidelity read-out mechanism is necessary. Furthermore, for special applications like Bell tests [10], the read-out mechanism must be very fast to ensure space-like separation.

Since single, neutral ^{87}Rb fulfills all requirements, it is a possible candidate for quantum communication applications and is used in this experiment. Moreover, the alkali metal ru-

bidium has only one valence electron which leads to a simple and well-understood energy level structure [39]. The most important energy levels for this experiment are depicted in Figure 2.1.

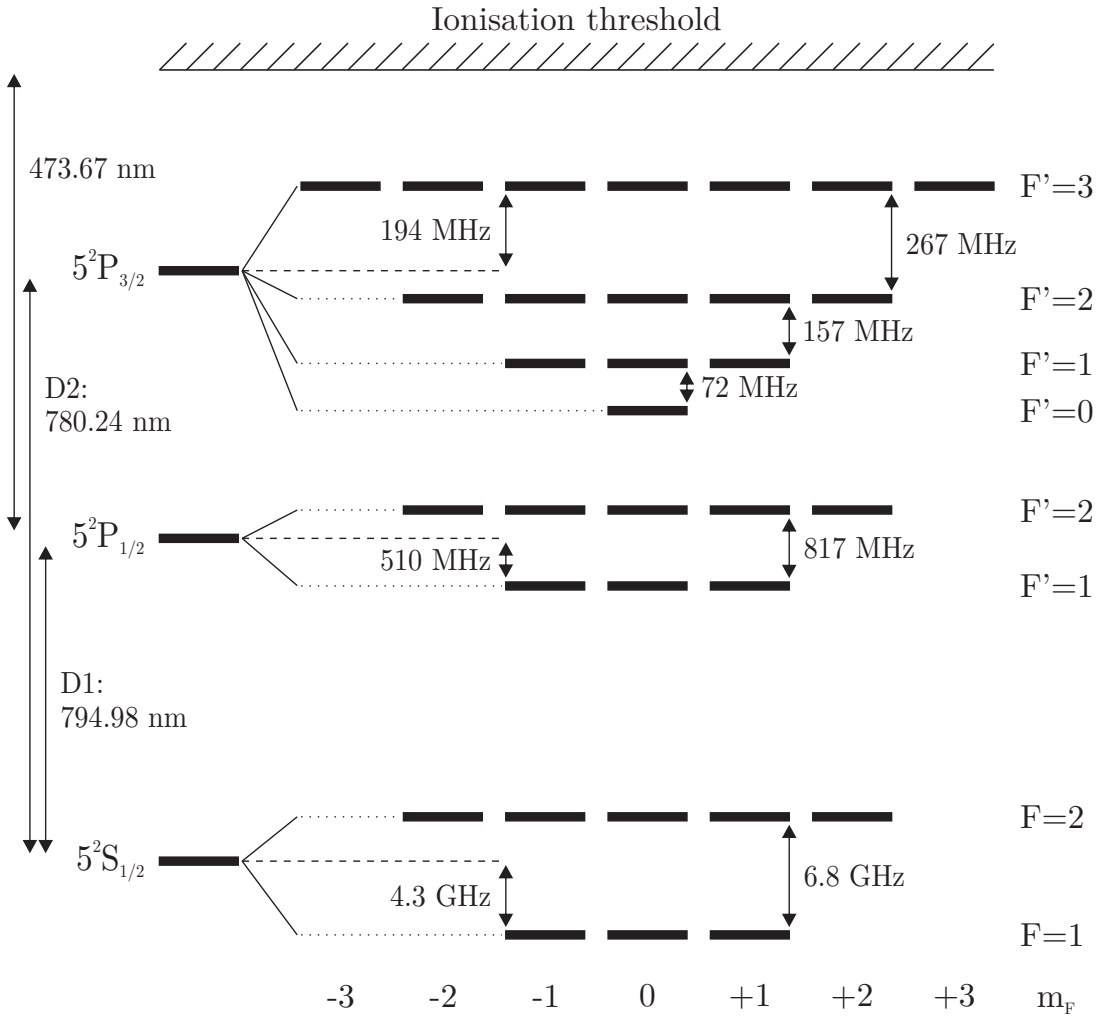

Figure 2.1: Relevant part of the energy level structure of ^{87}Rb for this experiment [39]. The $5^2S_{1/2}$ ground state splits into the hyperfine levels $F = 1, 2$. Due to fine structure and hyperfine structure splitting, the first excited state splits into the $5^2P_{1/2}$, $F' = 1, 2$ and $5^2P_{3/2}$, $F' = 0, 1, 2, 3$. Optical transitions from ground to excited states can be driven by laser beams with a wavelength of 794.98 nm and 780.24 nm. The stationary atomic qubit is encoded in the Zeeman substates $F = 1$, $m_F = \pm 1$ of the ground state.

The ground state of the single valence electron is the 5^2S state, the first excited state the 5^2P state. Due to fine structure splitting, the first excited state splits up into the two

sub-levels $5^2P_{1/2}$ and $5^2P_{3/2}$. Since all transitions from ground to first excited state are in the near-infrared regime, commercially available laser systems and optical components can be used without further effort. The nuclear spin of ^{87}Rb is I = 3/2, leading to a hyperfine splitting of F = 1, 2 for the ground state $5^2S_{1/2}$ and F' = 1, 2 respectively F' = 0, 1, 2, 3 for the first excited states $5^2P_{1/2}$ and $5^2P_{3/2}$. The single Zeeman substates are denoted by $|F, m_F\rangle$ in case of the ground state and $|J, F', m_{F'}\rangle$ for the excited states.

The pair of entangled stationary atomic qubit and flying qubit is generated by a spontaneous decay of the $|J = 3/2, F' = 0, m_{F'} = 0\rangle$ state to the $|F = 1, m_F = \pm 1\rangle$ levels, which together form a so-called $\Lambda-$system. This emission results in an entanglement of the polarization of the emitted photon and a stationary qubit encoded in the Zeeman substates $|F = 1, m_F = \pm 1\rangle$ (see Subsection 2.3.2). In absence of any magnetic and optical field, the sub-levels of the $5^2S_{1/2}$, F = 1 ground state are degenerate, which leads to long coherence times of the qubit. Due to dipole selection rules, a fast state-dependent read-out is possible (see Section 2.3.3). In addition, the closed transition $|J = 1/2, F' = 2, m_{F'} = +2\rangle \rightarrow |J = 3/2, F' = 3, m_{F'} = +3\rangle$ provides an efficient opportunity for laser cooling (see Subsection 2.2.2).

2.2 Trapping single ^{87}Rb atoms

Experiments on single atom quantum memories, i.e., the atomic qubit, require a single isolated, trapped and well-localized atom. Long coherence times of the atomic qubit are achieved by isolating the atom in an ultra-high vacuum (UHV) from any interaction with other atoms. For trapping a single atom, a two step scheme is realized: out of the background gas, ^{87}Rb atoms are trapped and laser cooled in a magneto-optical trap forming a cold cloud of atoms. From this cloud, a single atom is trapped in an optical dipole trap.

2.2.1 Laser systems and vacuum

The most important optical transitions, the D1 and D2 line at 794.98 nm respectively 780.24 nm, can be driven by commercially available diode lasers[1]. These diode lasers are frequency stabilized using an external resonator, created by an actively controlled grating [40] and Doppler-free saturation spectroscopy. To fine-tune the frequency of the light and address single hyperfine levels, acousto-optical modulators (AOMs) are used. An overview of the complete laser system and all used laser beams and transition frequencies can be found in Appendix A.
In this experiment the vacuum chamber allows pressures below $\sim 10^{-10}$ mbar. This ultra-high vacuum is maintained by an ion-getter pump[2], which leads to a sufficient isolation of the atom from the environment. The atom trap and therefore the position of the atom is located in a glass cell attached to the vacuum chamber, providing a good optical access for

[1] Toptica DL Pro.
[2] Varian/Agilent Vaclon Plus 55 Starcell.

the required laser beams. Moreover, particle detectors for state read-out and a rubidium dispenser are located inside the glass cell. Since rubidium atoms have deposited on the walls of the glass cell, they can be released with LED light in the ultraviolet regime without turning-on the vapor dispenser. This increases the lifetime of the dispenser and prevents the contamination of internal parts of the UHV setup. Further details about the structure of the vacuum setup can be found in [41, 42].

2.2.2 Magneto-optical trap

^{87}Rb atoms are released inside the glass cell by LED light which makes it mandatory to pre-cool atoms ($\sim 1\,\mathrm{mK}$) before loading the optical dipole trap. Nevertheless, slowing techniques, e.g. Zeeman slowers, are not necessary for trapping atoms in a magneto-optical trap (MOT). A MOT combines a compression force with the dissipative friction force of Doppler cooling which leads to a localized atom cloud with low thermal energy [43–45].

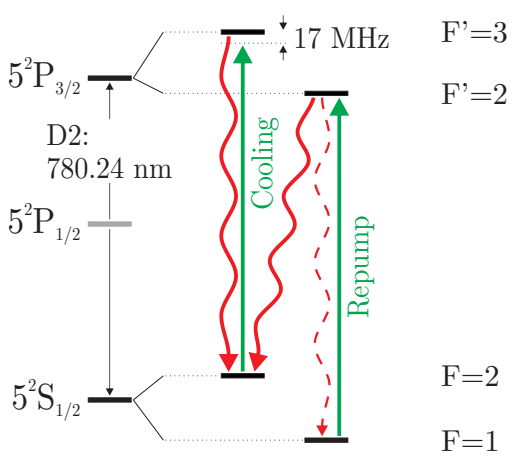

(a) The closed transition $5^2S_{1/2}$, F = 2 → $5^2P_{3/2}$, F' = 3 efficiently cools the atom by using a 17 MHz red detuned cooling laser beam. In case of an off-resonant excitation, the repump laser beam transfers atoms back to the cooling transition.

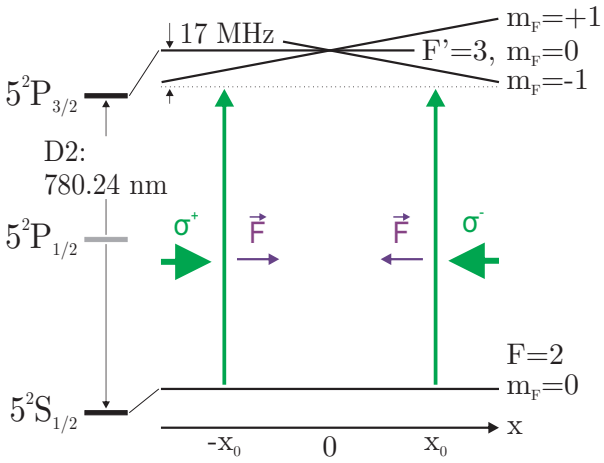

(b) Due to an inhomogeneous magnetic field, the $5^2P_{3/2}$, F' = 3 Zeeman substates are split depending on their location. σ^+ or σ^- polarized light is preferably absorbed at specific positions. This leads to a compression force.

Figure 2.2: Schematic of the two essential parts of a MOT: cooling and trapping for the example of ^{87}Rb.

The technique of Doppler cooling relies on a scattering force inducing a net momentum transfer. Due to the Doppler effect, the direction of this momentum transfer is preferentially opposed to the propagation direction of the atoms. By applying 3 orthogonal pairs

of counter-propagating, red detuned laser beams, a friction force in all three spatial dimensions is generated. This leads to a cooling effect [43, 46]. In case of the ^{87}Rb quantum system, laser beams red detuned by 17 MHz with regard to the $5^2S_{1/2}$, F = 2 $\rightarrow$ $5^2P_{3/2}$, F' = 3 transition are used [47]. This transition is a closed transition which allows efficient Doppler cooling. Due to off-resonant excitations into the $5^2P_{3/2}$, F' = 2 state, atoms can decay into the $5^2S_{1/2}$, F = 1 ground level. To maintain atoms in the cooling cycle, an additional repump laser beam is applied, which drives the transition $5^2S_{1/2}$, F = 1, $\rightarrow$ $5^2P_{3/2}$, F' = 2. This scheme is shown in Figure 2.2 (a). The achievable temperature limit for ^{87}Rb by Doppler cooling is 146 µK [39]. However, temperatures of about 30 µK were already realized in this experiment [47, 48]. A process called polarization gradient cooling [49] leads to temperatures below the Doppler limit.

The compression force of a MOT is generated by a spatial dependency of the friction force. This is achieved by applying a magnetic quadrupole field, i.e., a linearly inhomogeneous field, created by two coils in anti-Helmholtz configuration. The center of the quadrupole field is overlapped with the center of the atomic cloud. The quadrupole field leads to a spatially dependent Zeeman splitting. Due to angular momentum conservation, two counter-propagating beams with σ^+ respectively σ^- polarized light preferably excite atoms at specific spatial positions. Therefore, the scattering force is directed to the center of the trap leading to a confinement of the atoms (see Figure 2.2 (b)) [43]. It should be noted that σ^+ or σ^- polarized light is defined with respect to the quantization axis. In regions of negative magnetic fields, the quantization axis is flipped and σ^- light is effectively σ^+ polarized. Therefore, it is sufficient to illuminate the atom with σ^- light. In this experiment, the diameter of the atomic cloud is less than 1 mm containing more than 10^4 atoms [50, 51].

2.2.3 Optical dipole trap

After successfully trapping and cooling atoms in the MOT, one can transfer them into an optical dipole trap by simply overlapping the focus of the ODT with the atomic cloud, before turning off the MOT [51]. The principle of an optical dipole trap relies on an attractive force induced by a shift of energy levels due to light-atom interaction. For a two level system, the so-called AC-Stark energy level shift is proportional to the light intensity irradiating the atom, which leads to an attractive force in case of a red detuning [52]. The atom is then trapped at the position of the highest intensity, i.e., in the center of a tightly focused beam [53]. The ^{87}Rb quantum system can be approximated by a three level system ($5^2S_{1/2}$, $5^2P_{1/2}$, $5^2P_{3/2}$). For linear polarized light, the AC-Stark shift expressed by the potential of the ground state is given by [54]:

$$U_{\mathrm{dip}}(r,z) = \frac{\pi\, c^2\, \Gamma}{2\omega_{\mathrm{t}}^3} \left(\frac{2}{\Delta_{2,\,\mathrm{F}}} + \frac{1}{\Delta_{1,\,\mathrm{F}}} \right) I(r,z) \tag{2.1}$$

with the spontaneous decay rate Γ of the excited state $5^2P_{1/2}$, the transition frequency ω_{t}

of the D2 line and the detuning $\Delta_{1,\,\mathrm{F}}$, $\Delta_{2,\,\mathrm{F}}$ of the laser beam with regard to the transition line D1 respectively D2. The spatial intensity profile $I(r,z)$ is given by the Gaussian laser mode $\mathrm{TEM}_{0,0}$ which is defined by:

$$I(r,z) = I_0 \left[\frac{w_0}{w(z)}\right]^2 e^{-\frac{2\,r^2}{w_0^2}}, \quad \text{with} \qquad w(z) = w_0\sqrt{1+\left(\frac{z}{z_\mathrm{R}}\right)^2}\,. \tag{2.2}$$

In this equation $w(z)$ denotes the beam width at position z, $z_\mathrm{R} = \pi\, w_0/\lambda$ the Rayleigh length and λ the wavelength. In the focus at $z = 0$ the beam waist is given by w_0 and the intensity by I_0. Figure 2.3 depicts the longitudinal and transverse shape of a Gaussian beam. In case of low thermal energies $T \cdot k_\mathrm{B}$ compared to the potential depth $\hat{U}$, Equation 2.1 and 2.2 can be approximated by a cylindrically symmetric harmonic oscillator

$$U_\mathrm{FB}(r,z) \approx -\hat{U}\left[1 - 2\left(\frac{r}{w_0}\right)^2 - \left(\frac{z}{z_\mathrm{R}}\right)^2\right] = \frac{1}{2}\,m\,(\omega_\mathrm{r}\,r^2 + \omega_\mathrm{z}\,z^2), \tag{2.3}$$

with the oscillation frequencies in radial direction $\omega_\mathrm{r} = \sqrt{4\hat{U}/\,(m\,w_0^2)}$ and longitudinal direction $\omega_\mathrm{z} = \sqrt{2\hat{U}/\,(m\,z_\mathrm{R}^2)}$ and m the mass of ^{87}Rb [54].

Since the ODT with a wavelength 849.5 nm is far-detuned from any possible ground state transition, disturbing effects like off-resonant excitation or photon scattering can be neglected. The waist is given by $w_0 \approx 2.08\,\mu\mathrm{m}$ and the Rayleigh length is $z_\mathrm{R} = 15.54\,\mu\mathrm{m}$ [55]. For such a small volume, collisions become the dominant part of the atom loss mechanism leading to the so-called collisional blockade mechanism [56, 57]. This process limits the maximal number of trapped atoms to one. The potential depth and therefore the two oscillation frequencies can be tuned by the power of the ODT laser. A laser power of 60 mW results in a trapping potential depth $\hat{U} = k_\mathrm{B}\cdot\, 2.74\,\mathrm{mK}$ and oscillation frequencies of $\omega_\mathrm{r} = 2\pi\cdot\, 79.5\,\mathrm{kHz}$, $\omega_\mathrm{z} = 2\pi\cdot\, 7.4\,\mathrm{kHz}$.

According to [54] the density distribution for a thermal state of the atom within an optical dipole trap is given by

$$n(r,z,T) = n_0\, e^{-\frac{U(r,z)}{k_\mathrm{B}T}}. \tag{2.4}$$

The color gradient of Figure 2.3 indicates the distribution of the atom inside a Gaussian optical dipole trap. In case of the low temperature approximation (Eq. 2.3), the distribution is Gaussian and given by

$$n(r,z,T) = \frac{1}{(2\pi)^{3/2}\,\sigma_\mathrm{z}\,\sigma_\mathrm{r}^2}\, e^{-\frac{z^2}{2\sigma_\mathrm{z}^2}}\, e^{-\frac{r^2}{2\sigma_\mathrm{r}^2}}, \quad \text{with} \qquad \sigma_\mathrm{i} = \sqrt{\frac{k_\mathrm{B}\,T}{m\,\omega_\mathrm{i}^2}}\,. \tag{2.5}$$

Here σ_i denotes the Gaussian spatial standard deviation which are given by $\sigma_\mathrm{r} = 135.7\,\mathrm{nm}$ and $\sigma_\mathrm{z} = 1.45\,\mu\mathrm{m}$ for a temperature of $T = 48\,\mu\mathrm{K}$. Therefore, the probability to find the atom in the region $\pm\,2\sigma_i$ from the center of the trap is given by 95.45 %.

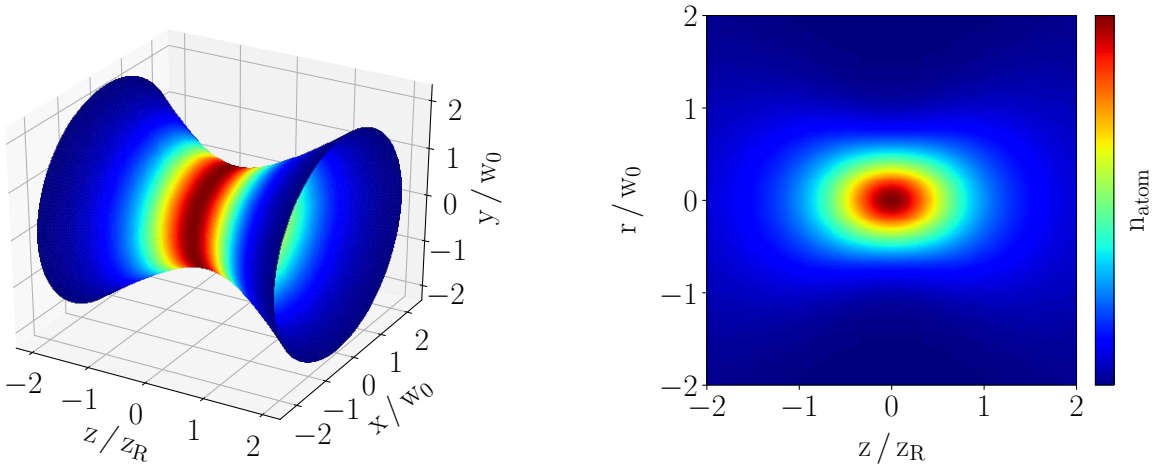

(a) Schematic surface plot of the Gaussian beam.

(b) Schematic contour plot of the density distribution of the atom within the ODT.

Figure 2.3: Schematic surface and contour plot of a Gaussian beam. The color gradient indicates the density distribution of the atom within the ODT. Red colors show regions of a high chance, blue regions a low chance to detect the atom.

2.2.4 Confocal microscope setup

To observe trapped atoms, fluorescence light can be collected and analyzed. A microscope objective[3] located outside the glass cell with a high numerical aperture (NA) of 0.5 guarantees high collection efficiencies (see Chapter 3). The same objective that collects single photons also focuses light for the ODT and ionization, which is used for a state selective readout (see Subsection 2.3.3). The three wavelengths ($\lambda_{\text{ionization}} = 473\,\text{nm}$, $\lambda_{\text{fluorescence}} = 780\,\text{nm}$, $\lambda_{\text{ODT}} = 850\,\text{nm}$) are superimposed/separated by two dichroic mirrors. Fluorescence light and single entangled photons are coupled into a single-mode fiber and guided to single photon detectors for further analysis. The dipole trap and pulsed ionization light is collimated and focused on the atom to trap respectively ionize the atom. Figure 2.4 gives an overview of the microscope setup. A detailed description of all elements and their operation can be found in Chapter 5.
The direction of photon collection (the optical axis of the microscope objective) defines the quantization axis of the atom and is denoted as z. The x-axis is defined to be parallel to the optical table, the y-axis perpendicular to it (see Appendix B).

A rapid increase of fluorescence detections indicates a trapped atom, while MOT and ODT are switched on. If the ODT overlaps with the MOT, scattered light of the cooling transition is collected. As soon as the fluorescence counts exceed a predefined threshold, the magnetic field of the MOT is turned off. The setup is now ready for further experiments (Section 2.3). Whenever the atom falls out of the ODT, the detection rate drops to

[3]Custom designed by Photon Gear.

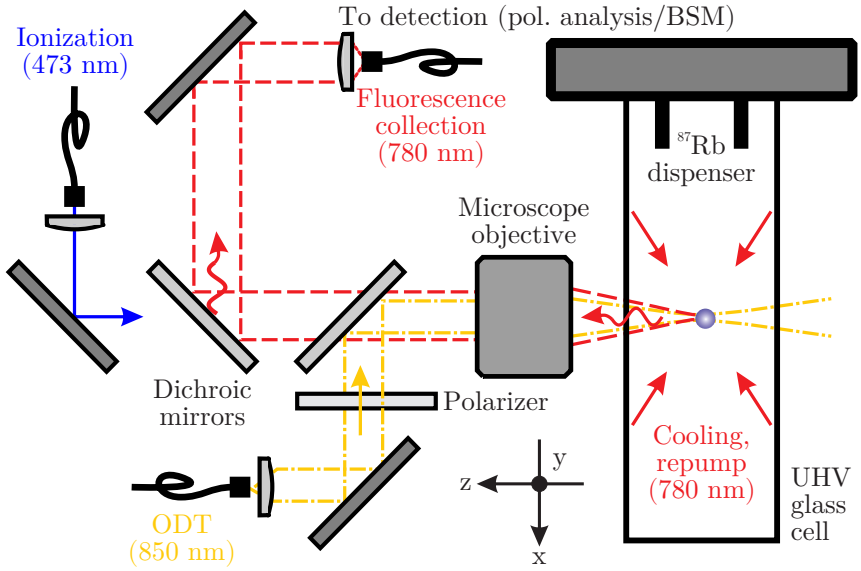

Figure 2.4: Overview of the microscope setup. The microscope objective collects single photons and focuses light for ionization and optically trapping atoms. Two dichroic mirrors superimpose respectively separate these three wavelengths. [55]

background level and the MOT/ODT are automatically switched on again [48].

2.3 Generating atom-photon entanglement

The entanglement generation scheme between the photonic polarization state and the atomic state consists of two steps: a specific atomic state must be prepared such that the spontaneous decay generates atom-photon entanglement [50, 58]. Afterwards, a verification of this entanglement can be performed by an atomic and photonic state read-out.

2.3.1 State preparation

The atom is in one of the two stable $5^2S_{1/2}$ states after the trapping scheme, most likely in F = 2. Optically pumping the atom from $5^2S_{1/2}$, F = 2 to $5^2P_{3/2}$, F' = 1 state ($\text{pump}_{2\to1}$) results in a decay into the states $5^2S_{1/2}$, F = 1, 2 (see Figure 2.5 (a)). When the optical transition is continuously driven, the atom sooner or later ends up in the F = 1 state. Alternating pump polarizations address every single Zeeman substate and decrease the residual F = 2 population.

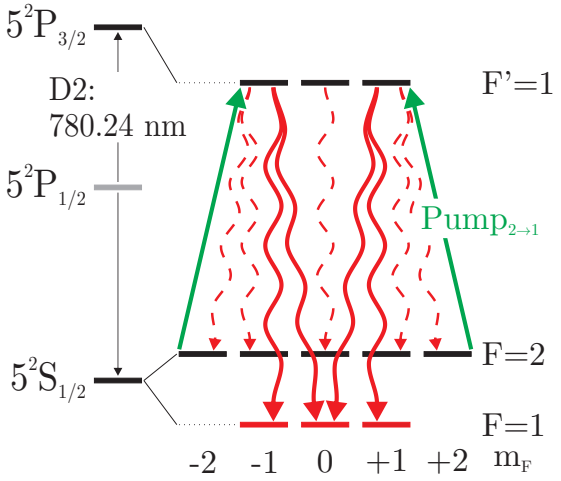

(a) The pump$_{2\to1}$ laser beam excites atoms to the $5^2P_{3/2}$, F' = 1 states. After some time, atoms populate the $5^2S_{1/2}$, F = 1 states.

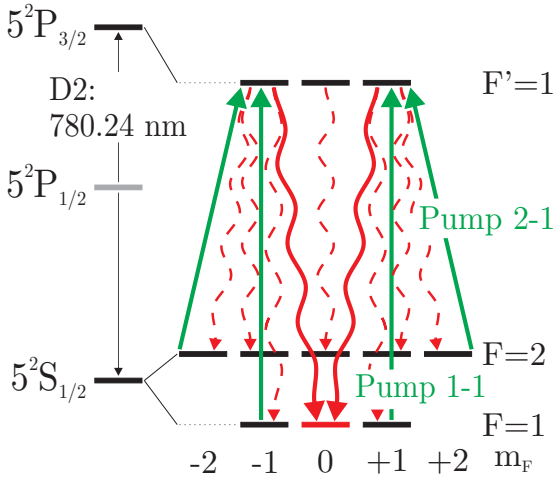

(b) Applying the pump$_{2\to1}$ and pump$_{1\to1}$ laser beam simultaneously lead to a population of the $|F = 1, m_F = 0\rangle$ dark state.

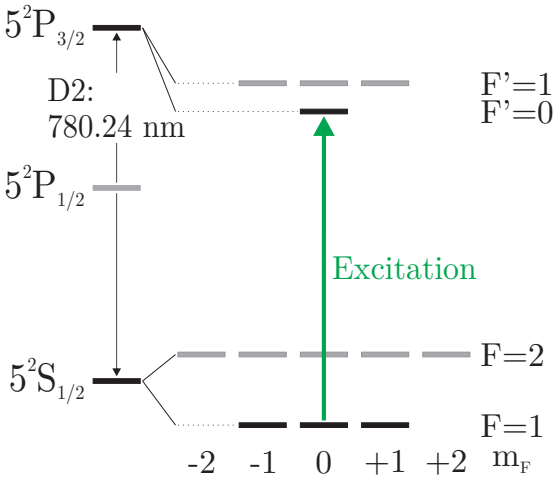

(c) A π polarized excitation pulse, excites the atom from the $|F = 1, m_F = 0\rangle$ to the $|J = 3/2, F' = 0, m_F = 0\rangle$ state.

Figure 2.5: Scheme for state preparation of the Λ-system. The three subfigures show sections of the ^{87}Rb energy level structure containing the different steps of the state preparation scheme. Green arrows indicate optically driven transitions, red curvy arrows the possible decay channels. Desired decay channels marked by solid lines point to dark states which are indicated by red blocks.

Driving the transition $5^2S_{1/2}$, F = 1 → $5^2P_{3/2}$, F' = 1 (pump$_{1\to1}$) only addresses the $|F = 1, m_F = \pm 1\rangle$ states, which leads to an selection rule induced $|F = 1, m_F = 0\rangle$ dark

state (see Figure 2.5 (b)). Therefore, applying pump$_{2\to1}$ and pump$_{1\to1}$ simultaneously yields a $|\mathrm{F}=1,\mathrm{m_F}=0\rangle$ population with an efficiency of $\eta_{\mathrm{pump}} = 0.8$ within less than 4 µs [48]. A more detailed overview of the pump laser beams can be found in Appendix A. Afterwards, a short $\pi-$ polarized laser pulse excites the atom to the $|\mathrm{J}=3/2,\ \mathrm{F'}=0,\ \mathrm{m_{F'}}=0\rangle$ state, the initial point of the Λ-system (see Figure 2.5 (c)) with a high efficiency $\eta_{\mathrm{exc}} \approx 1$. For Bell-state measurements a lower excitation efficiency of $\eta_{\mathrm{exc}} = 0.8$ is chosen to reduce two photon emission events during one excitation process. This leads to a better fidelity of atom-atom entanglement. More information about the excitation process can be found in [59].

2.3.2 Atom-photon entanglement

The spontaneous decay of the excited $|\mathrm{J}=3/2,\ \mathrm{F'}=0,\ \mathrm{m_{F'}}=0\rangle$ state occurs within an average lifetime of 26.2 ns [39]. Dipole selection rules only allow a decay into the $|\mathrm{F}=1,\mathrm{m_F}=\pm1\rangle$ or $|\mathrm{F}=1,\mathrm{m_F}=0\rangle$ states. The transition probabilities for the three different decays are 1/3 due to equal Clebsch-Gordan coefficients [39]. Conservation of angular momentum leads to a bijective mapping between the three possible atomic and three possible photon polarization states. An emission of a $\sigma^{\pm}$ polarized photon generates the atomic state $|\mathrm{F}=1,\mathrm{m_F}=\pm1\rangle$, a π polarized photon the state $|\mathrm{F}=1,\mathrm{m_F}=0\rangle$. In Chapter 3, the coupling efficiency for differently polarized photons into single-mode fibers is calculated. This coupling efficiency nearly vanishes for π polarized photons. Therefore, the entanglement of atomic state $|\mathrm{F}=1,\mathrm{m_F}=0\rangle$ and π polarized photon does occur, but is not exploited for further applications. For that reasons, spontaneous decay creates entanglement between the flying qubit encoded in the photon polarization state $|\sigma^{\pm}\rangle$ and the atomic qubit $|\mathrm{F}=1,\ \mathrm{m_F}=\pm1\rangle$ (Fig. 2.6):

$$
\begin{aligned}
|\Psi\rangle_{\mathrm{A,P}} &= \frac{1}{\sqrt{2}}\left(|\sigma^+\rangle\,|\mathrm{F}=1,\ \mathrm{m_F}=-1\rangle + |\sigma^-\rangle\,|\mathrm{F}=1,\ \mathrm{m_F}=+1\rangle\right) \\
&\equiv \frac{1}{\sqrt{2}}\left(|\sigma^+\rangle\,|{\downarrow}\rangle_{\mathrm{z}} + |\sigma^-\rangle\,|{\uparrow}\rangle_{\mathrm{z}}\right) \qquad (2.6)\\
&= \frac{1}{\sqrt{2}}\left(|\mathrm{H}\rangle\,|{\downarrow}\rangle_{\mathrm{x}} + |\mathrm{V}\rangle\,|{\uparrow}\rangle_{\mathrm{x}}\right) \qquad (2.7)
\end{aligned}
$$

The quantum state $|\Psi\rangle_{\mathrm{A,P}}$ can be identified as one of the Bell-states, thus it is maximally entangled. For clarity, the atomic states are expressed by their orientation to the quantization axis[4] (Eq. 2.6). It is possible to project $|\Psi\rangle_{\mathrm{A,P}}$ onto other orthogonal basis sets e.g. $\{|\mathrm{H}\rangle, |\mathrm{V}\rangle\}$ and $\{|{\downarrow}\rangle_{\mathrm{x}}, |{\uparrow}\rangle_{\mathrm{x}}\}$ (see Equation 2.7). For further information see Appendix B. Imperfections in the pumping or excitation process lead to different entangled quantum states or even to no atom-photon entanglement at all [38, 59].

[4]Henceforth the following abbreviations are used:
The Zeeman sub-levels of the $5^2\mathrm{S}_{1/2}$, F = 1 ground state are denoted according to their spin-orientation with regard to the quantization axis ($|{\downarrow}\rangle_{\mathrm{z}} \equiv |\mathrm{F}=1,\ \mathrm{m_F}=-1\rangle$ and $|{\uparrow}\rangle_{\mathrm{z}} \equiv |\mathrm{F}=1,\ \mathrm{m_F}=+1\rangle$).

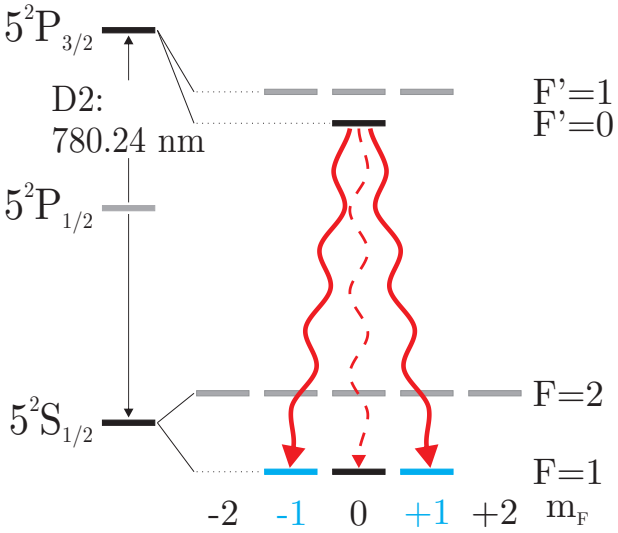

Figure 2.6: Section of the energy level structure of ^{87}Rb containing the Λ-system generating atom-photon entanglement. The atom is prepared in the $5^2P_{3/2}$, F' = 0 state and decays into $5^2S_{1/2}$, F = 1. Since π polarized light is not coupled into the single-mode fiber (see Chapter 3), entanglement between photon polarization states $|\sigma^+\rangle$, $|\sigma^-\rangle$ and atomic states $|F = 1, m_F = \pm 1\rangle$ arises.

2.3.3 Atomic and photonic qubit read-out

To verify atom-photon entanglement and not only correlation, it must be possible to read out the atomic state as well as the polarization state of the photon in several bases. Hence, the following polarization analysis and state selective ionization scheme are used.

Photonic polarization state read-out

The emitted photons are collected, coupled into a single-mode fiber and guided to a polarization analysis. This consists of a polarizing beamsplitter (PBS) and single-photon detectors such as avalanche photo diodes (APDs) at each output. The PBS separates two orthogonal polarizations with regard to their orientation to the optical axis of the birefringent material or with regard to the reflection on dielectric coatings. The natural measurement basis of a PBS is $|H\rangle$ and $|V\rangle$ for a typically horizontal plane of incoming and reflected beam. For a projection onto an arbitrary measurement basis, a combination of half- and quarter-wave plates are put in front of the PBS [48].

Atomic state read-out

For a clear understanding of the state selective atomic read-out scheme, the concrete example of a read-out using σ^+ polarized light is presented first (see Figure 2.7 (a)):
Driving the optical transition from the atomic qubit states $|\downarrow\rangle_z$, $|\uparrow\rangle_z$ to the $5^2P_{1/2}$, F' = 1 levels using σ^+ polarized light only excites the $|\downarrow\rangle_z$ state. Dipole selection rules forbid

any transition of $|\uparrow\rangle_z$ since there is no $|J = 1/2, F' = 1, m_{F'} = +2\rangle$ state. Simultaneously irradiated ionization light at $\lambda = 473\,\text{nm}$, only ionizes atoms which are in the excited state, i.e., which have been in the $|\downarrow\rangle_z$ state before. The ionization fragments are not trapped by the ODT anymore and are accelerated by strong electric fields to two channel electron multipliers (CEMs). The CEMs detects the fragments within 1 µs and guarantees space-like separation between the two labs [10, 41, 60, 61]. A detection of fragments clearly indicates the $|\downarrow\rangle_z$ state, hence it is denoted as bright state $|\Psi_B\rangle$. An absence of any detection signal then indicates the $|\uparrow\rangle_z$ state, thus it is denoted as dark state $|\Psi_D\rangle$. An alternative method to distinguish bright and dark state is given by the detection of fluorescence light. If the atom is not ionized and still trapped, cooling light is scattered by the atom. Therefore, a detection of this light clearly indicates the dark state.

In general, the excitation process $5^2S_{1/2}$, $F = 1 \rightarrow 5^2P_{1/2}$, $F' = 1$ is possible for every superposition of σ^+ and σ^- polarized light of the read-out laser [50]:

$$|\chi\rangle_{RO} = \sin(\alpha)\,|\sigma^+\rangle - e^{i\phi}\cos(\alpha)\,|\sigma^-\rangle\,, \tag{2.8}$$

with α, $\phi \in [0, 2\pi)$. These two parameters and therefore the polarization of the read-out laser can be adjusted freely by a combination of quarter- and half-wave plates. This adjustment determines the read-out basis and the corresponding orthogonal bright and dark states:

$$\begin{aligned} |\Psi_B\rangle &= \sin(\alpha)\,|\downarrow\rangle_z - e^{i\phi}\cos(\alpha)\,|\uparrow\rangle_z\,, \\ |\Psi_D\rangle &= \cos(\alpha)\,|\downarrow\rangle_z + e^{i\phi}\sin(\alpha)\,|\uparrow\rangle_z \end{aligned} \tag{2.9}$$

with $\langle\Psi_B|\Psi_D\rangle = 0$. For further information about the relation of different photonic and atomic states see Appendix B.

Performance and imperfections of atomic state read-out

Without any imperfections, the previously presented scheme would lead to a certain detection and differentiation of bright and dark state. A measure of imperfections in the read-out scheme is given by the contrast. It is defined by the difference between the ionization probability of bright state and dark state.
Reasons for imperfections are off-resonant excitations, detection efficiencies of the ionization fragments $\eta_{det} \gtrsim 0.98$ and the finite lifetime of the $5^2P_{1/2}$, $F' = 1$ state. The latter leads to a decay into the ground states which can not be ionized (see Figure 2.7 (b)). Applying a cycling laser, it is at least possible to ionize the fraction which decayed to the $5^2S_{1/2}$, $F = 2$ states. The atom is excited to the $5^2P_{3/2}$, $F' = 3$ states and can be ionized afterwards. By optimizing the optical transitions, a contrast of $\eta_{RO} = 0.94$ is achievable [41]. More detailed information about the ionization process can be found in [38, 41, 62].

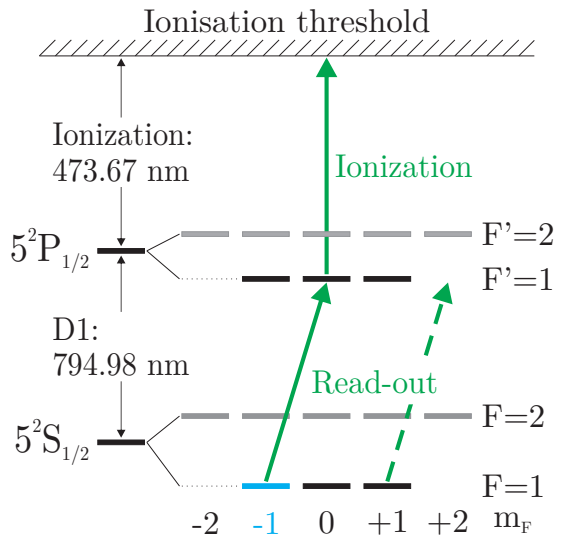

(a) σ^+ polarized light can only excite the $|F = 1, m_F = -1\rangle$ state. The atom is ionized afterwards.

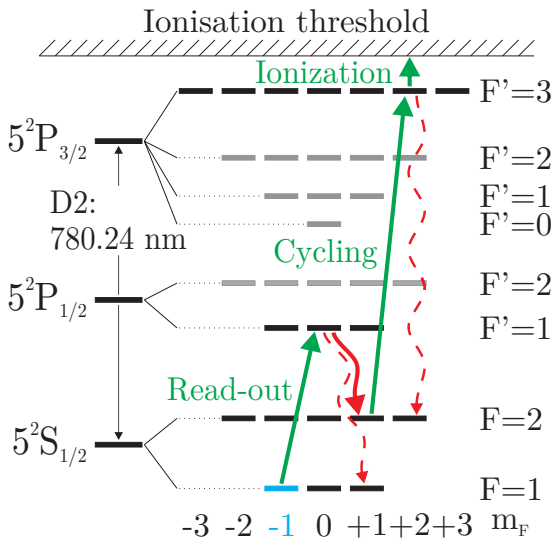

(b) If the $5^2P_{1/2}$, F' = 1 state decays before ionizing, the cycling laser excites the atoms in the $5^2S_{1/2}$, F = 2 state which can be ionized afterwards.

Figure 2.7: Schematic of the ionization process. The two subfigures show sections of the ^{87}Rb energy level structure. Green arrows indicate optically driven transitions, red curvy arrows the possible decay channels, desired decay channels are marked by solid lines.

2.4 Heralded generation of atom-atom entanglement

Heralded entanglement of two atomic qubits is obtained by using the entanglement swapping protocol [23, 63]. In this protocol, the atom-atom entanglement is generated without any direct interaction between the two separated atoms. The starting point are two independent entangled atom-photon pairs (according to Section 2.3). Both photons are guided to a so-called Bell-state measurement apparatus, where they are projected onto a joint entangled two-photon Bell-state. This leads to an entanglement of the two stationary atomic qubits.

2.4.1 Entanglement swapping

The two independently generated entangled atom-photon pairs form a joint four particle state $|\Psi\rangle$. It can be described as the tensor product of two entangled atom-photon states $|\Psi\rangle_{A,P}$. Their representation in the $\{|H\rangle, |V\rangle\}$ and $\{|\downarrow\rangle_x, |\uparrow\rangle_x\}$ basis is used (Eq. 2.7) where the photon states can be measured without any further basis transformation:

$$
\begin{aligned}
|\Psi\rangle &= |\Psi\rangle_{\mathrm{A_1,P_1}} \otimes |\Psi\rangle_{\mathrm{A_2,P_2}} \\
&= \left[\frac{1}{\sqrt{2}}(|\mathrm{H}\rangle_1 |\downarrow\rangle_{1,\mathrm{x}} + |\mathrm{V}\rangle_1 |\uparrow\rangle_{1,\mathrm{x}})\right] \otimes \left[\frac{1}{\sqrt{2}}(|\mathrm{H}\rangle_2 |\downarrow\rangle_{2,\mathrm{x}} + |\mathrm{V}\rangle_2 |\uparrow\rangle_{2,\mathrm{x}})\right]
\end{aligned} \tag{2.10}
$$

with the subscripts 1 or 2 indicating the different atom-photon pairs. Expressing Equation 2.10 in terms of the four maximally entangled two-particle Bell-states, leads to [48]:

$$
\begin{aligned}
|\Psi\rangle = \frac{1}{2} \big(&|\Psi^+\rangle_{\mathrm{A_1,A_2}} |\Psi^+\rangle_{\mathrm{P_1,P_2}} + |\Psi^-\rangle_{\mathrm{A_1,A_2}} |\Psi^-\rangle_{\mathrm{P_1,P_2}} \\
&+ |\Phi^+\rangle_{\mathrm{A_1,A_2}} |\Phi^+\rangle_{\mathrm{P_1,P_2}} + |\Phi^-\rangle_{\mathrm{A_1,A_2}} |\Phi^-\rangle_{\mathrm{P_1,P_2}} \big)
\end{aligned} \tag{2.11}
$$

$$
\begin{aligned}
\text{with the atomic Bell-states:} \quad |\Psi^\pm\rangle_{\mathrm{A_1,A_2}} &= \frac{1}{\sqrt{2}}(|\uparrow\rangle_{1,\mathrm{x}} |\downarrow\rangle_{2,\mathrm{x}} \pm |\uparrow\rangle_{2,\mathrm{x}} |\downarrow\rangle_{2,\mathrm{x}}) \\
|\Phi^\pm\rangle_{\mathrm{A_1,A_2}} &= \frac{1}{\sqrt{2}}(|\uparrow\rangle_{1,\mathrm{x}} |\uparrow\rangle_{2,\mathrm{x}} \pm |\downarrow\rangle_{2,\mathrm{x}} |\downarrow\rangle_{2,\mathrm{x}})
\end{aligned} \tag{2.12}
$$

$$
\begin{aligned}
\text{and the photonic Bell-states:} \quad |\Psi^\pm\rangle_{\mathrm{P_1,P_2}} &= \frac{1}{\sqrt{2}}(|\mathrm{H}\rangle_1 |\mathrm{V}\rangle_2 \pm |\mathrm{V}\rangle_1 |\mathrm{H}\rangle_2) \\
|\Phi^\pm\rangle_{\mathrm{P_1,P_2}} &= \frac{1}{\sqrt{2}}(|\mathrm{H}\rangle_1 |\mathrm{H}\rangle_2 \pm |\mathrm{V}\rangle_1 |\mathrm{V}\rangle_2)\,.
\end{aligned} \tag{2.13}
$$

Equation 2.11 shows that a detection of a two-particle photonic Bell-state heralds the generation of the corresponding two-particle atomic Bell-state. Hence, the spatially separated atomic qubits are entangled.

2.4.2 Photonic Bell-state projection

To perform such a two-particle photonic Bell-state measurement (BSM), the two photons are guided to the Bell-state measurement apparatus shown in Figure 2.8. It consists of a non polarizing 50/50 fiber beamsplitter (fiber BS) with free-space polarizing beamsplitters at each output. An APD detects the photons at all PBS outputs. To project the two photons onto a Bell-state, the following scheme is used. Whenever a pair of indistinguishable[5] photons arrive at the fiber BS, the so-called Hong-Ou-Mandel effect [64] occurs. Two photons interfere with each other and the probabilities to leave the BS at specific output add. This leads to photon bunching in the case of symmetric[6] Bell-states $|\Psi^+\rangle_{\mathrm{P_1,P_2}}$, $|\Phi^+\rangle_{\mathrm{P_1,P_2}}$ or $|\Phi^-\rangle_{\mathrm{P_1,P_2}}$ and photon anti-bunching for the anti-symmetric Bell-state $|\Psi^-\rangle_{\mathrm{P_1,P_2}}$. The two photon interference process is described detailedly in [59]. A successful BSM is indicated

[5] In this case indistinguishable means identical in all degrees of freedom other than the polarization state. Spatial overlap is guaranteed by using the fiber BS, spectral overlap by their common origin of the same Λ-system and temporal overlap by adapting the excitation sequence to the different fiber lengths.

[6] Symmetric under exchange of particles.

by coincidental detection of two photons at specific detectors, matching a respective Bell-state. For a measurement of the $|\Psi^-\rangle_{P_1,P_2}$ state, coincidental clicks of the APDs $1_{||} \wedge 2_\perp$ or $1_\perp \wedge 2_{||}$ must be detected. The $|\Psi^+\rangle_{P_1,P_2}$ state is indicated by clicks of the detectors $1_{||} \wedge 1_\perp$ or $2_{||} \wedge 2_\perp$. As the $|\Phi^\pm\rangle_{P_1,P_2}$ states are symmetric and have the same polarization, two photons impinge on any of the four detectors. The detectors can not distinguish between one or two photons arriving at the same time, hence these states can not be observed. Furthermore, the $|\Phi^\pm\rangle_{P_1,P_2}$ states are indistinguishable by only analyzing clicks at the detectors, anyway.
Applying this scheme, a violation of Bell's inequality was demonstrated while closing locality and detection loophole simultaneously [10].

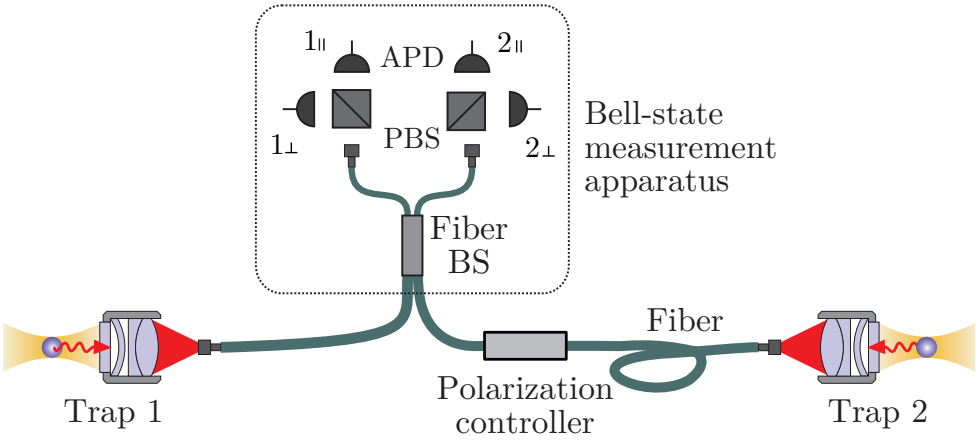

Figure 2.8: Schematic of the atom-atom entanglement scheme. The photons of two independently entangled atom-photon pairs, are guided to the Bell-state measurement apparatus. A Bell-state measurement (coincidental detection of two photons) is performed leading to an entanglement of the two atomic qubits. [55]

2.5 Limitations and prospects of long-distance entanglement

Many future quantum communication applications, such as quantum repeaters and quantum networks, rely on entanglement of quantum memories separated over large distances [35]. In this experiment, the achieved distance between two entangled atomic qubits is 700 m fiber length. For a feasible application of quantum communication, this distance must be extended to the range of $\sim$ 100 km. Two major difficulties prevent the above mentioned heralded entanglement swapping experiment from increasing the distance: the coherence of atomic qubits and the achievable atom-atom entanglement rate.

2.5.1 Coherence of atomic qubits

A successful scheme for heralded atom-atom entanglement generation as described in Section 2.4 assumes that the initially prepared atomic qubit is maintained until the state read-out. This period of time consists of the duration until both photons arrive at the BSM, the time that the BSM electronics needs for evaluation and sending back the signal to the read-out setup. The read-out scheme is only initialized when a signal from the BSM is received. In the current setup, the time span between excitation and read-out is 7.3 µs (see Fig. 2.9). If the fiber length is extended to 20 or even 100 km, this time increases to 200 µs respectively 1 ms. During that period of time, the atomic state is prone to external decoherence effects. In an UHV setup the main external influences are fluctuating external magnetic and electric fields, which lead to a Zeeman splitting and Larmor precession of different Zeeman substates. In the current setup, the probability to find the atom in the prepared state after 120 µs is reduced to > 0.8 [38].

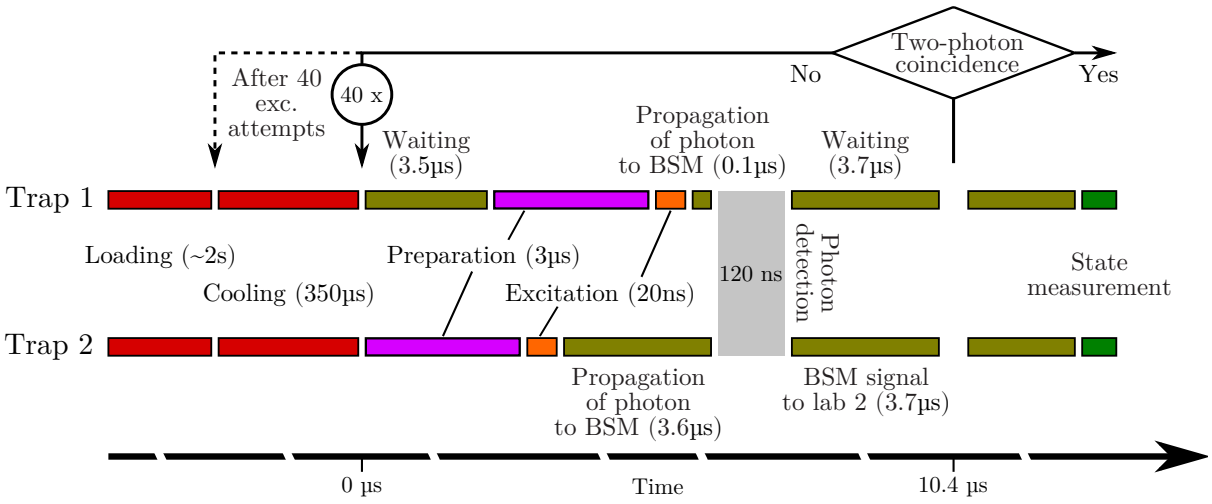

Figure 2.9: Experimental sequence for entanglement of two atomic states based on entanglement swapping. In this sequence, the atoms are spatially separated by a fiber length of 700 m. After successfully loading and cooling two single ^{87}Rb atoms, state preparation and excitation is initialized such that both emitted photons arrive simultaneously at the BSM apparatus located close to trap 1. After the BSM, the corresponding results are sent back to the individual traps. If the BSM was successful, the state read-out is performed. Otherwise the sequence starts from the beginning. Since excitation heats the atoms, there is an additional cooling period after 40 repetitions. [48]

External magnetic fields originate from experimental components in the vicinity of the atom or from the Munich metro, which is only 60 m away from the laboratory. The exact influence of external magnetic fields is further described in [47]. By applying a magnetic guiding field at the position of the atom, it is possible to reduce the influence of external

magnetic fields. Though, the guiding field is controlled by a feedback loop which obtains data from a 3D magnetic sensor[7] next to the glass cell [47, 48]. Furthermore, the guiding field can be used to suppress decoherence effects produced by the optical dipole trap.

In the case of a circular polarized optical dipole trap, a state dependent term[8] has to be added to Equation 2.1. This leads to a splitting of the Zeeman substates and in general to comparable decoherence effects as for magnetic fields. The fraction of circular polarization can be sufficiently reduced by using a linear polarizer. Nevertheless, in strongly focused laser beams longitudinal electric field components become significant, resulting in an elliptical polarization and thus decoherence at off-axis positions [38, 65–68]. Since this effect is mirror-symmetric with regard to the y-z-plane, decoherence effects compensate during a transverse oscillation of the atom. This results in a rephasing and increased probability to find the atom in the initialized state after multiples of the transverse oscillation period [38]. However, a perfect rephasing is only possible for a 1D transverse atom oscillation and an exact harmonic oscillator potential (Eq. 2.3). Since these assumptions do not match reality, the rephasing is slightly reduced. To decrease the decoherence effect induced by the strongly focused ODT, the atoms can be cooled further or a standing wave dipole trap can be used to potentially cancel longitudinal components completely [38, 69].

2.5.2 Remote atom-atom entanglement rate

Besides the atomic state decoherence, the small rate of heralded generation of atom-atom entanglement limits the applicability of the current setup when increasing the distance. In atom-atom entanglement schemes based on entanglement swapping protocol, the event rate can be calculated by:

$$R_{\mathrm{E}} = f_{\mathrm{E}} \cdot P_{\mathrm{A_1,P_1}} \cdot P_{\mathrm{A_2,P_2}} \cdot P_{\mathrm{BSM}} \cdot P_{\mathrm{duty}} \,. \tag{2.14}$$

f_{E} denotes the repetition rate, $P_{\mathrm{A_1,P_1}}$ and $P_{\mathrm{A_2,P_2}}$ the success probabilities of detecting atom-photon entanglement for trap 1 respectively 2 and P_{BSM} the probability that the photon pair is projected onto a measurable BSM state.

The repetition rate is given by the used experimental sequence (Fig. 2.9). It mainly depends on the amount of cooling (350 µs after every 40 excitation tries), the state preparation process (3 µs) and the time span between excitation and state read-out[9] (described in Subsection 2.5.1). Furthermore, the duty cycle probability P_{duty} must be considered,

[7] Honeywell, HMC1053.

[8] The potential of the ground state for the polarization P and the Landé factor g_{F} is given by:

$$U_{\mathrm{dip}}(r,z) = \frac{\pi\, c^2\, \Gamma}{2\omega_{\mathrm{t}}^3} \left(\frac{2 + P\, g_{\mathrm{F}}\, m_{\mathrm{F}}}{\Delta_{2,\,\mathrm{F}}} + \frac{1 - P\, g_{\mathrm{F}}\, m_{\mathrm{F}}}{\Delta_{1,\,\mathrm{F}}} \right) I(r,z)\,, \text{ with } P = \begin{cases} 0, & \text{for linear polarized light} \\ \pm 1, & \text{for } \sigma^{\pm} \text{ polarized light} \end{cases} .$$

[9] This time span is given by $2(d_1 + d_2)/\left(\frac{2}{3}c\right)$ assuming a speed of light of $\frac{2}{3}$ c inside glass fibers and distances d_1, d_2 between BSM apparatus and trap 1 respectively 2.

which is determined by the probability, that the two atoms both are in a measurement-ready state, i.e., both atoms are cooled and trapped at the same time. This efficiency is hard to estimate.
The success probabilities of detecting atom-photon entanglement of the individual traps are well known and defined by:

$$P_{\mathrm{A,P}}(d) = \eta_{\mathrm{pump}}\,\eta_{\mathrm{exc}}\,\eta_{\mathrm{cc}}\,\eta_{\mathrm{det}}\,\eta_{\mathrm{loss}}\,\tau_{\mathrm{fiber}}(d) \tag{2.15}$$

and depend on the efficiencies of state preparation η_{pump}, excitation η_{exc}, detection η_{det} and the efficiency that an emitted photon is successfully collected and coupled into a single mode fiber η_{cc}. The transmission losses in optical fibers $\tau_{\mathrm{fiber}} = 10^{-\alpha\, d/10}$ with the fiber attenuation α depends on the distance d between trap setup and detectors. As the distance d differs for the two traps, we distinguish between d_1 and d_2. In spite of optimizing the whole setup, some losses e.g. reflections of anti-reflective coated surfaces, are not avoidable. These losses are summarized by η_{loss}.
Since only 2 of 4 equiprobable photonic Bell-states are detectable (see Section 2.4), P_{BSM} is given by $\frac{1}{2}$.

The location of the BSM is in the same laboratory as trap 1, hence the distance d_1 is negligible ($d_1 \ll d_2 = d$), leading to an event rate of:

$$R_{\mathrm{E}} = \frac{1}{2}\,\frac{P_{\mathrm{duty}}}{\frac{350\,\mu\mathrm{s}}{40} + 3\,\mu\mathrm{s} + \frac{2d}{\frac{2}{3}c}}\;\eta_{\mathrm{cc}_1}\,\eta_{\mathrm{cc}_2}\,\eta_{\mathrm{pump}}^2\,\eta_{\mathrm{exc}}^2\,\eta_{\mathrm{det}}^2\,\eta_{\mathrm{loss}_1}\,\eta_{\mathrm{loss}_2}\,10^{-\frac{\alpha\, d}{10}}\;. \tag{2.16}$$

The experimental setup of the loophole-free Bell test [10] obtained 2.13 events/min at a fiber length of 700 m. According to Equation 2.16, an increase of the fiber length to 20 km, would drop the event rate to only one event per 60 years (Fig. 2.10). Hence, the setup of 2016 was not suitable for long-distance entanglement at reasonable event rates. Since 2016, the two following major modifications have been installed to increase the event rate for feasible long-distance entanglement applications.

Photon conversion to the telecom S band

The main reason for the insufficient event rates at long distances are the losses in the optical fibers. Loss mechanisms in glass fibers are caused by Rayleigh scattering and stimulated Brillouin respectively Raman scattering [70]. These losses are frequency dependent and are minimized in the telecom regime. Therefore, a decrease in attenuation from $\leq 3.5\,\mathrm{dB/km}$ at 780 nm to $\leq 0.18\,\mathrm{dB/km}$ is possible by using telecom wavelengths at 1550 nm. To maintain the entanglement scheme described previously, a telecom conversion process must preserve the polarization state of the photon without detecting it. The quantum frequency conversion (QFC) was adapted to this experiment, which allowed to observe entanglement with a fidelity of $\geq (78.5 \pm 0.9)\,\%$ between atom and telecom S band photon propagated through 20 km fiber [71]. An external device conversion efficiency of 57 % was obtained.

Furthermore, efficient superconducting single-photon detectors can be used in telecom wavelength which increases the detection efficiency up to 85 %.
In total, the QFC to the telecom regime results in higher event rates for larger distances than 770 m (see Figure 2.10).

High NA microscope objective setup

Another possibility to enhance the atom-atom entanglement rate is to optimize the collection and the coupling process of single photons. In 2018, a new custom designed high NA microscope setup was installed in one laboratory. Details of the setup can be found in Subsection 2.2.4 or in [55]. The new microscope objective is specified to operate diffraction limited up to the full NA of 0.5. The former replaced objective[10] (a standard commercial objective with a NA of 0.5) was not designed and optimized for the purpose of this experiment, leading to an efficient numerical aperture of 0.267 [41]. Therefore, a gain of a factor of ~ 2.5 in collection and coupling efficiency as well as in atom-photon success probability was obtained by installing the new microscope. In this thesis, the installation of the second, similarly constructed Photon Gear objective is described (Chapter 5). Assuming an identical gain in collection and coupling efficiency, the atom-atom entanglement rate increases by a factor of ~ 6.25. The resulting event rate is depicted in Figure 2.10. The QFC to the telecom regime combined with the new high NA microscope objective setup eventually leads to a rate of 0.41 events/min at a distance of 20 km. Using a symmetric setup, i.e., setting the fiber length to both traps equally ($d_1 = d_2$), increases the repetition rate and therefore the event rate at least to a feasible rate of 0.77 events/min at 20 km distance between the two traps. For larger distances the event rate drops significantly.

Nevertheless, further optimizations of the collection and coupling process are possible and described in this thesis. First of all, collection and coupling must be understood well. For this purpose the upper limit of the collection and coupling efficiency is simulated (Chapter 3). Afterwards the performance of involved optics is tested (Chapter 4) to identify elements which can be optimized.

[10] Mitutoyo G Plan Apo 50.

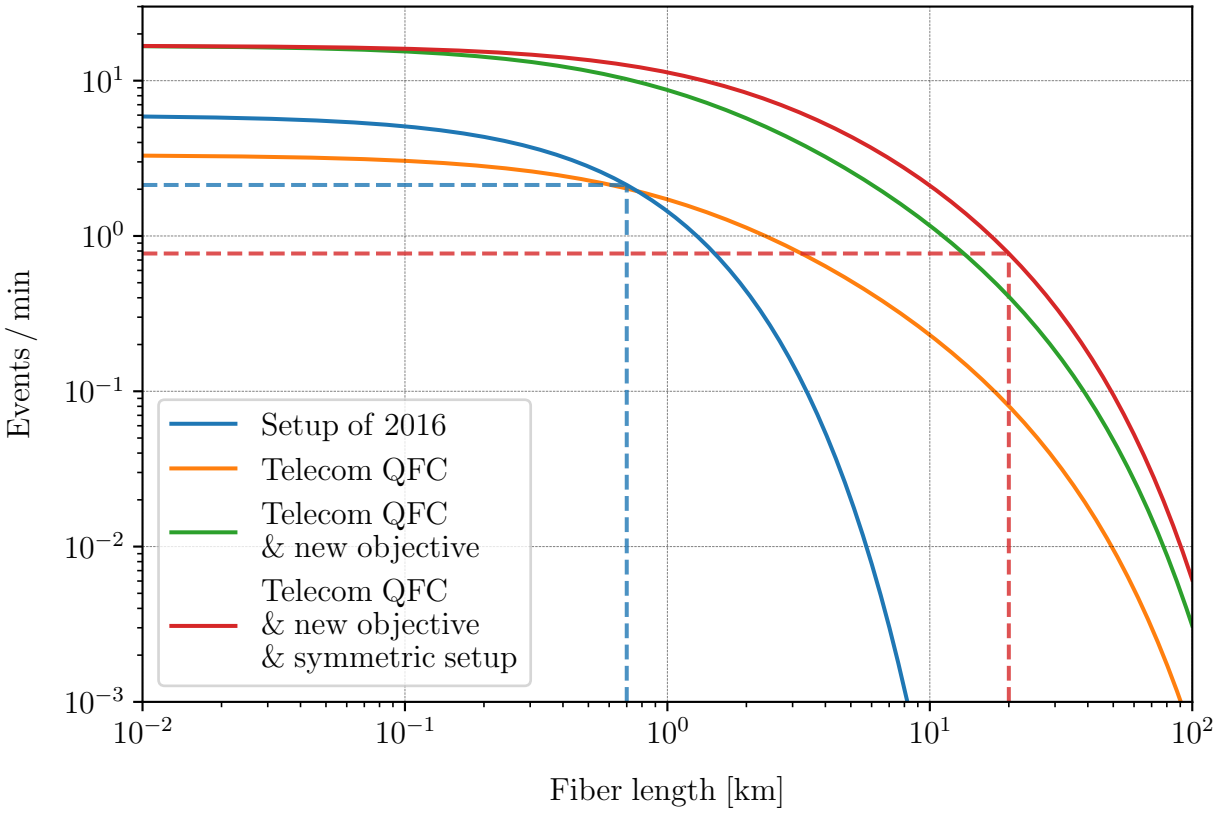

Figure 2.10: Estimated event rates of atom-atom entanglement in dependence on the total fiber length between the two traps. It was assumed that the setup of 2016 achieved a rate of 2.13 events/min at distance of 700 m. Quantum frequency conversion to the telecom regime leads to a loss in event rate for smaller distances than 770 m due to the external device conversion efficiency and higher event rates at larger distances due to less fiber attenuation. Introducing new microscope objectives, increases the collection and coupling efficiency. Hence, the event rate is increased by a factor of 6.25. Combining QFC, the new objectives and a symmetric setup leads to feasible event rates of 0.77 events/min at 20 km distance between the two traps.

Chapter 3

Photon collection and coupling efficiency

This chapter presents the simulation for the collection and coupling efficiencies. These simulations are performed for the case of optimal alignment and perfect optical properties of the involved components. Therefore, the estimated efficiencies refer to the upper physical limit. Calculations with regard to imperfections of the real experiment can be found in Subsection 5.3. The process of collection and coupling of photons can be split into two nearly independent processes. First of all, the collection process is described and simulated for atoms in the center of the ODT and for displaced atoms. The same procedure is done for the coupling process. Afterwards, the collection and coupling efficiency for a thermal distribution of the atom inside the ODT is estimated. This led to a reasonable improvement of the microscope setup described in Subsection 2.2.4 by implementing a self-made optimized fiber collimator.

3.1 Collection efficiency

For a simulation of the collection efficiency, the collection process and primarily the emission process must be investigated further. In the following, analytic expressions for the atomic dipole emission characteristic are derived such that they can be used for estimating the collection efficiency.

3.1.1 Analytic expressions for the atomic dipole emission characteristics

The spontaneous decay of the $5^2P_{3/2}$, F' = 0 state can be quantum mechanically described by a change of the probability amplitude of the valence electron from the $m_{F'} = 0$ state to the $5^2S_{1/2}$, F = 1 states. This process induces a transition dipole moment $\mathbf{p}_{e,g}$[1] whose expectation value is given by

[1] Henceforth, in this thesis, vectorial quantities are indicated by bold letters.

$$\begin{aligned}\mathbf{M}_{\mathrm{e,g}} = \langle \hat{\mathbf{p}}_{\mathrm{e,g}} \rangle &= \langle \mathrm{J} = 3/2, \mathrm{F'} = 0, \mathrm{m_{F'}} = 0 | \hat{\mathbf{p}} | \mathrm{J} = 1/2, \mathrm{F} = 0, \mathrm{m_F} = 0, \pm 1 \rangle \\ &= e \, \langle \mathrm{J} = 3/2, \mathrm{F'} = 0, \mathrm{m_{F'}} = 0 | \hat{\mathbf{r}} | \mathrm{J} = 1/2, \mathrm{F} = 0, \mathrm{m_F} = 0, \pm 1 \rangle \ ,\end{aligned} \tag{3.1}$$

with e the elementary charge and $\hat{\mathbf{r}}$ the spatial position operator. Only if at least one component of $\mathbf{M}_{\mathrm{e,g}}$ is non-vanishing, the transition is possible [72]. In case of the $5^2\mathrm{P}_{3/2}$, F' = 0 state, all three components do not vanish, leading to a possible decay to the three $5^2\mathrm{S}_{1/2}$, F = 1 states by emitting a $\sigma^{\pm}$ or π polarized photon.

In this thesis, the emission process is described by a semi-classical approach, which is less complicated than the quantum mechanical description [73] but still reflects the correct emission profiles. This approach considers an oscillating atomic dipole generating the mode of the emitted photon [73–75]. In the far field approximation ($k\,r \gg 1$), this mode is given by [75]:

$$\mathbf{E}(\mathbf{r}) = \frac{k^2}{4\,\pi\,\epsilon_0\,\epsilon_{\mathrm{r}}} \frac{e^{i\,k\,r}}{r} \left[(\mathbf{e}_{\mathrm{r}} \times \mathbf{e}_{\mathrm{p}}) \times \mathbf{e}_{\mathrm{r}} \right] \tag{3.2}$$

$$\text{with the radial unit vector } \mathbf{e}_{\mathrm{r}} = \begin{pmatrix} \sin(\theta)\cos(\phi) \\ \sin(\theta)\sin(\phi) \\ \cos(\theta) \end{pmatrix}, \tag{3.3}$$

where $\mathbf{e}_{\mathrm{p}}$ denotes the dipole oscillation direction, $k = 2\pi/\lambda$ the wavenumber, ϵ_0 and ϵ_{r} the vacuum respectively the relative permittivity and r the radial distance. The corresponding magnetic field can be calculated by using Maxwell equations. Choosing a linear ($\mathbf{e}_{\mathrm{p}} = \mathbf{e}_{\mathrm{z}}$) or circular ($\mathbf{e}_{\mathrm{p}} = \mathbf{e}_{\sigma^{\pm}} = \frac{1}{\sqrt{2}}(\mathbf{e}_{\mathrm{x}} \mp i\,\mathbf{e}_{\mathrm{y}})$) oscillation direction, the emission modes of the following polarization states (see photon polarization definition in Appendix B) are obtained [50, 73, 75]:

$$\pi \text{ photon:} \quad \mathbf{E}^{(\pi)}(\mathbf{r}) = \frac{k^2}{4\,\pi\,\epsilon_0\,\epsilon_{\mathrm{r}}} \frac{e^{i\,k\,r}}{r} \left[(\mathbf{e}_{\mathrm{r}} \times \mathbf{e}_{\mathrm{z}}) \times \mathbf{e}_{\mathrm{r}} \right], \tag{3.4}$$

$$\sigma^{\pm} \text{ photon:} \quad \mathbf{E}^{(\sigma^{\pm})}(\mathbf{r}) = \frac{k^2}{4\,\pi\,\epsilon_0\,\epsilon_{\mathrm{r}}} \frac{e^{i\,k\,r}}{r} \left[(\mathbf{e}_{\mathrm{r}} \times \frac{1}{\sqrt{2}}(\mathbf{e}_{\mathrm{x}} \mp i\,\mathbf{e}_{\mathrm{y}})) \times \mathbf{e}_{\mathrm{r}} \right]. \tag{3.5}$$

To simplify calculations of the following sections, superpositions of $\sigma^{\pm}$ emission modes are used. These superpositions corresponds to the emission of linear polarized H ($\mathbf{e}_{\mathrm{p}} = \frac{1}{\sqrt{2}}(\mathbf{e}_{\sigma^+} + \mathbf{e}_{\sigma^-}) = \mathbf{e}_{\mathrm{x}}$) or V ($\mathbf{e}_{\mathrm{p}} = \frac{i}{\sqrt{2}}(\mathbf{e}_{\sigma^+} - \mathbf{e}_{\sigma^-}) = \mathbf{e}_{\mathrm{y}}$) photons (see Appendix B):

$$\mathrm{H} \text{ photon:} \quad \mathbf{E}^{(\mathrm{H})}(\mathbf{r}) = \frac{k^2}{4\,\pi\,\epsilon_0\,\epsilon_{\mathrm{r}}} \frac{e^{i\,k\,r}}{r} \left[(\mathbf{e}_{\mathrm{r}} \times \mathbf{e}_{\mathrm{x}}) \times \mathbf{e}_{\mathrm{r}} \right], \tag{3.6}$$

$$\mathrm{V} \text{ photon:} \quad \mathbf{E}^{(\mathrm{V})}(\mathbf{r}) = \frac{k^2}{4\,\pi\,\epsilon_0\,\epsilon_{\mathrm{r}}} \frac{e^{i\,k\,r}}{r} \left[(\mathbf{e}_{\mathrm{r}} \times \mathbf{e}_{\mathrm{y}}) \times \mathbf{e}_{\mathrm{r}} \right]. \tag{3.7}$$

Obviously, the H or V emission modes are no eigenstates of the emission process with respect to the quantization axis z (Figure 2.6 and Appendix B). However, they are constructed by a superposition of eigenstates. Therefore, the estimated collection and coupling

efficiencies of Section 3.3 are identical for H, V photons and σ^+, σ^- photons. The corresponding efficiencies of Section 3.3 for $\sigma^\pm$ photons can be obtained by a simple substitution: H $\rightarrow \sigma^+$, V $\rightarrow \sigma^-$.

The emission characteristics of the atom (the probability that a photon is emitted into a solid angle $\mathrm{d}\Omega$) is obtained by normalizing the energy flux $\overline{\mathbf{S}}^{(\mathrm{i})}(\mathbf{r}) \propto |\mathbf{E}^{(\mathrm{i})}(\mathbf{r})|^2\,\mathbf{e}_\mathrm{r}$ through the surface element spanned by the differential solid angle $\mathrm{d}\mathbf{f} = \mathrm{d}f\,\mathbf{e}_\mathrm{r} = \mathrm{d}\Omega\,r^2\,\mathbf{e}_\mathrm{r}$ (see Figure 3.1):

$$\mathrm{d}P^{(\mathrm{i})}_{\mathrm{photon}}(\mathbf{r}) = \frac{1}{N_\mathrm{norm}}\,\overline{\mathbf{S}}^{(\mathrm{i})}(\mathbf{r})\cdot\mathrm{d}\mathbf{f} \tag{3.8}$$

$$= \frac{1}{N_\mathrm{norm}}\,\mathrm{d}\Omega\,r^2\,\mathbf{E}^{(\mathrm{i})}(\mathbf{r})\cdot(\mathbf{E}^{(\mathrm{i})}(\mathbf{r}))^* \tag{3.9}$$

$$\text{with}\quad N_\mathrm{norm} = \int_{4\pi}\mathrm{d}\Omega\,r^2\,\mathbf{E}^{(\mathrm{i})}(\mathbf{r})\cdot(\mathbf{E}^{(\mathrm{i})}(\mathbf{r}))^* = \frac{8\,\pi}{3}\,\frac{k^4}{16\,\pi^2\,\epsilon_0^2\,\epsilon_\mathrm{r}^2}\,, \tag{3.10}$$

where N_norm denotes the normalization constant, $(\cdot)^*$ the complex conjugate and $\mathrm{i} \in \{\pi, \sigma^\pm, \mathrm{H}, \mathrm{V}\}$. Emission characteristics for different polarizations can be calculated easily by inserting the corresponding oscillation direction which yields the results in [75]:

$$\mathrm{d}P^{(\pi)}_{\mathrm{photon}}(\mathbf{r}) = \mathrm{d}\Omega\,\frac{3\,(\sin^2(\theta))}{8\,\pi}\,, \tag{3.11}$$

$$\mathrm{d}P^{(\sigma^\pm)}_{\mathrm{photon}}(\mathbf{r}) = \mathrm{d}\Omega\,\frac{3\,(1+\cos^2(\theta))}{16\pi}\,, \tag{3.12}$$

$$\mathrm{d}P^{(\mathrm{H})}_{\mathrm{photon}}(\mathbf{r}) = \mathrm{d}\Omega\,\frac{3\,(\cos^2(\theta)+\sin^2(\phi)\sin^2(\theta))}{8\,\pi}\,, \tag{3.13}$$

$$\mathrm{d}P^{(\mathrm{V})}_{\mathrm{photon}}(\mathbf{r}) = \mathrm{d}\Omega\,\frac{3\,(\cos^2(\theta)+\cos^2(\phi)\sin^2(\theta))}{8\,\pi}\,. \tag{3.14}$$

In Appendix C the general expression for arbitrary oscillation directions can be found.

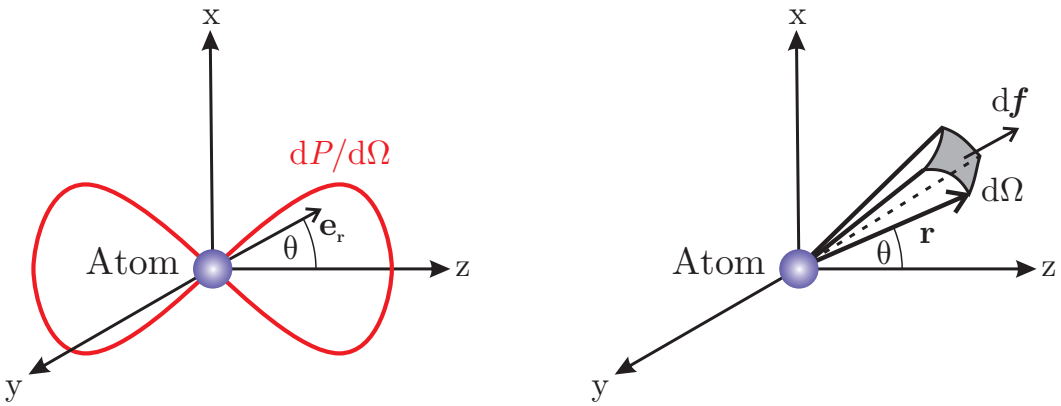

Figure 3.1: Schematic of the dipole emission characteristics and definition of energy flux per differential solid angle.

Projection onto the Cartesian coordinate system

Equations (3.9) to (3.14) are presented in spherical coordinates. This is useful if the atom is positioned right in the center of the coordinate system. For atoms shifted to the position $\mathbf{r}'$ it is much more handy to use the Cartesian coordinate system. The Cartesian coordinates (x, y, z) of a point can be obtained by substituting the following formulae for the spherical coordinates (r, θ, ϕ):

$$\begin{aligned} r &= \sqrt{x^2 + y^2 + z^2}\,, \\ \theta &= \arccos\left(\frac{z}{\sqrt{x^2 + y^2 + z^2}}\right), \\ \phi &= \operatorname{arctan2}(y, x)\,. \end{aligned} \tag{3.15}$$

[2]

However, only transforming the coordinates of a point $P(r, \theta, \phi)$ in space is not sufficient to correctly project the dipole emission characteristic into Cartesian coordinates. If a spherical wavefront emitted in a solid angle $\mathrm{d}\Omega$ is directly projected locally onto a plane, a stretched wavefront is obtained (Fig. 3.2). To correct this, the so-called projection factor between the differential solid angle and the surface element must be included. It can be easily derived by considering differential elements of the spherical wavefront and its projection onto a plane. As depicted in Figure 3.2, the differential curved wavefront is compressed by a factor of $\cos(\theta)$ compared to its projection onto a plane. This leads to the following substitution [76]:

$$\mathrm{d}\Omega = \mathrm{dA}\,\cos(\theta)\,. \tag{3.16}$$

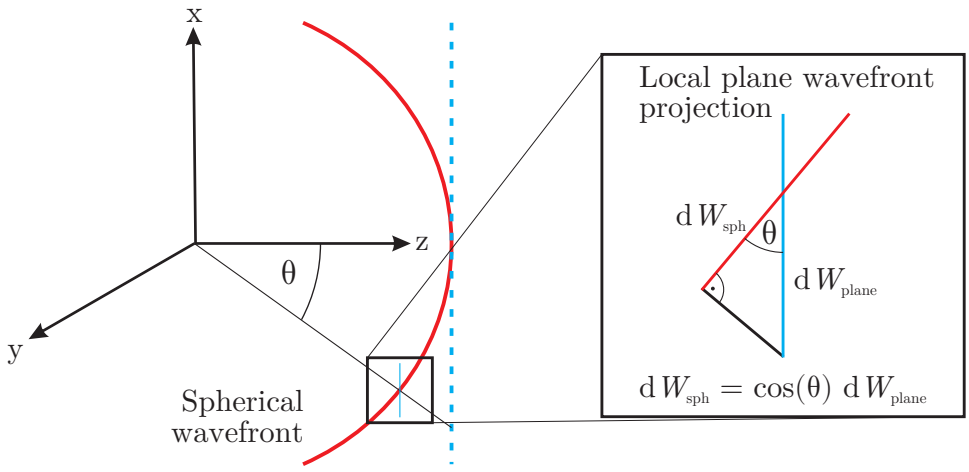

Figure 3.2: Local projection of a spherical wavefront onto a plane. The projection factor $\cos(\theta)$ can be easily derived by considering the differential elements of spherical wavefront and its projection onto the plane.

[2] The two argument function $\operatorname{arctan2}(y, x)$ is identical with $\arctan(y/x)$ for $x > 0$. In all other cases ($x \leq 0 \wedge y \in \mathbb{R}$), arctan2 guarantees the correct transformation between ϕ of polar/cylindrical/spherical coordinates and Cartesian coordinates.

Since the previous argument is valid for every intersection of a curved wavefront and a plane, the projection factor $\cos(\theta)$ is independent of r or ϕ.
Applying the above-mentioned transformation rules, the following emission characteristic is obtained:

$$\mathrm{d}P^{(\mathrm{i})}_{\mathrm{photon}}(\mathbf{r}) = \frac{1}{N_{\mathrm{norm}}}\,\mathrm{d}A\,\frac{z}{\sqrt{x^2+y^2+z^2}}\,(x^2+y^2+z^2)\,\mathbf{E}^{(\mathrm{i})}(\mathbf{r})\cdot(\mathbf{E}^{(\mathrm{i})}(\mathbf{r}))^*, \tag{3.17}$$

The expressions for the emission characteristic of π, $\sigma^{\pm}$, H and V polarized photons described in Cartesian coordinates are given by:

$$\mathrm{d}P^{(\pi)}_{\mathrm{photon}}(\mathbf{r}) = \mathrm{dA}\,\frac{3\,z}{8\,\pi\,(x^2+y^2+z^2)^{5/2}}\,(x^2+y^2)\,, \tag{3.18}$$

$$\mathrm{d}P^{(\sigma^{\pm})}_{\mathrm{photon}}(\mathbf{r}) = \mathrm{d}A\,\frac{3\,z}{8\pi\,(x^2+y^2+z^2)^{3/2}}\,\frac{(x^2+y^2+2z^2)}{2}\,, \tag{3.19}$$

$$\mathrm{d}P^{(\mathrm{H})}_{\mathrm{photon}}(\mathbf{r}) = \mathrm{dA}\,\frac{3\,z}{8\,\pi\,(x^2+y^2+z^2)^{5/2}}\,(y^2+z^2)\,, \tag{3.20}$$

$$\mathrm{d}P^{(\mathrm{V})}_{\mathrm{photon}}(\mathbf{r}) = \mathrm{dA}\,\frac{3\,z}{8\,\pi\,(x^2+y^2+z^2)^{5/2}}\,(x^2+z^2)\,. \tag{3.21}$$

The expression for arbitrary oscillation direction can be found in Appendix C.

3.1.2 Collection efficiency

The collection efficiency is defined by the probability that a photon is emitted into the entrance pupil of the objective. With regard to the previous subsection, it is obtained by a surface integral over the entrance pupil of Equation 3.9 respectively 3.17. The special case that the position of the atom $\mathbf{r}'$ is located in the center of the dipole trap ($\mathbf{r}' = 0$) is investigated in this subsection. The spherical coordinate system used is defined in Figure 3.3. The microscope objective collects photons up to a maximal polar angle θ_{max}. Therefore, the collection efficiency depends on the numerical aperture NA and the refractive index n of the material between atom and objective:

$$\eta^{(\mathrm{i})}_{\mathrm{col}}(\mathbf{r}'=0) = \int \mathrm{d}P^{(\mathrm{i})}_{\mathrm{photon}}(\mathbf{r}) \tag{3.22}$$

$$= N_{\mathrm{norm}}\int_{\mathrm{pupil}} \mathrm{d}\Omega\; r^2\;\mathbf{E}^{(\mathrm{i})}(\mathbf{r})\cdot(\mathbf{E}^{(\mathrm{i})}(\mathbf{r}))^* \tag{3.23}$$

$$= N_{\mathrm{norm}}\int_0^{\theta_{\mathrm{max}}} \mathrm{d}\theta \int_0^{2\pi} \mathrm{d}\phi\,\sin(\theta) r^2\;\mathbf{E}^{(\mathrm{i})}(\mathbf{r})\cdot(\mathbf{E}^{(\mathrm{i})}(\mathbf{r}))^* \tag{3.24}$$

$$\text{with } \theta_{\mathrm{max}} = \arcsin\left(\frac{\mathrm{NA}}{n}\right) \tag{3.25}$$

Assuming a numerical aperture of 0.5 and vacuum between atom and objective, the following collection efficiencies are obtained:

$$\eta^{(\mathrm{H})}_{\mathrm{col}}(\mathbf{r}'=0) = \eta^{(\mathrm{V})}_{\mathrm{col}}(\mathbf{r}'=0) = \eta^{(\sigma^{\pm})}_{\mathrm{col}}(\mathbf{r}'=0) = 9.41\,\% \tag{3.26}$$

$$\eta^{(\pi)}_{\mathrm{col}}(\mathbf{r}'=0) = 1.29\,\% \tag{3.27}$$

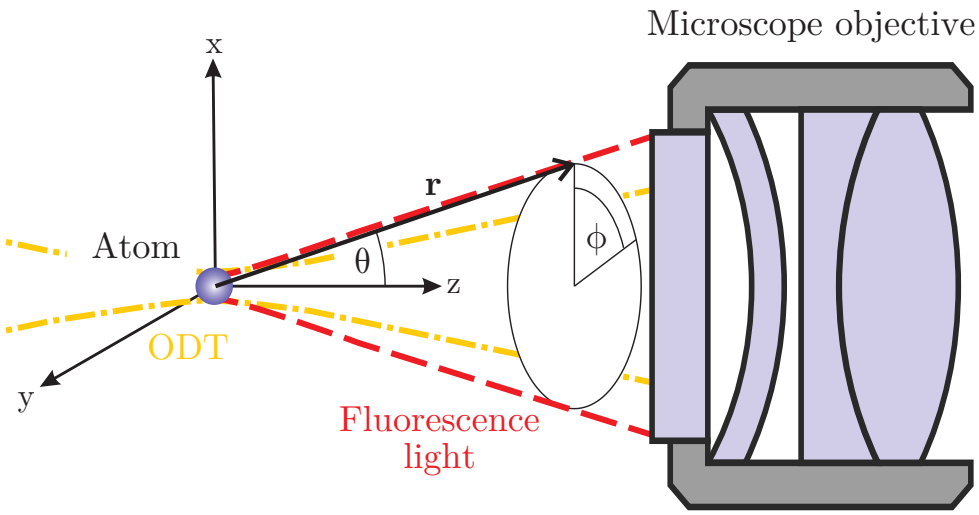

Figure 3.3: Definition of the spherical coordinate system for non displaced calculations of the collection efficiency $\mathbf{r}' = 0$. The position of the atom, the center of the dipole trap and the origin of the spherical coordinate system coincide. The two angles θ and ϕ are defined according to the diagram. The microscope objective collects photons up to an angle $\theta_{\max}$, which depends on the numerical aperture.

The collection efficiency of H, V (and $\sigma^{\pm}$) polarized photons is equal such that the collection process does not influence the uniformly distributed collection of entangled H, V (or $\sigma^{\pm}$) photons (Eq. 2.6). Due to the specific emission characteristic of π polarized photons, the probability to collect them is suppressed. In Figure 3.4 (a) the collection efficiency in dependency of the numerical aperture is shown. By using objectives with higher NA than 0.5, the probability to collect photons increases as well. This improvement factor with regard to an NA of 0.5 is depicted in Figure 3.4 (b).

The next iterative step of improving the collection performance would be a microscope objective with a NA of 0.6. This would increase the collection efficiency to 13.6 %, an improvement factor of 1.45 which results in an increase of 2.09 in atom-atom entanglement rate. The theoretical maximum of a dry lens is 0.95 [77]. This results in a collection efficiency of 37.9 %, an improvement factor of 4.03 and an increase of 16.24 in atom-atom entanglement rate. It is possible to build objectives with even higher numerical apertures [78], but then the quantum memory must be embedded in liquids or solids with a significant larger refractive index than 1. In this experiment this leads to interactions with the atom and ruins the coherence between atomic and photonic qubit. An implementation of nitrogen-vacancy centers, isolated in diamond and operating as qubits would be possible [24].

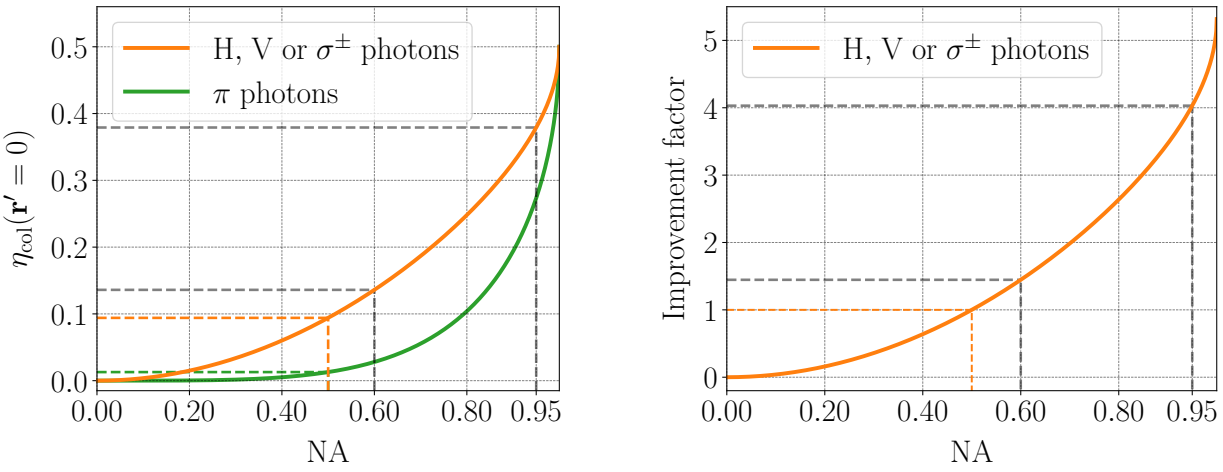

(a) Collection efficiency of H, V or $\sigma^{\pm}$ and π photons.

(b) Improvement factor for H, V or $\sigma^{\pm}$ photons with regard to the current NA.

Figure 3.4: Collection efficiency respectively improvement factor in dependency of the NA. The example of a realistic future improvement of the NA to 0.6 and the theoretical maximum of 0.95 are shown as well.

Effect of the window of the vacuum chamber

In previous considerations (see Figure 3.3), the glass window of the vacuum chamber was completely neglected. Refraction at the glass plate leads to a larger effective acceptance angle θ_{max} and therefore to a higher numerical aperture (see Fig. 3.5). The deviation x between the optical path with and without the glass plate can be easily derived by applying geometrical optics:

$$x = d\left[\tan(\theta) - \frac{\sin(\theta)}{\sqrt{n^2 - \sin^2(\theta)}}\right] \tag{3.28}$$

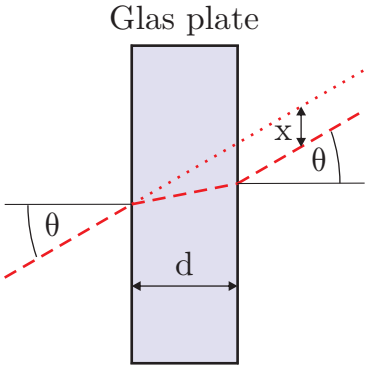

Figure 3.5: Refraction at the window of the vacuum chamber changes the numerical aperture.

with the refractive index n and the thickness d of the glass plate. By introducing the effective entrance pupil radius of the objective R_{eff}, the effect of the glass plate can be included in the general expression of the numerical aperture:

$$\mathrm{NA} = \sin(\theta_{\mathrm{max}}) = \frac{R_{\mathrm{eff}}}{\sqrt{f^2 + R_{\mathrm{eff}}^2}}, \quad \text{with } R_{\mathrm{eff}} = \begin{cases} R_0 + x, & \text{with glass plate} \\ R_0, & \text{without glass plate} \end{cases} \tag{3.29}$$

where R_0 denotes the radius of the entrance pupil. Since the microscope objective is custom-made for the purpose of this experiment, the window of the vacuum chamber is

already included in the optical design with a numerical aperture of 0.5. Therefore, the following calculations consider the existence of the glass plate by adopting Eq. 3.29 with the focal length $f = 10\,\mathrm{mm}$ and $R_{\mathrm{eff}} = \mathrm{NA}\, f / \left(\sqrt{1 - \mathrm{NA}^2}\right) = 5.77\,\mathrm{mm}$.

3.1.3 Collection efficiency for displaced atoms

Since atoms inside an ODT are not fixed to the center of the trap, the collection efficiency for off-center atoms must be considered as well. The emission profile $\mathrm{d}P^{\mathrm{i}}_{\mathrm{photon}}(\mathbf{r})$ of an atom at the position $\mathbf{r}'$ can be described by applying a transformation of the coordinate system $\mathbf{r} \rightarrow \mathbf{r} - \mathbf{r}' = (x - x', y - y', z - z')$ (see Figure 3.6). Though, the origin of the coordinate system $\sum$ is still in the center of the trap and the position of the objective is unchanged in this coordinate system. Therefore, the integration over the entrance pupil in the $\sum$ coordinate system, can be performed as before.

$$\eta^{(\mathrm{i})}_{\mathrm{col}}(\mathbf{r}') = \int \mathrm{d}P^{(\mathrm{i})}_{\mathrm{photon}}(\mathbf{r} - \mathbf{r}') \tag{3.30}$$

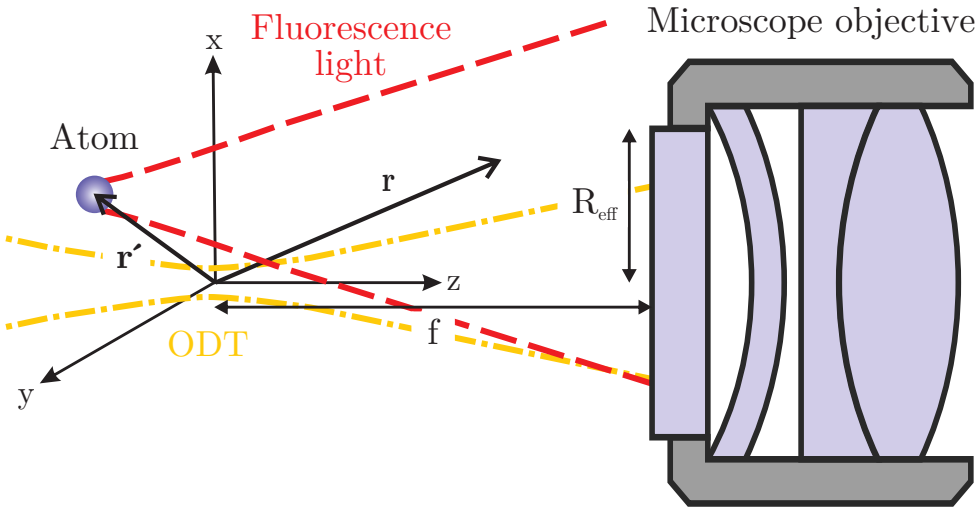

Figure 3.6: Definition of the Cartesian coordinate system for the estimation of the collection efficiency $\eta^{(\mathrm{i})}_{\mathrm{col}}(\mathbf{r}')$. The position of the atom is defined by the coordinates $\mathbf{r}'$. The emission characteristic is then given by the relative coordinates $\mathrm{d}P^{(\mathrm{i})}_{\mathrm{photon}}(\mathbf{r} - \mathbf{r}')$. The entrance pupil of the microscope objective has a radius of R_{eff} and is located at the position $\mathbf{r} = (0, 0, f)$.

Since the position of the atom is arbitrary within the density distribution of the ODT, there are no symmetries left which simplify the integration. Thus, it is more handy to perform the integration in the Cartesian description. The collection efficiencies for an

atom at position $\mathbf{r}'$ for H,V and π polarization are given by

$$\eta_{\mathrm{col}}^{(\mathrm{H})}(\mathbf{r}') = \int_{-R_{\mathrm{eff}}}^{R_{\mathrm{eff}}} \mathrm{d}x \int_{-\sqrt{R_{\mathrm{eff}}^2-x^2}}^{\sqrt{R_{\mathrm{eff}}^2-x^2}} \mathrm{d}y \, \frac{3\,(f-z')\,((y-y')^2+(f-z')^2)}{8\,\pi\,((x-x')^2+(y-y')^2+(f-z')^2)^{5/2}}\,, \tag{3.31}$$

$$\eta_{\mathrm{col}}^{(\mathrm{V})}(\mathbf{r}') = \int_{-R_{\mathrm{eff}}}^{R_{\mathrm{eff}}} \mathrm{d}x \int_{-\sqrt{R_{\mathrm{eff}}^2-x^2}}^{\sqrt{R_{\mathrm{eff}}^2-x^2}} \mathrm{d}y \, \frac{3\,(f-z')\,((x-x')^2+(f-z')^2)}{8\,\pi\,((x-x')^2+(y-y')^2+(f-z')^2)^{5/2}}\,, \tag{3.32}$$

$$\eta_{\mathrm{col}}^{(\pi)}(\mathbf{r}') = \int_{-R_{\mathrm{eff}}}^{R_{\mathrm{eff}}} \mathrm{d}x \int_{-\sqrt{R_{\mathrm{eff}}^2-x^2}}^{\sqrt{R_{\mathrm{eff}}^2-x^2}} \mathrm{d}y \, \frac{3\,(f-z')\,((x-x')^2+(y-y')^2)}{8\,\pi\,((x-x')^2+(y-y')^2+(f-z')^2)^{5/2}}\,. \tag{3.33}$$

As shown in Figure 3.6, the radius of the entrance pupil is R_{eff} and the center of the entrance pupil is at position $(0, 0, f)$. In Figure 3.7, the collection efficiency for displacement of the atom in the three dimensions is depicted. Since the results for H and V polarization coincide when x'- and y'-axis are interchanged, only H and π polarization is shown. The displacement of the atom is given in units of standard deviations of the thermal distribution $\sigma_{\mathrm{r}} = 135.7\,\mathrm{nm}$ and $\sigma_{\mathrm{z}} = 1.45\,\mu\mathrm{m}$.

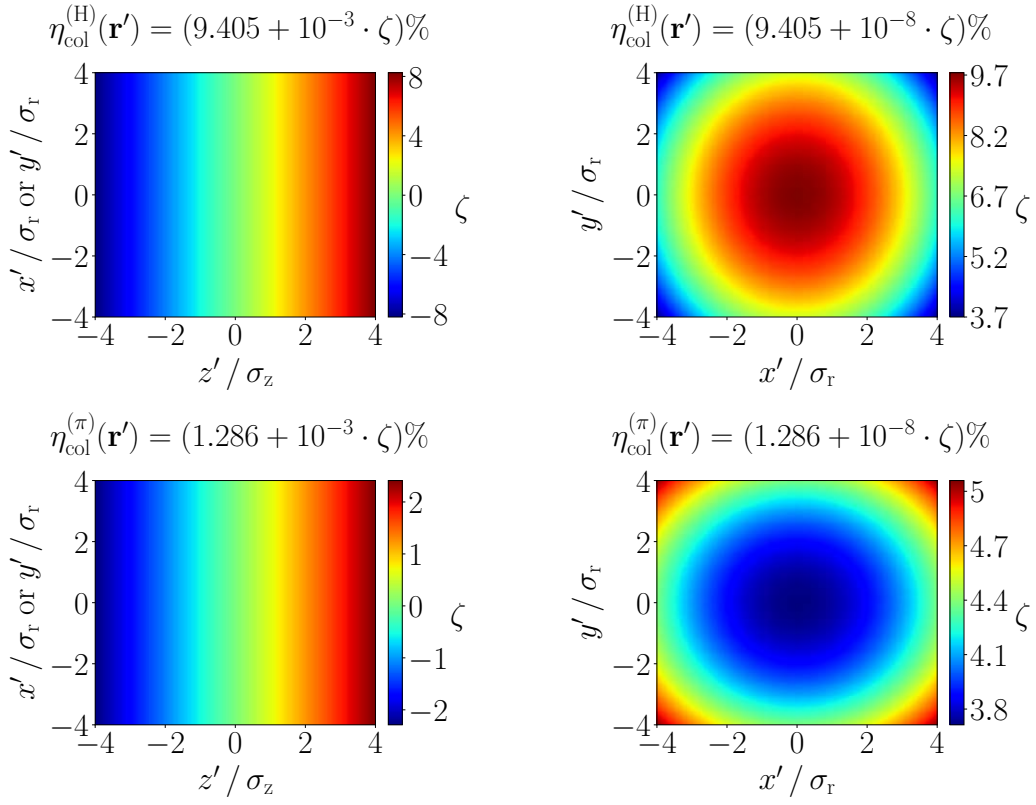

Figure 3.7: Collection efficiencies for H and π photons as a function of displacement of the atom from the center of the trap. The displacement is given in units of standard deviations of the thermal distribution $\sigma_{\mathrm{r}} = 135.7\,\mathrm{nm}$ and $\sigma_{\mathrm{z}} = 1.45\,\mu\mathrm{m}$. The collection efficiency for each plot is defined in the title and depends on the variable ζ, which defines the colorbar. Within the dimensions of the ODT, the collection probability does not change significantly.

The collection efficiency does not change significantly within the dimensions of the ODT. The largest changes result from longitudinal displacements along the z-axis. This is due to the large value of σ_z compared with σ_r and the resulting change in acceptance angle θ_{max}. Transverse displacements lead to negligible changes of the collection probability within the dimension of the trap.

For objectives with a larger numerical aperture, a significant change of this behavior is not to be expected. For objectives with much smaller NA's, the spot size of the dipole trap is larger and thus the density distribution is wider. Furthermore, the acceptance angle θ_{max} is smaller. This leads to a larger deviation of collection efficiency within the dimensions of the trap.

3.2 Coupling efficiency

After calculating the probability to collect photons with the objective, the coupling process is left for considerations. The coupling efficiency defines the probability that an already collected photon is coupled into a single mode fiber. To simplify this calculation, the objective is considered as a thin lens. Though, the thin lens adopts all optical properties of the objective like focal length, aperture diameter and the optical aberrations. Figure 3.8 depicts the simplified situation. Since the entrance pupil and the principle plane of the thin lens coincides, the coupling probability can be calculated easily as shown subsequently.

3.2.1 Definition of coupling efficiency

The coupling efficiency can be estimated by the overlap of the emitted photon mode $\mathbf{E}_{photon}$ and the mode of the fiber $\mathbf{E}_{fiber}$. The plane, at which this overlap is calculated (overlap plane), is located somewhere between the position of the thin lens and the fiber collimator (Figure 3.8):

$$\eta_{coup}^{(i,j)}(\mathbf{r}', w_{coll}) = \left| \frac{\int \mathrm{d}A \; \mathbf{E}_{photon}^{(i)}(\mathbf{r}-\mathbf{r}') \cdot (\mathbf{E}_{fiber}^{(j)}(\mathbf{r}, w_{coll}))^*}{N_{photon}^{(i)}(\mathbf{r}') \; N_{fiber}^{(j)}(w_{coll})} \right|^2 . \tag{3.34}$$

Since the objective collimates the mode of the emitted photon, it projects the electric field onto a plane. Therefore, it is not necessary to include the projection factor $\cos(\theta)$ in Equation 3.34. By expressing $\mathbf{E}_{photon}^{(i)}$ in its Cartesian representation, the overlap integration can be performed by using only Cartesian coordinates. Due to the aperture of the objective respectively the thin lens $A_{objective}$, the mode of the emitted photon is truncated. It is assumed that the dimension of the aperture of the fiber collimator $A_{collimator}$ is chosen such that it does not clip the fiber mode significantly. Therefore, the integration range can be reduced to the aperture of the fiber collimator. Nevertheless, for meaningful results both

modes must be normalized:

$$N^{(i)}_{\text{photon}}(\mathbf{r}') = \left| \int \mathrm{d}A \; \mathbf{E}^{(i)}_{\text{photon}}(\mathbf{r}-\mathbf{r}') \cdot (\mathbf{E}^{(i)}_{\text{photon}}(\mathbf{r}-\mathbf{r}'))^* \right|^{1/2} \tag{3.35}$$

$$N^{(j)}_{\text{fiber}}(w_{\text{coll}}) = \left| \int \mathrm{d}A \; \mathbf{E}^{(j)}_{\text{fiber}}(\mathbf{r}, w_{\text{coll}}) \cdot (\mathbf{E}^{(j)}_{\text{fiber}}(\mathbf{r}, w_{\text{coll}}))^* \right|^{1/2}, \tag{3.36}$$

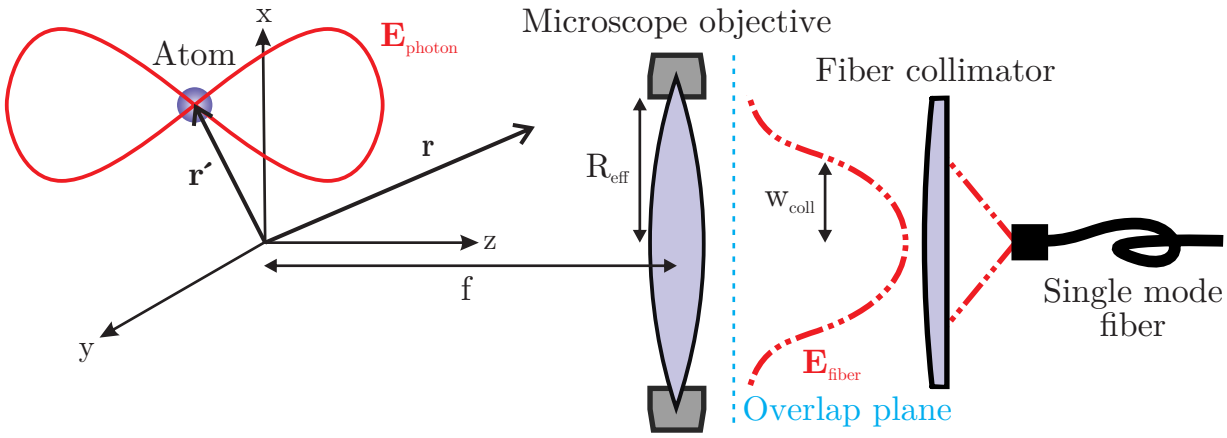

Figure 3.8: Coupling efficiency scheme. The coupling efficiency η_{coup} is defined by the overlap of the emitted photon mode $\mathbf{E}_{\text{photon}}$ and the fiber mode $\mathbf{E}_{\text{fiber}}$. The overlap is calculated at the overlap plane between objective in the thin lens approximation and the fiber collimator. The collimated waist w_{coll} of the fiber mode can be adjusted by choosing a suitable fiber collimator.

where $\mathbf{E}^{(i)}_{\text{photon}}$ is defined by Eq. 3.2 and its Cartesian coordinate system representation for H,V and π photons is given by:

$$\mathbf{E}^{(\mathrm{H})}_{\text{photon}}(\mathbf{r}-\mathbf{r}') = \frac{k^2}{4\,\pi\,\epsilon_0\,\epsilon_{\mathrm{r}}} \frac{e^{i\,k\,(\sqrt{(x-x')^2+(y-y')^2+(z-z')^2}-\sqrt{x^2+y^2+z^2}+z)}}{((x-x')^2+(y-y')^2+(z-z')^2)^{3/2}} \begin{pmatrix} (y-y')^2+(z-z')^2 \\ -(x-x')\,(y-y') \\ -(x-x')\,(z-z') \end{pmatrix}, \tag{3.37}$$

$$\mathbf{E}^{(\mathrm{V})}_{\text{photon}}(\mathbf{r}-\mathbf{r}') = \frac{k^2}{4\,\pi\,\epsilon_0\,\epsilon_{\mathrm{r}}} \frac{e^{i\,k\,(\sqrt{(x-x')^2+(y-y')^2+(z-z')^2}-\sqrt{x^2+y^2+z^2}+z)}}{((x-x')^2+(y-y')^2+(z-z')^2)^{3/2}} \begin{pmatrix} -(x-x')\,(y-y') \\ (x-x')^2+(z-z')^2 \\ -(y-y')\,(z-z') \end{pmatrix}, \tag{3.38}$$

$$\mathbf{E}^{(\pi)}_{\text{photon}}(\mathbf{r}-\mathbf{r}') = \frac{k^2}{4\,\pi\,\epsilon_0\,\epsilon_{\mathrm{r}}} \frac{e^{i\,k\,(\sqrt{(x-x')^2+(y-y')^2+(z-z')^2}-\sqrt{x^2+y^2+z^2}+z)}}{((x-x')^2+(y-y')^2+(z-z')^2)^{3/2}} \begin{pmatrix} -(x-x')\,(z-z') \\ -(y-y')\,(z-z') \\ (x-x')^2+(y-y')^2 \end{pmatrix}. \tag{3.39}$$

Since the mode is truncated by the aperture of the objective, Equations 3.37 to 3.39 are only valid for $x, y \in A_{\text{objective}}$. Outside of this region, the electric field vanishes. Moreover,

the phase takes the phase shift (the collimation effect) of the lens into account. The LP_{01}[3] mode $\mathbf{E}^{(j)}_{\text{fiber}}$ of the single mode fiber, a Bessel function first kind of zeroth order, can be approximated by a Gaussian function

$$\mathbf{E}^{(j)}_{\text{fiber}}(\mathbf{r}, w_{\text{coll}}) = \begin{cases} \frac{1}{\sqrt{\frac{\pi}{2}} w_{\text{coll}}} \, e^{-\frac{x^2+y^2}{w^2_{\text{coll}}}} \begin{pmatrix} c_{\text{H}} \\ c_{\text{V}} \\ 0 \end{pmatrix}, & \text{for } x, y \in A_{\text{collimator}} \\ 0, & \text{for } x, y \notin A_{\text{collimator}} \end{cases} \tag{3.40}$$

where $|c_{\text{H}}|^2 + |c_{\text{V}}|^2 = 1$. It was assumed that the electric field inside the single mode fiber is only transversely polarized [79]. Therefore, the H polarization of the fiber ($j = \text{H}$) is given by $c_{\text{H}} = 1,\ c_{\text{V}} = 0$ and the V polarization ($j = \text{V}$) by $c_{\text{H}} = 0,\ c_{\text{V}} = 1$. The waist w_{coll} of the collimated Gaussian fiber mode can be adjusted by using a suitable fiber collimator.

3.2.2 Coupling efficiency calculations

In principle it is possible to calculate the overlap and therefore the coupling between the H, V or π photon and the H or V polarization of the fiber mode. However, some combinations are equal. The linearly independent cases are given by:

- The same polarization as emitted is coupled into the fiber: $(i, j) = $ (H,H) or (V,V)
- The orthogonal polarization as emitted is coupled into the fiber: $(i, j) = $ (H,V) or (V,H)
- π polarized photon is coupled into the fiber: $(i, j) = (\pi$,H) or (π,V)

Subsequently, the three different linearly independent possibilities are discussed further. For each of the three cases, the coupling into the H polarized fiber mode is assumed. A coupling into the V polarized fiber mode is obtained by interchanging x' and y' coordinates.

Coupling of the same polarization as emitted (H,H)

The coupling efficiency η_{coup} depends on the spatial location of the atom which emits a photon and on the width of the fiber mode in the overlap plane. Figure 3.9 depicts the dependency on the Gaussian width w_{coll} for several atom emission positions. If the atom is located in the center of the trap, a maximal overlap between emitted photon and fiber mode of $\eta_{\text{coup}} = 80.3\,\%$ for $w_{\text{coll}} = 0.85\, R_{\text{eff}}$ is achieved. Increasing or decreasing the width w_{coll} leads to a reduced overlap. The same happens if the atom is shifted from the center of the dipole trap. A transverse shift to the position $x' = 2\,\sigma_{\text{r}}$ with $\sigma_{\text{r}} = 135.7\,\text{nm}$ decreases the coupling efficiency to 63.5 %. Since a $2\,\sigma_{\text{r}}$ shift in y direction leads to slightly lower overlap of 62.2 %, the coupling efficiency has no rotational symmetry. However, it

[3] Lowest order linearly polarized propagation mode of optical fibers.

is completely symmetric with respect to reflections at the coordinate hyperplanes spanned by the three axes (see Equation 3.37). A longitudinal shift of $2\,\sigma_z$ with $\sigma_z = 1.45\,\mu m$ has a drastic impact on the coupling efficiency which decreases to 36.1 %. The dependency of the coupling efficiency on displacements of the atom in the three dimensions is shown in Figure 3.10. In general, any shift of the atom from the center of the trap decreases the coupling into a single mode fiber. In this process, the influence of longitudinal shifts is more dramatic. Furthermore, the Gaussian width value $w_{\mathrm{coll}_{\max}}$, which maximizes the curve $\eta_{\mathrm{coup}}(w_{\mathrm{coll}})$ at a specific position $\mathbf{r}'$, decreases for increasing atom displacements.

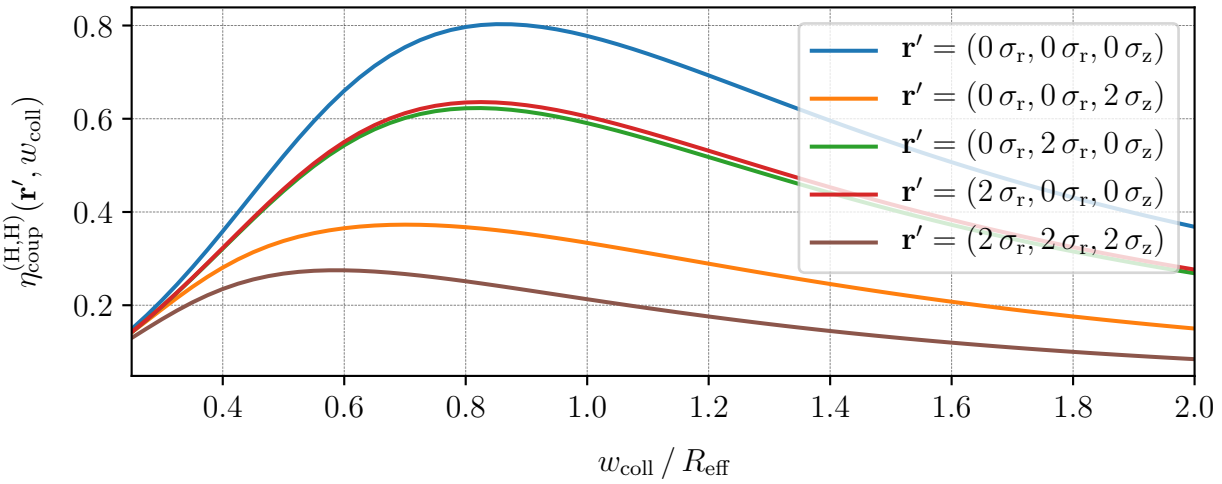

Figure 3.9: Coupling efficiency versus width of the collimated fiber mode w_{coll} in units of the effective entrance pupil radius of the objective R_{eff} for several displacements of the atom position from the center of the trap. The relative position of the atom is given in units of standard deviations of the thermal distribution $\sigma_r = 135.7\,nm$ and $\sigma_z = 1.45\,\mu m$. The probability to find the atom in a region of $\pm 2\sigma_i$ from the center of the trap is given by 95.45 %.

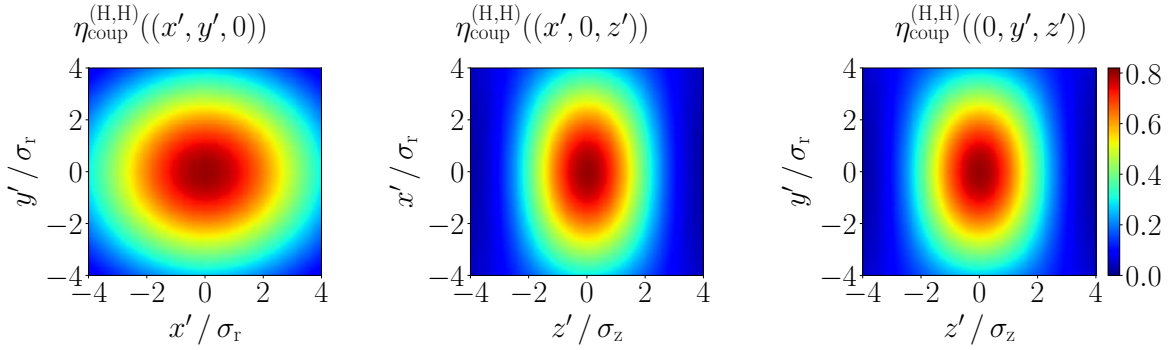

(a) $x'y'-$plane. (b) $x'z'-$plane. (c) $y'z'-$plane.

Figure 3.10: Coupling efficiency versus the spatial location of the atom in the three dimensions. In all three figures, a Gaussian width of $0.85\,R_{\mathrm{eff}}$ is assumed.

Coupling of the orthogonal polarization as emitted (V,H)

While the coupling between the same polarizations of the modes leads to reasonable high efficiencies, the coupling between orthogonal polarizations of the two modes is highly suppressed. In general, the coupling probabilities are orders of magnitude ($\sim 10^4$) less than in the previously presented situation. As shown in Figure 3.11 and 3.12, the overlap is only finite, if the position of the atom is shifted diagonally in the $x'y'$-plane. If either the x' or the y' coordinate is zero, the coupling efficiency vanishes as well. Moreover, a longitudinal shift decreases the coupling into the single mode fiber. The overlap between orthogonal polarizations of the fiber and emitted photon mode, reveal a mirror symmetry with respect to the center of the trap.

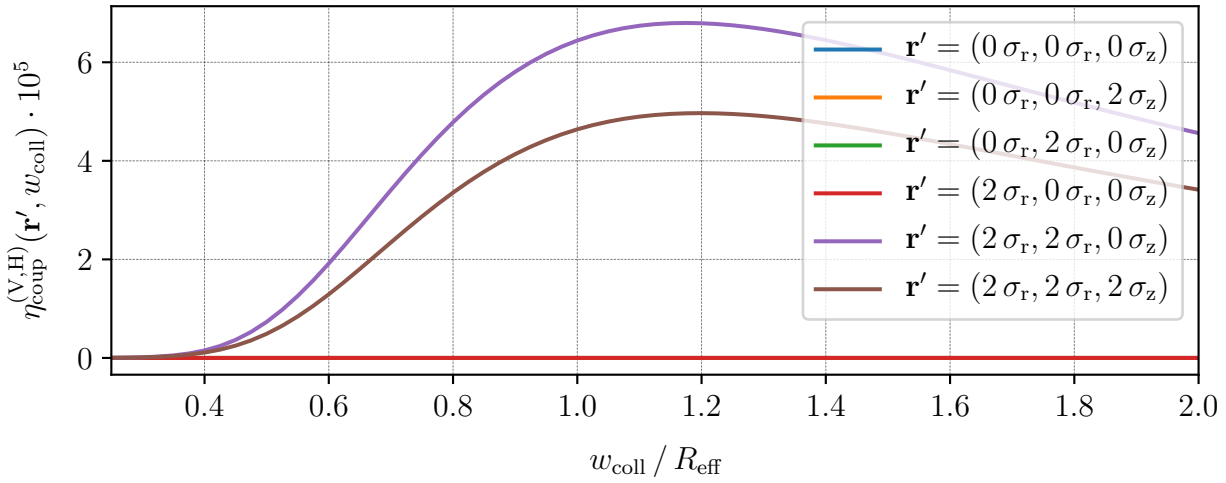

Figure 3.11: Coupling efficiency versus width of the collimated fiber mode w_{coll} in units of the effective entrance pupil radius of the objective R_{eff} for several displacements of the atom position from the center of the trap. The relative position of the atom is given in units of standard deviations of the thermal distribution $\sigma_\mathrm{r} = 135.7\,\mathrm{nm}$ and $\sigma_\mathrm{z} = 1.45\,\mu\mathrm{m}$.

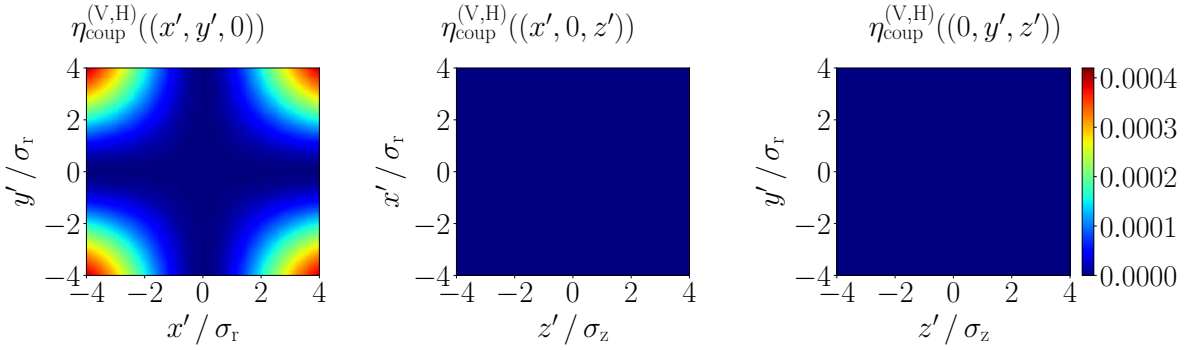

(a) $x'y'-$plane. (b) $x'z'-$plane. (c) $y'z'-$plane.

Figure 3.12: Coupling efficiency versus the spatial location of the atom in the three dimensions. In all three figures, a Gaussian width of $0.85\,R_{\mathrm{eff}}$ is assumed.

Coupling of π photons (π,H)

The coupling efficiency for π photons in the center of the trap vanishes as well. If the atom is located in the center of the optical dipole trap, only H polarized photons can couple to the H polarized fiber mode. However, if the atom is displaced along the x'-axis, π photons can couple to the H polarized fiber mode too (see Figure 3.13 and 3.14). In this process, the corresponding coupling efficiency is only around one order of magnitude lower than in the (H,H) situation. If the x' displacement of the atom vanishes, the π photon can not couple to the H polarized fiber mode anymore. A longitudinal displacement leads to a decrease in coupling probability. $\eta_{\text{coup}}^{(\pi,\text{H})}(\mathbf{r}', w_{\text{coll}})$ reveals a mirror symmetry with regard to the $y'z'$-plane.

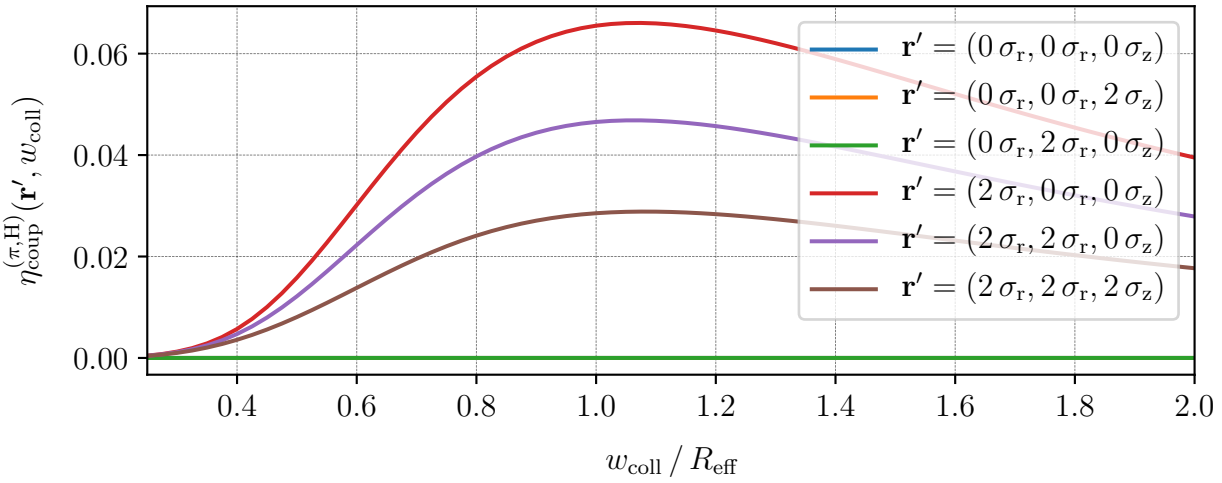

Figure 3.13: Coupling efficiency versus width of the collimated fiber mode w_{coll} in units of the effective entrance pupil radius of the objective R_{eff} for several displacements of the atom position from the center of the trap. The relative position of the atom is given in units of standard deviations of the thermal distribution $\sigma_\text{r} = 135.7\,\text{nm}$ and $\sigma_\text{z} = 1.45\,\mu\text{m}$.

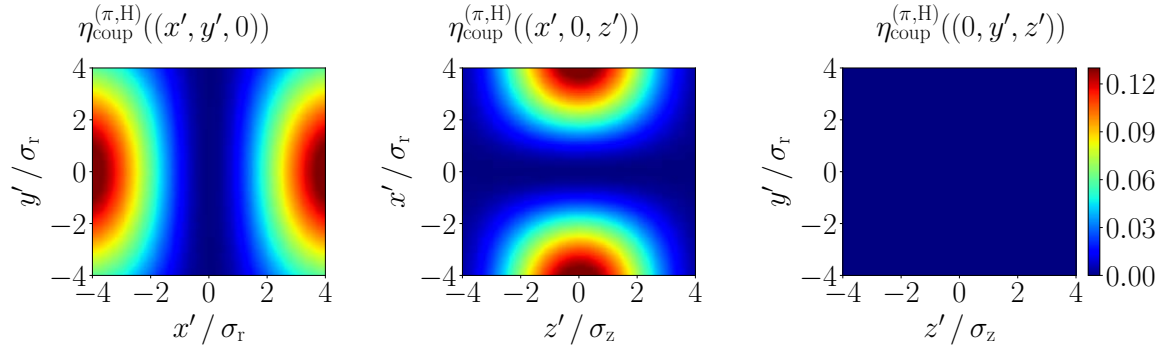

(a) $x'y'-$plane. (b) $x'z'-$plane. (c) $y'z'-$plane.

Figure 3.14: Coupling efficiency versus the spatial location of the atom in the three dimensions. In all three figures, a Gaussian width of $0.85\,R_{\text{eff}}$ is assumed.

3.3 Collection and coupling efficiency for the thermal distribution

After simulating the collection efficiency in Section 3.1 and the coupling efficiency in Section 3.2, in this section the overall collection and coupling efficiency η_{cc} is estimated. It describes the probability that an atom located in an ODT spontaneously decays and emits a photon which is successfully collected and coupled into a single mode fiber. This probability is described by a multiplication of the collection efficiency and coupling efficiency. Though, the three situations discussed in Subsection 3.2.2 can occur. However, their probabilities are not only determined by the mode overlap, but also by the decay probability of the atomic state. Due to the decay channels of the $5^2\mathrm{P}_{3/2}$, F' = 0 state, an emission of H or V photons is more likely than an emission of π photons. This leads to a suppression of the collection and coupling of π photons in contrast to the other two coupling possibilities. Furthermore, the atom is thermally distributed within the dipole trap. Hence, to obtain the overall collection and coupling probability, the individual efficiencies for each position $\mathbf{r}'$ must be integrated[4] with regard to the thermal distribution function $n(\mathbf{r}', T)$ (see Subsection 2.2.3):

$$\eta_{\mathrm{cc}}^{(i,j)}(w_{\mathrm{coll}}) = c^{(i)} \int_{\mathrm{trap}} \mathrm{d}V \; n(\mathbf{r}', T) \; \eta_{\mathrm{col}}^{(i)}(\mathbf{r}') \; \eta_{\mathrm{coup}}^{(i,j)}(\mathbf{r}', w_{\mathrm{coll}}) \; , \tag{3.41}$$

$$\text{with } c^{(i)} = \begin{cases} 1/3, & \text{for } i = \pi \\ 2/3, & \text{for } i \neq \pi \end{cases} \tag{3.42}$$

where $c^{(i)}$ denotes the decay channel probability.

Figure 3.15 depicts the overall collection and coupling efficiency for an optically trapped atom at a temperature of $T = 48\,\mu\mathrm{K}$. Considering a coupling of the same polarization as emitted, a maximal collection and coupling efficiency of 3.81 % for a Gaussian fiber width of $w_{\mathrm{coll}} = 0.82\,R_{\mathrm{eff}}$ is obtained. Due to the effects explained in Chapter 2, the collection and coupling of π photons leads to a loss in fidelity of the atom-photon entanglement. This fidelity loss is even higher, if an H photon couples to the V polarized mode of the fiber. However, these two effects are highly suppressed and nearly negligible. Their collection and coupling efficiencies are given by $\eta_{\mathrm{cc}}^{(\pi,\mathrm{H})\vee(\pi,\mathrm{V})}(w_{\mathrm{coll}}/R_{\mathrm{eff}} = 0.82) = 5.54 \times 10^{-3}\,\%$ and $\eta_{\mathrm{cc}}^{(\mathrm{H},\mathrm{V})\vee(\mathrm{V},\mathrm{H})}(w_{\mathrm{coll}}/R_{\mathrm{eff}} = 0.82) = 2.30 \times 10^{-5}\,\%$. Therefore, the assumption in Chapter 2, that the Λ-system leads to an entangled pair of photonic and atomic qubit, which maintains during the collection and coupling process, is justified. Nevertheless, the effect of (V,H) or (π,H) coupling increases when the trapping region of the ODT expands. This is either possible due to a larger focus of the dipole trap laser, a lower dipole trap or higher temperatures of the atom.

[4]Since numerical built-in integration algorithms fail due to the large number of variables, a look up table of the collection and coupling efficiencies for individual atom displacements $\mathbf{r}'$ is created first. Afterwards the volume integration is performed using the 3D trapezoidal rule [80].

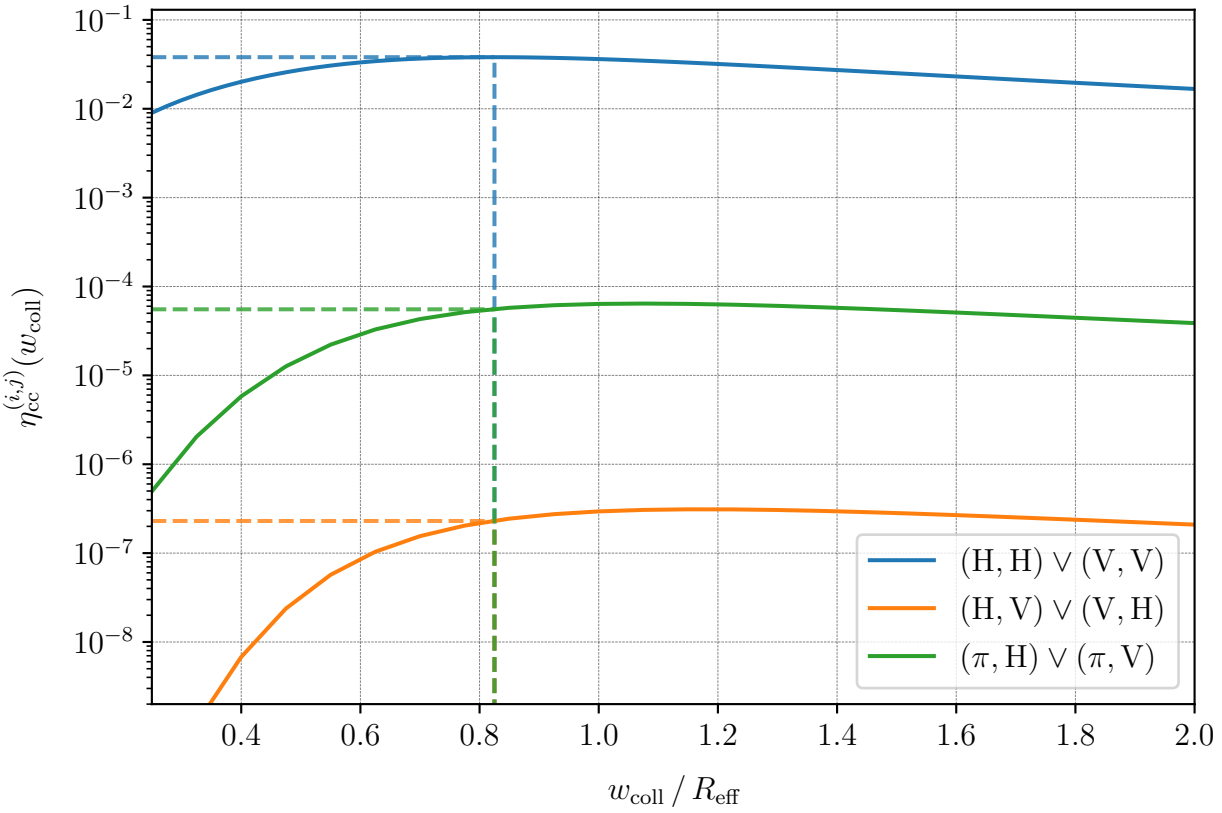

Figure 3.15: Plot of the collection and coupling efficiency $\eta_{\mathrm{cc}}^{(i,j)}(w_{\mathrm{coll}})$ in logarithmic scale. Assuming a coupling of the same polarization as emitted, the maximal collection and coupling probability is $\eta_{\mathrm{cc}}^{(\mathrm{H},\mathrm{H})\vee(\mathrm{V},\mathrm{V})}(w_{\mathrm{coll}}/R_{\mathrm{eff}} = 0.82) = 3.81\,\%$. The probabilities that either the orthogonal polarization as emitted is coupled into the fiber or a π photon is coupled into the fiber are negligible.

In contrast to the collection and coupling efficiency simulations of [81], the overall efficiencies presented in this thesis are lower. Even an objective with a numerical aperture of 0.6 only leads to an overall collection and coupling probability of 5.52 %. The assumed coupling efficiency of 80 % in [81] suggests that the thermal distribution is not considered or the ion trap is very deep. As shown in Section 3.2, a coupling efficiency of 80 % can only be achieved if the atom is located in the center of the ODT.

To test the simulated results of the collection and coupling efficiency, a comparison with experimental data can be made. The success probability of detecting atom-photon entanglement presented in Subsection 2.5.2 is a well known quantity. The new high NA microscope optical setup described in [55] achieved a success probability of $P_{\mathrm{A,P,exp}}(d \approx 3\,\mathrm{m}) \approx 6.8\,‰$. Considering the following efficiencies: state preparation $\eta_{\mathrm{pump}} \approx 0.8$, excitation $\eta_{\mathrm{exc}} = 0.8$, detection $\eta_{\mathrm{det}} \approx 0.55 \pm 0.10$ and the simulated collection and coupling efficiency $\eta_{\mathrm{cc}}^{(\mathrm{H},\mathrm{H})\vee(\mathrm{V},\mathrm{V})}(w_{\mathrm{coll}}/R_{\mathrm{eff}} = 0.7) = 3.67\,\%$, yields a success probability of

$P_{\mathrm{A,P,sim}}(d \approx 3\,\mathrm{m}) \approx (1.29 \pm 0.24)\,\%$ according to Eq. 2.15. Further sources of losses are the fiber losses (fiber attenuation, losses due to an optical splice, losses of fiber to fiber connectors), the interference filter before the APD, losses of the fiber beam splitter respectively the PBS and the losses of about 25 anti-reflective coated surfaces. These lead to an additional factor of $\sim 0.92 \pm 0.05$. Therefore, a simulated success probability of $P_{\mathrm{A,P,sim}}(d \approx 3\,\mathrm{m}) \approx (1.19 \pm 0.23)\,\%$ is obtained. The difference between simulated and experimental success probability is a factor of 1.75. However, the uncertainties of several losses are high which might lead to a reduction of this factor. Furthermore, a perfectly overlapped dipole trap with the $\lambda = 780\,\mathrm{nm}$ focus spot is assumed. This assumption is not valid (see Chapter 5 and [55]). A consideration of the effect of misalignment is made in Chapter 5.

3.4 Self-made fiber collimator

The current fiber collimator used to couple single photons into the single mode fiber generates a collimated Gaussian beam with the width of $w_{\mathrm{coll}} = 0.7\,R_{\mathrm{eff}}$. Therefore, using a suitable fiber collimator with a width of $w_{\mathrm{coll}} = 0.82\,R_{\mathrm{eff}}$, a relative improvement of 3.7 % is possible. Even this small improvement is crucial for increasing the atom-atom entanglement rate. Thus, a potential fiber collimator must satisfy the following requirements:

- Diffraction limited operation at $\lambda = 780\,\mathrm{nm}$ such that it can not be assumed that optical aberrations reduce the coupling efficiency.
- $w_{\mathrm{coll}} = 0.82\,R_{\mathrm{eff}}$ waist of the collimated beam which represents the optimal $\eta_{\mathrm{coup}}(w_{\mathrm{coll}})$.
- Optimized for reduced intensity losses by using anti-reflection coated surfaces for $\lambda = 780\,\mathrm{nm}$.
- Sufficient large aperture stop such that a Gaussian beam with a waist of $w_{\mathrm{coll}} = 0.82\,R_{\mathrm{eff}}$ is not clipped.

Since there was no commercially available fiber collimator that satisfied all the aforementioned requirements, it was decided to design and assemble the desired fiber collimator by ourselves. In this process, the optical design software Zemax[5] was used. First of all, general properties of the lens design must be provided. The focal length of the system must be chosen such that a collimated Gaussian beam width of $w_{\mathrm{coll}} = 0.82\,R_{\mathrm{eff}}$ is obtained. Measuring the numerical apertures of several fibers[6], an average value of $\mathrm{NA}_{\mathrm{fiber}} \approx 0.085$ was determined. Therefore, a focal length of $f \approx 49\,\mathrm{mm}$ leads to the desired waist. A lens system containing four separated lenses provides a good trade-off between performance and simple assembly. Furthermore, the single lenses possess spherical surfaces due to a superior manufacturing quality[7]. Using aspherical surfaces, doublets or triplets lead to a

[5] Zemax Opticstudio.
[6] Thorlabs 780HP fiber.
[7] Lenses made by Lens-optics.

better performance, however the focus was placed on a simple and stable lens design. Two different optical glasses of the Schott glass catalogue [82], the borosilicate glass N-BK7 and the dense flint glass N-SF6 are used. The refractive index of the two glasses are chosen to be as different as possible ($n_{\text{N-BK7}} = 1.51$ and $n_{\text{N-SF6}} = 1.79$ at $\lambda = 780\,\text{nm}$) while providing a high resistivity against influences of the environment and a high internal transmittance [82]. This provides the Zemax optimization algorithms an as large as possible range and therefore an increase in optical performance. Moreover, the lens system should be robust against manufacturing tolerances of either the surface thickness and radius (0.2 mm), the thickness of the spacer between two lenses (0.2 mm), the decenter and tilt of individual surfaces (0.2 mm, 0.2 °) respectively of individual lenses (0.2 mm, 1 °). These tolerances are chosen such that they comply with the manufacturing tolerances of the in-house workshop, which produced the mount of the lens system. After determining these general properties, Zemax optimization algorithms calculate the optimal optical design. This is shown in Figure 3.16 (a) and the lens data can be found in Appendix D. The mount of the lens system is depicted in Figure 3.16 (b) and provides the possibility to transversely adjust single lenses by screws.

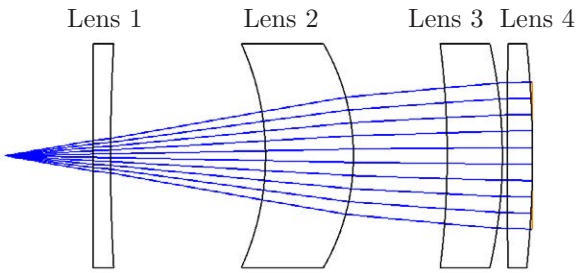

(a) Lens design of the fiber collimator. The lens system consists of four separated spherical lenses.

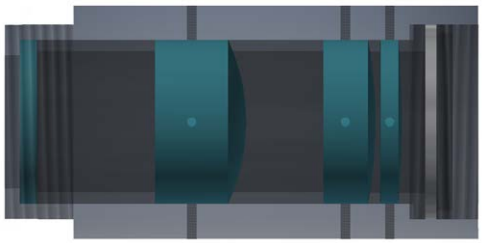

(b) Mount of the lens system. The four lenses are mounted in a custom made lens tube. All four lenses are separated by spacers. Screws can shift 3 of 4 lenses transversely.

Figure 3.16: Self-made fiber collimator.

The assumptions made previously, lead to a plug and play assembly under clean room conditions. Once the optical system is ready to use, an optomechanical system to mount and align the fiber in front of the lens system is needed. For this purpose a commercially available beam guiding system based on a cage system was used[8]. This provides the possibility to adjust the longitudinal distance between fiber and lens system using a translation stage. Furthermore, fine adjusters enable an adjustment of the transverse shift and the tip and tilt. Therefore, a full set of degrees of freedom is provided to perfectly align the single mode fiber with regard to the self-made fiber collimator. An analysis of the optical performance follows in Chapter 4.

[8]Radiant Dyes RD-BGS-TS.

Chapter 4

Characterization of optical elements

As mentioned in the previous chapters, the entanglement rate and thus the performance of applications based on entanglement over long distances depends on the collection and coupling efficiency. The coupling process into a single mode fiber depends on the mode overlap between photon and fiber mode. This mode overlap, in turn, is influenced by the performance of the involved optical elements, especially the microscope objective and the fiber collimator. In fact, any real optical system exhibits aberrations which deform the wavefront. In general, without any purpose of a controlled wavefront deformation, the occurrence of optical aberrations leads to reduced mode overlaps. The main purpose of optical system design is to control and reduce such aberrations to a degree of accuracy which is sufficient for the system performance. In this process, it is necessary to classify aberrations and characterize the most important optical elements, e.g. the microscope objective and the self-made fiber collimator.

4.1 Aberration theory

Optical aberrations can be considered in geometrical optics as well as in wave optics. The former, the ray aberrations, were especially object of research 150 years ago. In 1855, the investigation of transverse aberrations by Philipp Ludwig von Seidel led to the decomposition of third order aberrations into five constituents, the so-called Seidel aberrations [83]. Nowadays, ray aberrations (longitudinal, transverse and angular aberrations) are primarily used in optical design softwares based on geometrical optics, e.g. Zemax. The main object of the current research in the field of optical aberrations are wave aberrations, since they provide some unique benefits [84]:

- Wave aberrations can be measured directly and accurately by interferometric methods.

- Wave aberrations are strongly related to the physical image formation. They are an essential input for diffraction integrals.

- The wave aberrations of an optical system can be decomposed into the sum of wave aberrations of individual surfaces.

In this thesis, only wave aberrations are considered henceforth.
The wave aberrations W are defined as the deviation of the wavefront emerging from the exit pupil of a real optical system (aberrated wavefront) and the wavefront emerging from an ideal optical system (reference wavefront). Therefore, wave aberrations are defined in the image space and are strongly related to the image location and image distortion. In this process, the wavefront indicates the locus $\mathbf{r}$ of constant optical path measured from the object point OP. The optical path l_{op} is given by the geometrical distance along rays multiplied with the local refractive index $n(\mathbf{r}')$:

$$l_{\mathrm{op}}(\mathbf{r}) = \int_{OP}^{\mathbf{r}} \mathrm{d}\mathbf{r}'\, n(\mathbf{r}')\,. \tag{4.1}$$

Therefore, wave aberrations are given by the optical path difference Δl_{op} between aberrated and reference wavefront. Scaling the optical path length in units of wavelength λ, an optical path difference of λ leads to a phase difference of 2π. Using this convention, the aberrated electric field $\mathbf{E}$ in the exit pupil of an optical system can be written as:

$$\mathbf{E}(x_{\mathrm{p}}, y_{\mathrm{p}}) = \mathbf{E}_0(x_{\mathrm{p}}, y_{\mathrm{p}})\; e^{\frac{2\pi i}{\lambda} W(x_{\mathrm{p}}, y_{\mathrm{p}})}\,. \tag{4.2}$$

The amplitude is denoted by $\mathbf{E}_0$ and the wave aberration by

$$W(x_{\mathrm{p}}, y_{\mathrm{p}}) = \Delta l_{\mathrm{op}}(x_{\mathrm{p}}, y_{\mathrm{p}}) \;=\; l_{\mathrm{op}}(x_{\mathrm{p}}, y_{\mathrm{p}}) - l_{\mathrm{op}}(0,0)\,, \tag{4.3}$$

where $l_{\mathrm{op}}(0,0)$ defines the optical path length of the reference wavefront [85].
For ideal imaging, the wavefronts are concentric spheres centered in the image or object point. If the focal point and object point coincides, the image plane is at infinity and the wavefronts emerging from the exit pupil are flat planes. In isotropic media, the wavefronts are perpendicular to rays (see Figure 4.1).

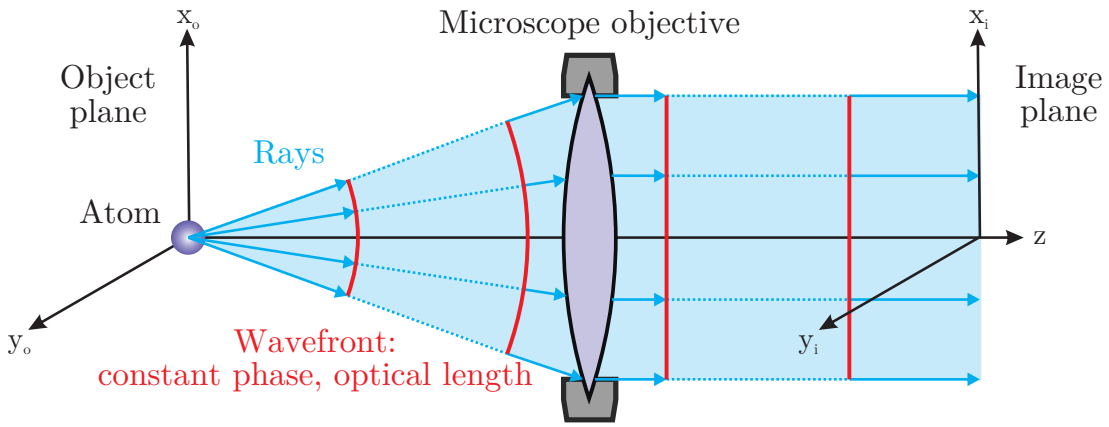

Figure 4.1: Illustration of the definition of Wavefronts.

However, the form of the wavefront emerging from the exit pupil of a real optical system can be exceedingly complex. Basically it is the result of several random errors in design, fabrication and assembly. Even if optical systems are well made and carefully assembled, they posses certain aberrations that are inherent in their design [86].

An example of a simple wavefront aberration is shown in Figure 4.2. If the optical system induces a small angle $\theta = -\partial W(x_\mathrm{p}, y_\mathrm{p}) / (n\, \partial x_\mathrm{p})$ between the aberrated wavefront and the unaberrated wavefront, the complete image is tilted by this angle. Hence, this wave aberration is called tilt. An optical system that induces a wave aberration of $W(x_\mathrm{p}, y_\mathrm{p}) = x_\mathrm{p}^2 + y_\mathrm{p}^2 / (2\,\Delta z)$ to an originally collimated beam (see Figure 4.3), leads to a converging beam. The focus occurs at the distance Δz from the exit pupil. This wave aberration is denoted as defocus [86].

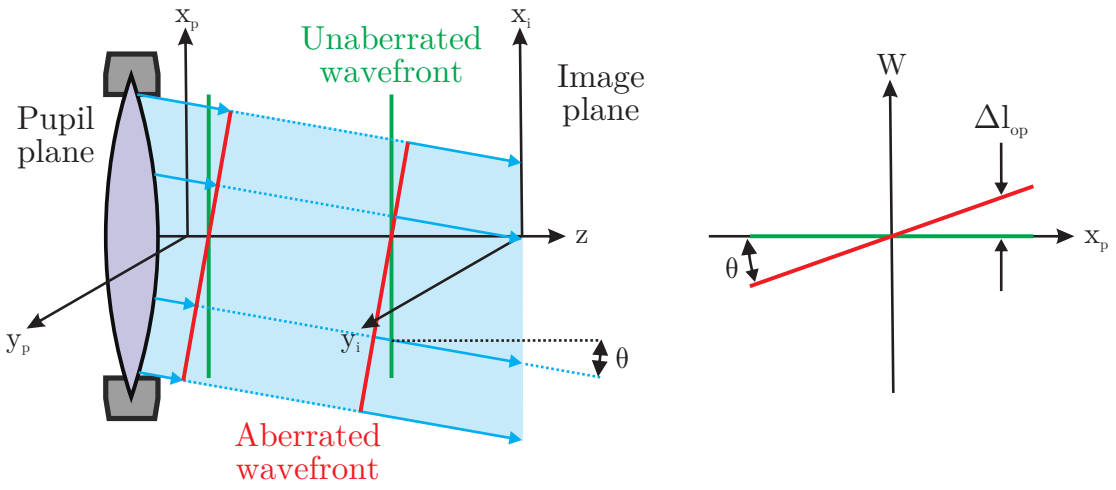

Figure 4.2: Illustration of the tilt wave aberration.

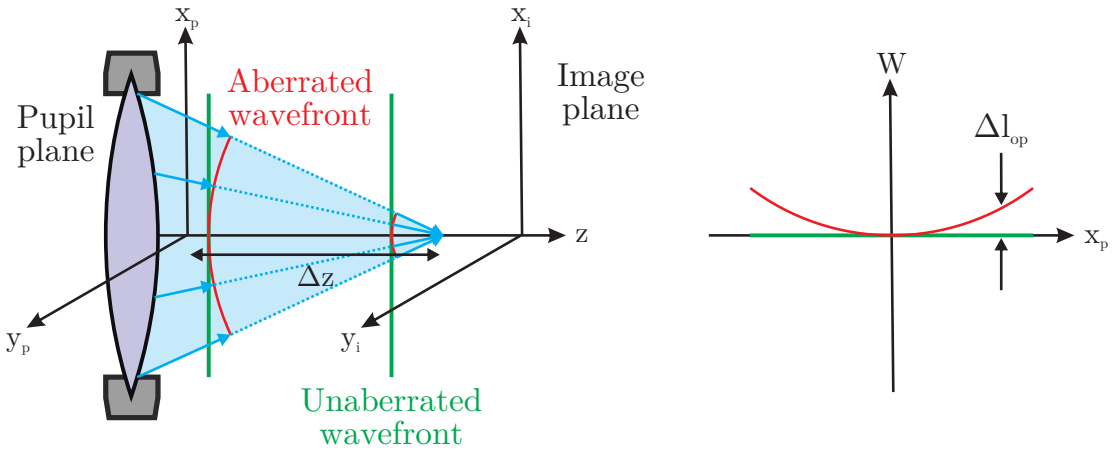

Figure 4.3: Illustration of the defocus wave aberration.

4.1.1 Wavefront definitions and wave aberration criteria

In general, the reference wavefront is chosen according to the paraxial sphere and the chief ray respectively. This means the center of the reference wavefront is given by the image point. The radius R of the reference wavefront is usually chosen such that the reference wavefront contains the intersection point between chief ray and optical axis (see Figure 4.4). If the optical system operates as a collimator, the radius of the reference wavefront goes to infinity. Then, the reference wavefront is a plane and the chief ray defines the normal vector.

Even if the reference wavefront is well-defined, there is still some arbitrariness for the definition of the wave aberrations. A global displacement of the aberrated wavefront with regard to the reference wavefront only induces a global phase shift, which has no effect on the image. Therefore, it is convenient to choose the global phase of the aberrated wavefront such that the mean value of the wave aberration vanishes (see Figure 4.4):

$$W_{\mathrm{mean}} = \langle W \rangle = \frac{1}{A_{\mathrm{ep}}} \int \mathrm{d}x_{\mathrm{p}} \int \mathrm{d}y_{\mathrm{p}}\, W(x_{\mathrm{p}}, y_{\mathrm{p}}) = 0 \tag{4.4}$$

where $A_{\mathrm{ep}} = \int \mathrm{d}x_{\mathrm{p}} \int \mathrm{d}y_{\mathrm{p}}\, 1$ denotes the area of the exit pupil. Furthermore, the sign of the deviation between aberrated and reference wavefront plays an important role. In this thesis, the following convention is used. If the aberrated wavefront leads the reference wavefront, the optical path difference and therefore the wave aberration is positive $W > 0$ (see Equation 4.3). A positive wave aberration introduces a negative focal shift. As shown in Figure 4.3 the aberrated beam is stronger convergent. On the other hand, a negative aberration $W < 0$ introduces a stronger divergence of the beam [85].

To quantify the deviation of a wavefront from the reference wavefront, several measures can be introduced. The simplest one is the peak-to-valley value W_{pv}. As depicted in Figure 4.4, it is the maximal deviation of the aberrated wavefront from the reference wavefront in both positive and negative directions:

$$W_{\mathrm{pv}} = \max_{x_{\mathrm{p}},\, y_{\mathrm{p}} \in A_{\mathrm{ep}}} \left[W(x_{\mathrm{p}}, y_{\mathrm{p}})\right] \; - \min_{x_{\mathrm{p}},\, y_{\mathrm{p}} \in A_{\mathrm{ep}}} \left[W(x_{\mathrm{p}}, y_{\mathrm{p}})\right]. \tag{4.5}$$

Although it is convenient and easy to quantify wave aberrations with W_{pv}, it can be misleading since the maximal wavefront error includes no information of the area over which this error occurs. Therefore, the root mean squared value W_{rms} is in general more meaningful:

$$W_{\mathrm{rms}} = \sqrt{\langle W^2 \rangle - \langle W \rangle^2} = \sqrt{\frac{1}{A_{\mathrm{ep}}} \int \mathrm{d}x_{\mathrm{p}} \int \mathrm{d}y_{\mathrm{p}}\, \left[W(x_{\mathrm{p}}, y_{\mathrm{p}}) - W_{\mathrm{mean}}\right]^2}\,. \tag{4.6}$$

If apodization is considered, the intensity distribution must be included as an additional factor in each integral of Equation 4.6 [84]. Note, that due to the definition of Equation 4.2 and 4.3, the wave aberration W and the corresponding criteria W_{pv}, W_{rms} are given in

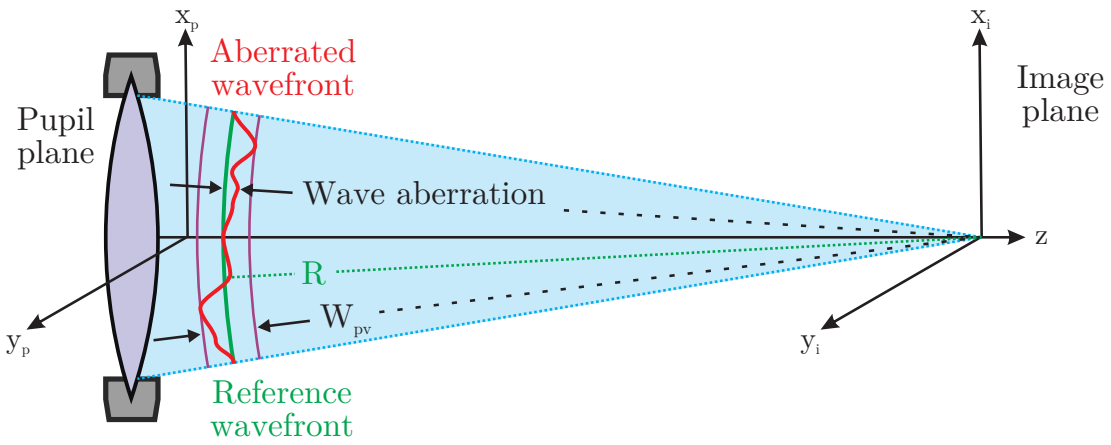

Figure 4.4: Illustration of the definition of wave aberration and peak-to-valley value. The reference wavefront is chosen such that its center coincides with the image point. The aberrated wavefront differs from the reference wavefront by the wave aberration. The mean value of the wave aberration vanishes. The maximal and minimal value of the wave aberration defines the peak-to-valley value.

units of wavelength λ.

If the performance of an optical system is only reduced by the theoretical limit of diffraction and not by wave aberrations, the system is called diffraction limited. In fact every system, independent of the amount of aberrations, is inherently diffraction limited. However, it is common to denote an aberration-free system as mentioned. The first idea of how to specify an image-quality criterion was given by Lord Rayleigh [87]. Assuming the focal point of an optical system without any aberrations, all Huygens wavelets emerging from the exit pupil are in phase. According to Rayleigh, an aberration introduced phase shift up to $\lambda/4$ has only little effect on the intensity of the focus and therefore aberrations can be considered as unimportant [87]. Expressed in mathematical terms, this leads to the

$$\text{Rayleigh wavefront criterion:} \quad W_{\text{pv}} \leq \frac{\lambda}{4}\,. \tag{4.7}$$

Since the usage of the peak-to-valley value can be misleading, a generalization of the Rayleigh criterion for the rms value was introduced. Considering a system which only contains defocus, $W_{\text{pv}} = \lambda/4$ can be rewritten in terms of the rms value, yielding the [84]

$$\text{Marechal criterion:} \quad W_{\text{rms}} \leq \frac{\lambda}{\sqrt{192}} \approx \frac{\lambda}{14}\,. \tag{4.8}$$

Even if this generalization of the Rayleigh criterion is defined for defocus, it can be used for other types of aberrations as well.

4.1.2 Zernike polynomials expansion

In contrast to the well-known Seidel aberrations presented in Appendix E, the image field independent wave aberration description with Zernike polynomials shows a close connection to the measurements of wavefronts while preserving the direct relation to Seidel aberrations. The Zernike polynomials represent a complete orthogonal set of a polynomial expansion of the wave aberrations. They are defined by coordinates in the polar representation of the normalized circular exit pupil ($x_\mathrm{p} = \rho\sin(\phi)$, $y_\mathrm{p} = \rho\cos(\phi)$ with $0 \leq \rho \leq 1$ and $0 \leq \phi \leq 2\pi$):

$$W(\rho,\phi) = \sum_{\mathrm{n}} \sum_{\mathrm{m}=-\mathrm{n}}^{\mathrm{n}} c_{\mathrm{nm}}\, Z_\mathrm{n}^\mathrm{m}(\rho,\phi)\,, \tag{4.9}$$

where Z_n^m denotes the Zernike polynomial of radial order n and azimuthal order m and c_{nm} defines the corresponding coefficient. The polynomials split up in a radial term $R_\mathrm{n}^\mathrm{m}(\rho)$ and an azimuthal term. In the standard representation [88], they are given by:

$$Z_\mathrm{n}^\mathrm{m}(\rho,\phi) = R_\mathrm{n}^\mathrm{m}(\rho) \begin{cases} \sqrt{2(n+1)}\sin(\mathrm{m}\phi)\,, & \text{for m} < 0 \\ \sqrt{2(n+1)}\cos(\mathrm{m}\phi)\,, & \text{for m} > 0 \\ \sqrt{(n+1)}\,, & \text{for m} = 0 \end{cases} \tag{4.10}$$

$$\text{with } R_\mathrm{n}^\mathrm{m}(\rho) = \sum_{\mathrm{s}=0}^{\frac{\mathrm{n}-\mathrm{m}}{2}} \frac{(-1)^\mathrm{s}\,(\mathrm{n}-\mathrm{s})!}{\mathrm{s}!\,(\frac{\mathrm{n}+\mathrm{m}}{2}-\mathrm{s})!\,(\frac{\mathrm{n}-\mathrm{m}}{2}-\mathrm{s})!}\,\rho^{\mathrm{n}-2\mathrm{s}}\,. \tag{4.11}$$

The indices n and m obey the following restrictions: $\mathrm{n}-\mathrm{m}$ is even and $|\mathrm{m}| \leq \mathrm{n}$. The most important Zernike polynomials are shown in Table 4.1. For a more intuitive presentation, the fringe numbering convention[1] is used. Therefore, the first four Zernike polynomials are the field independent representations of the zeroth and first order wave aberrations. These aberrations can be corrected trivially by only adjusting the position or the scale of the image. The next five terms represent the well-known Seidel aberrations (see Appendix E) which lead to real aberrations. In this thesis, only two fifth order wave aberration terms are considered. They are known as trefoil and correspond to a superposition of elliptical coma terms (a secondary fifth order wave aberration [84]). A clear and intuitive presentation of the different Zernike polynomials is given by an arrangement in a checkerboard pattern (see [85]).

Properties of Zernike polynomials

Zernike polynomials are designed to be orthonormal over the unit circle:

$$\frac{1}{\pi}\int_0^{2\pi}\mathrm{d}\phi\int_0^1\mathrm{d}\rho\,\rho\,Z_\mathrm{n}^\mathrm{m}(\rho,\phi)\,Z_\mathrm{n'}^\mathrm{m'}(\rho,\phi) = \delta_{\mathrm{n,n'}}\delta_{\mathrm{m,m'}}\,. \tag{4.12}$$

[1] The jth Zernike polynomial is defined by

$$\mathrm{j(n,m)} = \left(1+\frac{1+|\mathrm{m}|}{2}\right)^2 - 2|\mathrm{m}| + \frac{1-\mathrm{sign(m)}}{2}\,,\ \text{with sign(m)} = \begin{cases} 1, & \text{for m} \geq 0 \\ -1, & \text{for m} < 0 \end{cases}.$$

Number j	Radial order n	Azimuthal order m	Functional representation	Interpretation
1	0	0	1	Piston
2	1	1	$2\,\rho\sin(\phi)$	Tilt in x
3	1	-1	$2\,\rho\cos(\phi)$	Tilt in y
4	2	0	$\sqrt{3}\,(2\rho^2-1)$	Defocus
5	2	2	$\sqrt{6}\,\rho^2\sin(2\phi)$	Astigmatism 45°
6	2	-2	$\sqrt{6}\,\rho^2\cos(2\phi)$	Astigmatism 0°
7	3	1	$\sqrt{8}\,(3\rho^3-2\rho)\sin(\phi)$	Coma x
8	3	-1	$\sqrt{8}\,(3\rho^3-2\rho)\cos(\phi)$	Coma y
9	4	0	$\sqrt{5}\,(6\rho^4-6\rho^2+1)$	Spherical
10	3	3	$\sqrt{8},\rho^3\sin(3\phi)$	Trefoil 30°
11	3	-3	$\sqrt{8}\,\rho^3\cos(3\phi)$	Trefoil 0°

Table 4.1: Overview over the most important Zernike polynomials in standard convention and fringe numbering.

Since the polynomials are not orthogonal for parts of the full unit circle, they are not suitable for describing ring apertures etc. Due to the orthogonality, the single Zernike coefficients c_{nm} can be easily obtained, if the wave aberration $W(\rho,\phi)$ is known:

$$c_{\mathrm{nm}} = \frac{1}{\pi}\int_0^{2\pi}\mathrm{d}\phi\int_0^1\mathrm{d}\rho\,\rho\,Z_{\mathrm{n}}^{\mathrm{m}}(\rho,\phi)\,W(\rho,\phi)\,. \tag{4.13}$$

Therefore, a wavefront measurement by a Shack-Hartmann sensor for example, leads directly to the involved Zernike coefficients. This is the reason why Zernike polynomials are often used to analyze experimental wave aberration data. However, to describe local wavefront distortions, a large number of orders of Zernike polynomials is needed. In practice, a number of 36 is sufficient to guarantee smooth wavefronts [85]. Furthermore, the root mean square criteria of wave aberrations W_{rms} can be easily calculated for these polynomials. Since the different aberration terms are orthogonal, the individual aberrations sum up leading to the simple expression [84]:

$$W_{\mathrm{rms}} = \sqrt{\sum_{\mathrm{n}}\sum_{\mathrm{m=-n}}^{\mathrm{n}} c_{\mathrm{nm}}^2}\,. \tag{4.14}$$

In the standard convention, the peak-to-valley value is given by [84]:

$$W_{\mathrm{pv}} = \max_{\mathrm{n,\ m}} \ 2 \left| c_{\mathrm{nm}} \sqrt{\frac{2\,(\mathrm{n}+1)}{1+\delta_{\mathrm{m},0}}} \right| . \tag{4.15}$$

The maximal values of the Zernike coefficients for a diffraction limited system according to Equation 4.7 and 4.8 are shown in Table 4.2.

Aberration type	Maximal coefficient value	
	Rayleigh criterion	Marechal criterion
Defocus	$c_{20} = 0.072\,\lambda$	$c_{20} = 0.072\,\lambda$
Astigmatism	$c_{22} = c_{2-2} = 0.051\,\lambda$	$c_{22} = c_{2-2} = 0.072\,\lambda$
Coma	$c_{31} = c_{3-1} = 0.044\,\lambda$	$c_{31} = c_{3-1} = 0.072\,\lambda$
Spherical	$c_{40} = 0.056\,\lambda$	$c_{40} = 0.072\,\lambda$
Trefoil	$c_{33} = c_{3-3} = 0.044\,\lambda$	$c_{33} = c_{3-3} = 0.072\,\lambda$

Table 4.2: Maximal values for Zernike coefficients of a diffraction limited optical system.

4.2 Characterization by optical beam propagation

A qualitative method to identify aberrations of optical systems is the optical beam propagation. In this process, the optical system is investigated, for example, by collimating the Gaussian mode of an optical fiber. While increasing the distance to the optical system, distortions of the beam profile evolve due to aberrations. The rate at which the beam profile changes depends on the amount of induced aberrations. Significant aberrations lead to large distortions, while a diffraction limited system leaves the Gaussian beam nearly unperturbed. Furthermore, it is possible to draw conclusions about the type of aberrations from the symmetry of the beam profile.

In Figure 4.5 and 4.6 several intensity profiles are shown, measured by a CMOS camera[2] for different distances. Figure 4.5 depicts intensity profiles of the self-made fiber collimator in case of imperfect alignment. The distance z between camera and collimator is defined in terms of its Gouy phase $\eta(z) = \arctan\,(z/z_{\mathrm{R}})$. Since the Rayleigh length is roughly 71 m, only Gouy phases up to $0.2\,\pi$ could be measured without using any optical element between collimator and camera. Using a lens, which projects infinity to the focal point, enables measurements up to a Gouy phase of $0.5\,\pi$. However, any optical element induces further aberrations and falsifies the measurement. As shown in Figure 4.5, the beam profile deformations increase with increasing distance z. The asymmetry of the deformations

[2] IDS UI-3370CP Rev. 2.

hypothesize that the responsible aberrations are asymmetric as well. In case of optimized alignment of the self-made fiber collimator (Figure 4.6), the overall beam profile distortions are lower. It is reasonable that the rotationally symmetric deformations are provoked by spherical aberrations. The collimated waist of the self-made fiber collimator is $\sim 4.1\,\mathrm{mm}$ which corresponds to the optimal value of $w_{\mathrm{coll}} = 0.82\,R_{\mathrm{eff}}$ with R_{eff} the effective aperture radius of the objective.

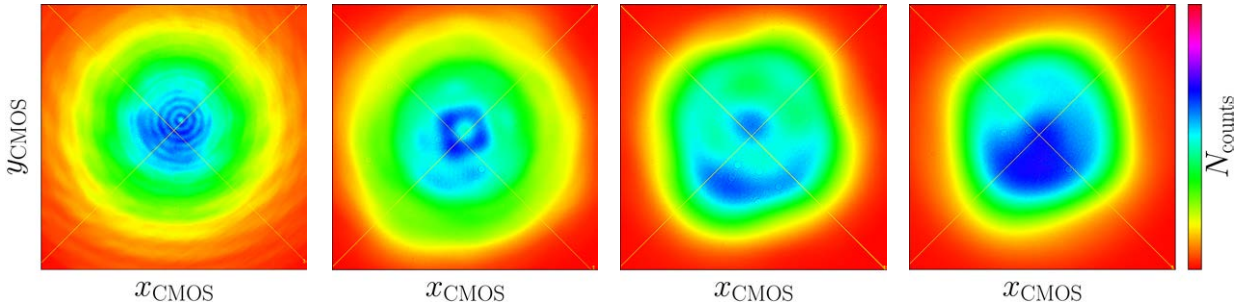

(a) $\eta(z) = 0.02\,\pi$, $z = 4\,\mathrm{m}$. (b) $\eta(z) = 0.07\,\pi$, $z = 15\,\mathrm{m}$. (c) $\eta(z) = 0.13\,\pi$, $z = 30\,\mathrm{m}$. (d) $\eta(z) = 0.18\,\pi$, $z = 44\,\mathrm{m}$.

Figure 4.5: Intensity profiles of the self-made fiber collimator in the case of imperfect alignment. The deformation of the beam increases with the Gouy phase η.

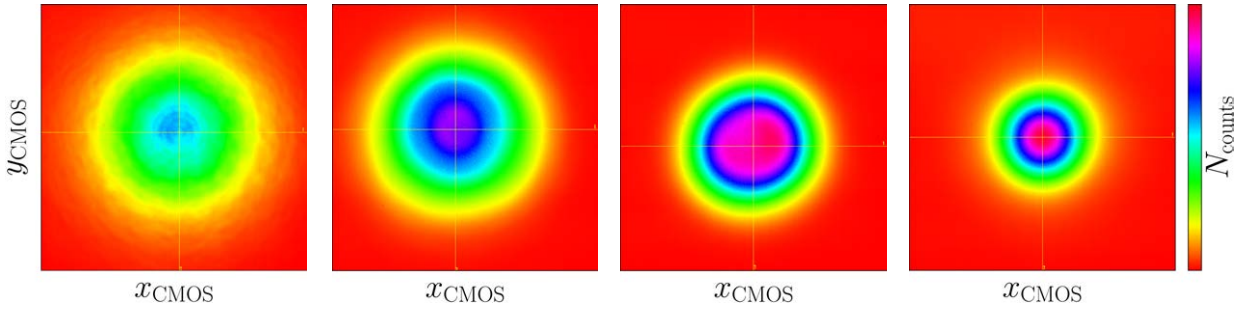

(a) $\eta(z) = 0.02\,\pi$, $z = 4\,\mathrm{m}$. (b) $\eta(z) = 0.06\,\pi$, $z = 14\,\mathrm{m}$. (c) $\eta(z) = 0.12\,\pi$, $z = 29\,\mathrm{m}$. (d) $\eta(z) = 0.18\,\pi$, $z = 44\,\mathrm{m}$.

Figure 4.6: Intensity profiles of the self-made fiber collimator in the case of perfect alignment. Up to a Gouy phase of $\eta \approx 0.1\,\pi$, the beam width expands according to a Gaussian beam. At larger Gouy phases, defocus and spherical aberrations starts to deform and shrink the beam. In general, it is only possible to collimate beams within intervals of low beam deformation.

The underlying physical process can be described by using the Fresnel-Kirchhoff diffraction formula [89]. In case of a nearly collimated beam, the formula can be simplified to:

$$\mathbf{E}(\mathbf{r}) = -\frac{i}{2\lambda} \int_{\mathrm{pupil}} \mathrm{d}A_{\mathrm{p}}\, \boldsymbol{\epsilon}_{\mathrm{s}}(\rho, \phi)\, \frac{e^{-i\,k\,r}}{r}\,, \tag{4.16}$$

where the electric field emerging from the exit pupil of the optical system is given by $\boldsymbol{\epsilon}_\mathrm{s}$ and r denotes the distance between a point of the exit pupil and the observation point (see Figure 4.7). Since Equation 4.16 only depends on the distance r, the z component of the exit pupil can be set to zero $z_\mathrm{p} = 0$. In far field approximation $z^2 \gg (x - x_\mathrm{p})^2 + (y - y_\mathrm{p})^2$, the distance r can be approximated by z. Since the phase term needs a more accurate approximation, r can be simplified by:

$$r = \sqrt{z^2 + (x - x_\mathrm{p})^2 + (y - y_\mathrm{p})^2} \tag{4.17}$$

$$\approx z \left[1 + \frac{(x - x_\mathrm{p})^2}{2\,z} + \frac{(y - y_\mathrm{p})^2}{2\,z}\right]. \tag{4.18}$$

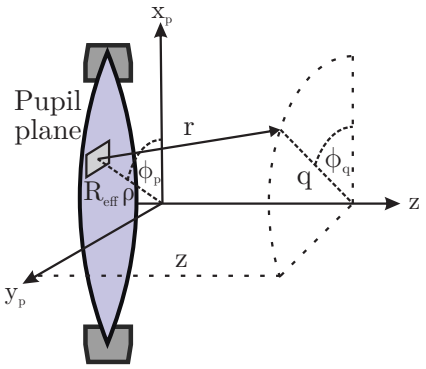

Figure 4.7: Definition of the cylindrical coordinate system and the polar coordinate system of the pupil plane.

Using cylindrical coordinates ($x = q\cos(\phi_\mathrm{q})$, $y = q\sin(\phi_\mathrm{q})$) for the observation point and polar coordinates for the exit pupil ($x_\mathrm{p} = R_\mathrm{eff}\,\rho\cos(\phi_\mathrm{p})$, $y_\mathrm{p} = R_\mathrm{eff}\,\rho\sin(\phi_\mathrm{p})$), where the radial component is normalized $0 \leq \rho \leq 1$, Equation 4.16 can be written as:

$$\mathbf{E}(\mathbf{r}) = \frac{i\,R_\mathrm{eff}^2}{\lambda\,z}\,e^{-i\,k\left(z+\frac{q^2}{2\,z}\right)}\int_0^{2\pi}\mathrm{d}\phi_\mathrm{p}\int_0^1\mathrm{d}\rho\,\rho\,\boldsymbol{\epsilon}_\mathrm{s}(\rho,\phi_\mathrm{p})\,e^{-i\,k\left[\frac{R_\mathrm{eff}^2\,\rho^2}{2\,z}-\frac{R_\mathrm{eff}\,\rho\,q}{z}\cos(\phi_\mathrm{p}-\phi_\mathrm{q})\right]}. \tag{4.19}$$

In contrast to Equation 3.40, additional phase terms must be considered for the source field $\boldsymbol{\epsilon}_\mathrm{s}$:

$$\boldsymbol{\epsilon}_\mathrm{s}(\rho,\phi_\mathrm{p}) = \mathbf{E}_0\,\frac{w_\mathrm{coll}}{w_{z_\mathrm{p}}}\,e^{-\frac{q^2}{w_{z_\mathrm{p}}^2}}\,e^{i\left[\eta_{z_\mathrm{p}}-\frac{k\,q^2}{2\,R_{z_\mathrm{p}}}+\frac{2\pi}{\lambda}\,W(\rho,\phi_\mathrm{p})\right]} \tag{4.20}$$

with w_coll the collimated waist. w_{z_p} is the beam width, η_{z_p} the Gouy phase and R_{z_p} radius of curvature ($R(z) = z\,[1 + (z_\mathrm{R}/z)^2]$) at the position of the exit pupil [90].
Using Equation 4.19 and 4.20, the field and therefore the intensity profile at a distance z for arbitrary wave aberrations $W(\rho,\phi_\mathrm{p})$ can be calculated. If the wave aberration is rotationally symmetric, the azimuthal integration of Equation 4.19 can be performed analytically and only one integral is left for numerical calculation.
Vice versa, knowing the intensity profiles at certain distances, it is possible to extract the induced wave aberrations. However, in practice two facts prevent a quantitative analysis:

- For a perfect collimated beam, the initial value of the Gouy phase η_{z_p} vanishes and the radius of curvature R_{z_p} is infinity. However, in reality it is impossible to achieve this configuration. Due to a finite amount of aberrations, the Gaussian beam deforms. If these deformations are too large, the Gaussian fit fails. Without knowing the exact aberrations, it is impossible to estimate the precise width of the deformed beam. Therefore, a perfect collimated beam can not be achieved. This leads to some nescience which makes it impossible to extract the real wave aberrations.

- In general, Equation 4.19 contains two integrals, which must be solved numerically. If arbitrary wave aberrations are included, the integrand contains highly oscillating terms which lead to numerical issues. Even if only spherical aberrations are considered and the number of numerical integrals reduces to one, hundreds of integrations must be performed to obtain a simulation of a high resolution intensity profile. Moreover, for reliable fit results, the previously described process must be performed again hundreds or even thousands of times to archive suitable values of the fit parameters. In summary, a quantitative analysis requires too much computational resources for a practical use.

Nevertheless, a qualitative analysis of the amount of aberrations in an optical system is possible (see Figure 4.5 and 4.6).

4.3 Characterization by point spread functions

In contrast to the previous section, point spread functions (PSFs) of optical systems provide a possibility to characterize optical systems quantitatively.

4.3.1 Ideal point image

For an ideal point source emitting spherical waves, diffraction effects occur, due to the finite dimension of the aperture of an optical system (see Figure 4.8). The truncation leads to an incomplete constructive interference of partial waves. Therefore, the image point is blurred in comparison with its analog, obtained by geometrical optics. The intensity distribution of the image of a single point-like source is denoted as point spread function. Since this function reflects the response of an optical system to a point source of light, it plays an important role in imaging theory. Knowing the properties of the object and the PSF, the corresponding image can be easily calculated by using the convolution theorem [89]. The point spread function itself is obtained by solving the diffraction integral of the optical system:

$$I_{\mathrm{PSF}} = \left| \int_{\mathrm{pupil}} \mathrm{d}A_{\mathrm{p}}\, E_0(\rho,\phi)\, \frac{e^{-i\,[k\,r - \frac{2\pi}{\lambda}\,W(\rho,\phi)]}}{r} \right|^2 . \tag{4.21}$$

Since the PSF depends on the source field strength E_0, the pupil aperture and the wave aberrations $W(\rho,\phi)$ of the optical system, it contains information of the light source as well as information of the optical system. Knowing the exact field strength of the light source at the pupil plane, the PSF provides the possibility to characterize the optical system in terms of numerical aperture and wave aberrations. As stated above, the original definition of a point spread function corresponds to an ideal point source. However, Equation 4.21 can be solved for extended light sources as well, leading to the same PSF. The crucial fact here is a strict phase relation within the beam. A light source, whose dimension is sufficiently small to be considered as point-like, satisfies this phase relation if the emission

profile is sufficiently smooth. The effort to obtain a suitable extended light source, e.g. a collimated beam with perfectly flat wavefronts, is at least as massive as constructing a point-like emitter. More information can be found in Subsection 4.3.4.

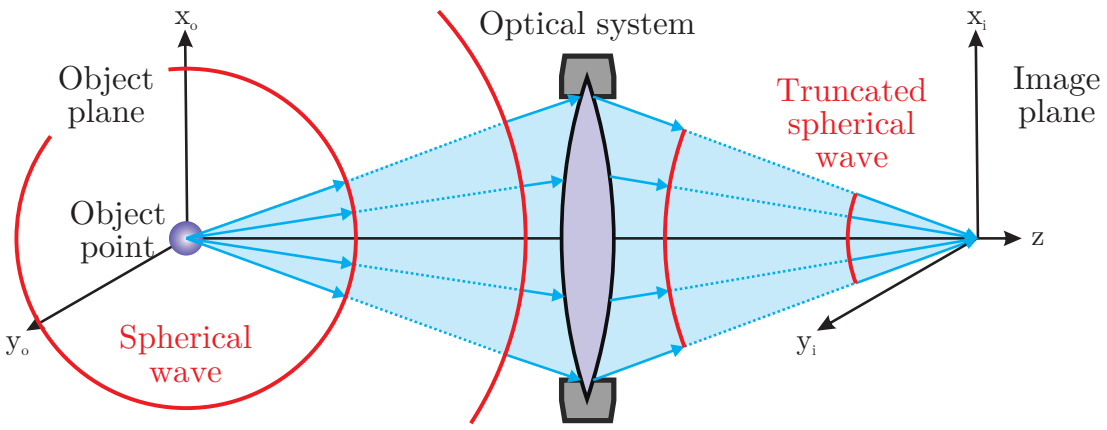

Figure 4.8: Diffraction effect, which leads to the generation of the PSF. Assuming an object point that emits spherical waves, the optical system truncates these waves due to the finite dimension of the aperture.

It is convenient to consider the ideal aberration-free point spread function of a rotationally symmetric optical system under homogenous illumination [85, 89]. The corresponding intensity distribution is shown in Figure 4.9. In the transverse sectioning, the intensity function of an ideal point image is Airy like:

$$I_{\mathrm{PSF}}^{(r)}(r_{\mathrm{i}}) = I_0 \left[\frac{2\, J_1(k \sin(\theta_{\mathrm{i}})\, r_{\mathrm{i}})}{k \sin(\theta_{\mathrm{i}})\, r_{\mathrm{i}}} \right]^2 , \tag{4.22}$$

with J_1 being the Bessel function of first order and θ_{i} the maximal angle of the light cone at the focal position (see Figure 4.9 (b)). The radial intensity distribution reveals an oscillatory behavior with not equidistant zeros. An important quantity is the diameter of the first ring of destructive interference, the Airy disk D_{Airy}:

$$D_{\mathrm{Airy}} \approx \frac{1.22\, \lambda}{\mathrm{NA}} . \tag{4.23}$$

Therefore, the numerical aperture of an optical system can be obtained by measuring the radial point spread function and especially the Airy disk diameter.
The intensity distribution of the PSF along the optical axis reveals an oscillatory behavior as well, but with equidistant intensity minima (see Figure 4.9 (a)):

$$I_{\mathrm{PSF}}^{(z)}(z_{\mathrm{i}}) = I_0 \left[\frac{\sin(\frac{\pi\, z_{\mathrm{i}}}{4\, z_{\mathrm{d}}})}{\frac{\pi\, z_{\mathrm{i}}}{4\, z_{\mathrm{d}}}} \right]^2 . \tag{4.24}$$

A characteristic quantity here is the diffraction limited depth of focus z_d. It describes the interval within the peak intensity reduces to 80 %:

$$z_\mathrm{d} \approx \frac{0.493\,\lambda}{\mathrm{NA}^2}\,. \tag{4.25}$$

Assuming the microscope objective with a NA of 0.5 and near infrared light ($\lambda = 780\,\mathrm{nm}$) as emitted by the $5^2\mathrm{P}_{3/2}$, F' = 0 $\rightarrow$ $5^2\mathrm{S}_{1/2}$, F = 1 transition, an Airy disk diameter $D_\mathrm{Airy} = 1.90\,\mu\mathrm{m}$ and a diffraction limited depth of focus $z_\mathrm{d} = 1.54\,\mu\mathrm{m}$ is obtained.

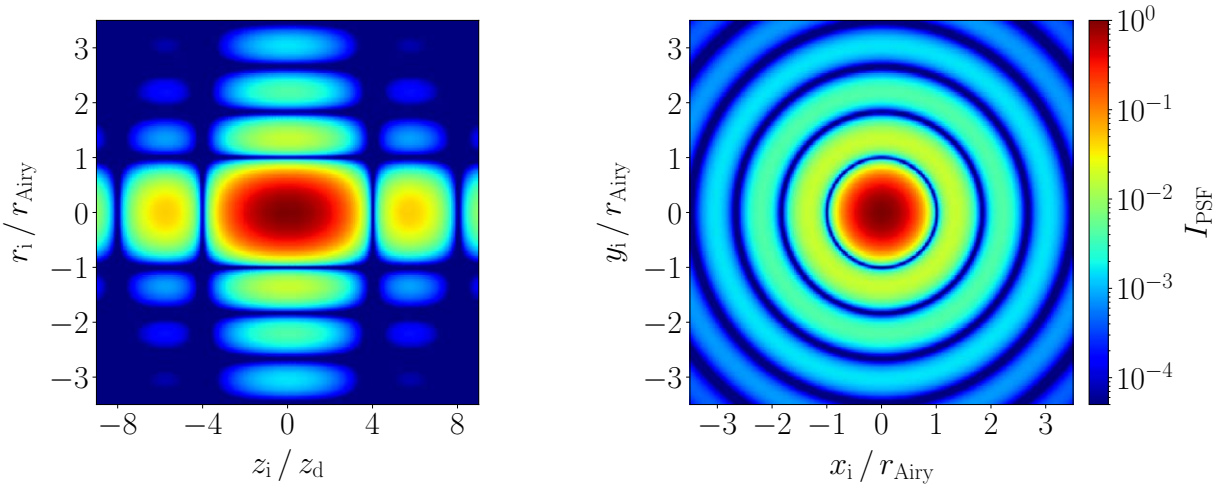

(a) PSF as a function of radial and longitudinal coordinates.

(b) PSF as a function of radial coordinates.

Figure 4.9: Schematic contour plots of a point spread function in the xz- and xy-plane. The PSF reveals an oscillatory behavior in all dimensions. In longitudinal direction it is equidistant and in transverse direction not equidistant. Characteristic quantities are given by the Airy disk radius r_Airy and the diffraction limited depth of focus z_d. The PSF is assumed to be normalized.

4.3.2 Point images of real systems

Point images of real systems can change drastically when the pupil is inhomogeneously illuminated or wave aberrations are taken into account [84, 85]. If the intensity profile illuminating the entrance pupil is enhanced towards the edge, both the transverse PSF and the Airy disk diameter shrink. In most instances the opposite effect occurs. The intensity distribution illuminating the pupil decreases towards the edges, which leads to an expansion of the transverse PSF. In the limit of a Gaussian intensity profile, an effect called apodization occurs [89]. It describes the absence of secondary intensity maxima, i.e., the lack of the ring structure (see Figure 4.10). Therefore, more energy is concentrated towards the center of the intensity profile. However, the larger width of the central curve leads to a decrease in angular resolution of the optical system.

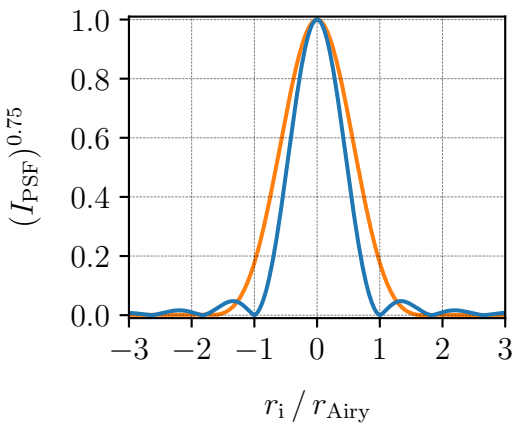

Figure 4.10: PSF with homogenous illumination (blue) and Gaussian apodization (orange).

Effects of inhomogeneous illumination can be caused by the light source, by the lens design itself or by local absorption effects e.g. caused by non uniform coatings [84]. In this thesis, the emission profile of the light source is measured by a camera. If the measured intensity profile can be well approximated by a mathematical function, this function is included in the mathematical description of the PSF. Even if the light source emits homogeneously, an inhomogeneous intensity profile at the exit pupil can be caused by the lens design itself. This effect especially occurs for high numerical aperture objectives [91–93]. While designing an optical system, it is possible to make the design insensitive against certain aberrations. If the lens system fulfills the sine condition for example, coma aberrations vanish as soon as the lens system is corrected for spherical aberrations [84, 85]. This is the case when the optical system reveals the same magnification for all aperture angles. In reality, the sine condition is never exactly fulfilled [85]. Besides that, there exist several similar conditions, for example the Herschel condition to suppress astigmatism or the Helmholtz condition to achieve a constant magnification over the field of view [93–95]. According to the Debye diffraction theory for high NA objectives, the relation between the intensity profile emerging from the exit pupil and incident intensity profile depends on the so-called apodization function $g(\theta)$ [93]. The exact relation is given by $g(\theta)\, g'(\theta)/\sin(\theta)$, where $g'(\theta)$ denotes the partial derivative with regard to θ. In the example of the sine condition, the apodization function is given by $g_{\mathrm{sine}}(\theta) = \sin(\theta)$, which leads to the following relation between the incident and exit amplitude: $\cos(\theta)$. This is exactly the projection factor described in Section 3.1. If an optical system satisfies sine condition, its principle planes are spherically shaped, leading to the same projection of Section 3.1. Zemax simulations of the Photon Gear objective indicate that sine condition is nearly fulfilled. However, the emission profile is measured by a camera which already projects the intensity profile onto a flat plane. Therefore, it is not necessary to consider an additional apodization factor.

Apart from the apodization effects, the PSF and especially the first Airy ring are very sensitive to wave aberrations. For coma aberrations, it is possible to identify aberrations well below the diffraction limited threshold ($c \approx \lambda/20$) only by observing the intensity structure by eye [84]. In general, increasing the amount of aberrations increases the deformation of the PSF, but the exact impact of wave aberrations depends on the type of the aberration itself. The individual effects are shown in Table 4.3 and Figure 4.11. In general, all higher (third, fifth, ..) order wave aberrations and defocus change the symmetry and the peak intensity drastically. While the change in symmetry depends on the symmetry of the type of aberration, the peak intensity decreases with increasing aberrations.

Aberration	Effect on point spread function
Piston	No effect at all
Tilt	Only changes the absolute position of PSF
Defocus & spherical	Induces ring structures and reduces central peak intensity
Astigmatism	Induces cross-like structures with x-y symmetry and reduces central peak intensity
Coma	Induces comet-like structures and reduces central peak intensity
Trefoil	Induces trefoil-like structures and reduces central peak intensity

Table 4.3: Effects of individual types of wavefront errors on the intensity profile of PSFs.

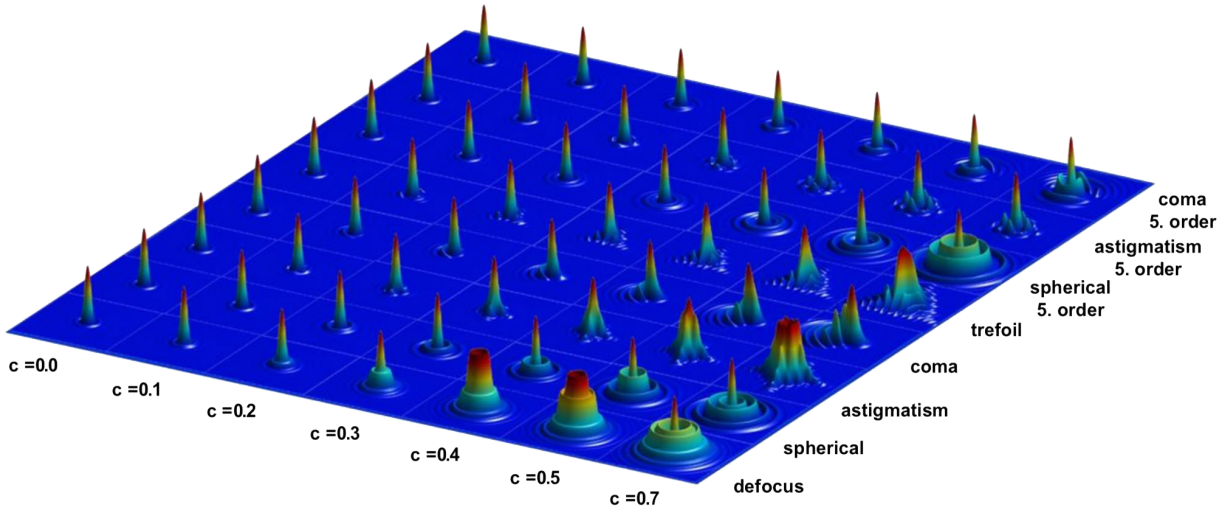

Figure 4.11: Effects of individual types of wavefront errors on the intensity profile of PSFs. The corresponding Zernike coefficients c are given in units of wavelengths. [84]

Since all aberrations represented by Zernike polynomials are orthogonal on the unit circle, they individually lead to a unique deformation. This provides the possibility to clearly extract the amount of the individual wave aberrations and therefore a sensitive analysis of system performance. Nevertheless, the differences of small distortions can often only be found within an intensity level of below 10 % of the peak value. Therefore, a computer based fitting algorithm is necessary to detect such small disturbances. Furthermore, it has to be noticed that an inhomogeneous illumination as mentioned above, has a huge impact on the effects of wavefront errors [84]. Illuminating the pupil inhomogeneously changes the

relative weight of different pupil regions and therefore the contribution of wave aberrations arising from these regions. For example, a Gaussian illumination suppresses the effects of wave aberrations which emerge from outer pupil regions.

Strehl ratio

The form of the intensity distribution within the Airy disk represents the basis of several quality criteria of PSFs [92]. It is possible to make statements of the energy density, the angular resolution and the amount of wave aberrations. Since all significant types of aberrations lead to a decrease of central intensity, the relation between unaberrated and aberrated peak value describes the total amount of aberrations within an optical system [84]:

$$\text{Strehl ratio:} \quad D_\mathrm{s} = \frac{I_\mathrm{PSF}^{(\mathrm{real})}(0)}{I_\mathrm{PSF}^{(\mathrm{unaberrated})}(0)} \,. \tag{4.26}$$

The Strehl ratio is defined for values between 0 and 1. It is equal to 1 for an unaberrated system and decreases with the amount of aberrations (see Figure 4.12). Since the Strehl ratio includes the effect of all involved wavefront errors in a single number, it is a simple criterion and critical in use at the same time. If the amount of aberrations is too large, the complex form induced by various aberrations can not be sufficiently represented by a single number anymore. Therefore, it only makes sense to use the Strehl ratio as quantity of system quality for $D_\mathrm{s} \gtrsim 0.6$ [84]. In general, Equation 4.26 is defined for both, systems with and without apodization effects. However, by assuming a homogenous illumination, analytical expressions can be derived [86]. For a nearly diffraction limited system, the wavefront term of $I_\mathrm{PSF}^{(\mathrm{real})}(0)$ can be expanded in a Taylor series, leading to the following simple approximation [84, 86]:

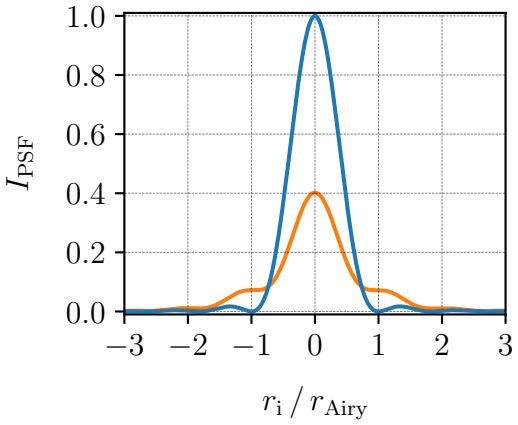

Figure 4.12: Normalized PSFs for an unaberrated (blue) and aberrated (orange) system. The Strehl ratio is given by the peak intensity: $D_\mathrm{s} = 1$ respectively $D_\mathrm{s} \approx 0.4$.

$$\text{Strehl ratio in Marechal approximation:} \quad D_\mathrm{s} \approx 1 - \left(\frac{2\pi}{\lambda}\right)^2 W_\mathrm{rms}^2 \,. \tag{4.27}$$

This approximation is justified[3], as long as $W_\mathrm{rms} \lesssim 0.1\,\lambda$ respectively $D_\mathrm{s} \gtrsim 0.6$. Using the

[3]For non diffraction limited systems, the following exponential approximation is recommended:

$$D_\mathrm{s} \approx e^{-(2\pi/\lambda)^2\, W_\mathrm{rms}^2} \,. \tag{4.28}$$

wavefront description of standard Zernike polynomials, a handy approximation is obtained:

$$D_\mathrm{s} \approx 1 - \left(\frac{2\pi}{\lambda}\right)^2 \sum_{\mathrm{n,m}} c_{\mathrm{nm}}^2 \,. \tag{4.29}$$

In the case of defocus, the Rayleigh respectively Marechal criterion of Subsection 4.1.1 reveals a Strehl ratio of $D_\mathrm{s} \approx 0.8$. Therefore, a system is denoted as diffraction limited if $D_\mathrm{s} > 0.8$. Table 4.4 depicts the Strehl ratios of the individual Zernike coefficients which correspond to the threshold of a diffraction limited system.

Aberration type	Coefficient	Marechal approximation	Exact Strehl
Defocus	$c_{20} = 0.072\,\lambda$	0.7944	$\frac{8}{\pi^2} = 0.8106$
Astigmatism	$c_{22} = c_{2-2} = 0.072\,\lambda$	0.7944	0.8133
Coma	$c_{31} = c_{3-1} = 0.072\,\lambda$	0.7944	0.8127
Spherical	$c_{40} = 0.072\,\lambda$	0.7944	0.8117
Trefoil	$c_{33} = c_{3-3} = 0.072\,\lambda$	0.7944	0.8155

Table 4.4: Zernike coefficients and Strehl ratios which correspond to the threshold of a diffraction limited system.

4.3.3 Fourier representation

Reformulate Equation 4.21 by using the far field approximation and defining $R = \sqrt{x^2 + y^2 + z^2}$ yields:

$$I_\mathrm{PSF}(x,y,z) = I_0 \left| \int_\mathrm{pupil} \mathrm{d}A_\mathrm{p}\, E_0(x_\mathrm{p}, y_\mathrm{p})\, e^{i\,\frac{2\pi}{\lambda}\,W(x_\mathrm{p},y_\mathrm{p})}\, e^{\frac{i\,k}{R}\,(x\,x_\mathrm{p} + y\,y_\mathrm{p}))} \right|^2 . \tag{4.30}$$

This integration can be treated in simplified form by using methods of Fourier optics. Therefore, the pupil coordinates are substituted by $x_\mathrm{p} = \nu_{\mathrm{x_p}}\,\lambda\,R$, $y_\mathrm{p} = \nu_{\mathrm{y_p}}\,\lambda\,R$, where $\nu_{\mathrm{x_p}}$ and $\nu_{\mathrm{y_p}}$ denotes the spatial frequencies of the exit pupil. Furthermore, it is useful to introduce the complex pupil function [85]:

$$P(\nu_{\mathrm{x_p}}, \nu_{\mathrm{y_p}}) = A(\nu_{\mathrm{x_p}}, \nu_{\mathrm{y_p}})\, e^{i\frac{2\pi}{\lambda}W(\nu_{\mathrm{x_p}},\nu_{\mathrm{y_p}})} \tag{4.31}$$

$$\text{with the aperture function: } A(\nu_{\mathrm{x_p}}, \nu_{\mathrm{y_p}}) = \begin{cases} 1, & \text{for } \nu_{\mathrm{x_p}}^2 + \nu_{\mathrm{y_p}}^2 \le \nu_\mathrm{NA}^2 \\ 0, & \text{for } \nu_{\mathrm{x_p}}^2 + \nu_{\mathrm{y_p}}^2 > \nu_\mathrm{NA}^2 \,. \end{cases} \tag{4.32}$$

The aperture function defines the dimension of the exit pupil of the optical system. In the spatial frequency representation, it is 1 if the radial spatial frequency does not exceed the spatial frequency of the numerical aperture[4] $\nu_\mathrm{NA} = \mathrm{NA}/\lambda$. Additionally the complex pupil

[4]The relation between ray angles θ_i, spatial frequencies, wavenumbers and spatial coordinates is given by [85]:

$$n \sin(\theta_\mathrm{i}) = \lambda\,\nu_\mathrm{i} = \frac{k_\mathrm{i}}{k} = n\,\frac{x_\mathrm{i}}{R} \,.$$

function contains the information of the change of phase introduced by the optical system, the wave aberration $W(\nu_{x_p}, \nu_{y_p})$. It can be expressed in terms of Zernike polynomials by using normalized spatial frequencies. Applying the above mentioned quantities, Equation 4.30 can be rewritten as:

$$I_{\mathrm{PSF}}(x,y,z) = I_0 \left| \int_{-\infty}^{\infty} \mathrm{d}\nu_{x_p} \int_{-\infty}^{\infty} \mathrm{d}\nu_{y_p}\, P(\nu_{x_p}, \nu_{y_p})\, E_0(\nu_{x_p}, \nu_{y_p})\, e^{i\,2\pi\,(x\,\nu_{x_p} + y\,\nu_{y_p}))} \right|^2 . \quad (4.33)$$

This expression exactly represents the 2D Fourier transform of the complex pupil function and the field strength $E_0(\nu_{x_p}, \nu_{y_p})$:

$$I_{\mathrm{PSF}}(x,y,z) = I_0 \left| \mathcal{F}[P(\nu_{x_p}, \nu_{y_p})\, E_0(\nu_{x_p}, \nu_{y_p})] \right|^2 . \quad (4.34)$$

Within this representation, the intensity distribution of the point spread function with arbitrary wave aberrations can be computed quickly by using convenient Fast Fourier transform algorithms. Note, that the wave aberrations of the optical system are contained in the complex pupil function and the apodization effects are contained in the field strength.

4.3.4 Generation of a point source

As mentioned in the previous section, the dimension of a light source must be sufficiently small and the emitted intensity profile must be sufficiently smooth to guarantee a constant phase relation. To obtain an equal contribution of wave aberrations arising from various different pupil regions, a preferably homogenous emission characteristic is desirable. However, it is mandatory that the emission profile can be represented by a convenient mathematical expression which can be implemented in the simulation algorithms. If the dimension of the light source is so small that it is not possible to resolve two separated points of this source, the light source is denoted as point source and the above mentioned requirements with regard to size are satisfied. There exist several criteria for the optical resolution depending on the numerical aperture of the objective. However, for a maximal NA of 0.5, all resolution criteria are satisfied well, if the spatial dimension of the light source does not exceed $\lambda/2$. Since the characterization of objective and self-made fiber collimator must be done for a wavelength of $\lambda = 780\,\mathrm{nm}$, the diameter of the light source should be below 390 nm. In the following, several possibilities to obtain such a point source are described.

SNOM fiber tip approach

A suitable point source is given by the aperture of an aluminum coated fiber tip. Originally it is employed for scanning near-field optical microscopy (SNOM) [96]. Therefore, these tapered fibers are commercially available with an aperture diameter ranging down to approximately 100 nm. In this thesis, several SNOM fiber probes with an aperture diameter of 185 nm[5] respectively 200 nm[6] are used. It is well known that SNOM fibers emit light

[5] TipsNano MF004.
[6] Lovalite E50-MONO780-AL-200.

onto a broad emission angle of ±164° [97, 98]. Obermüller et al. determined a homogenous angular intensity distribution for small angles up to ±10° and a $\cos(\theta)^2$ dependency for larger angles up to ±90°. For the H respectively V polarized fiber mode, two slightly different emission characteristics are obtained. This leads to an asymmetric PSF. However, if the exact emission characteristic is known, an optical system can be still characterized correctly. Moreover, the setup to characterize optical systems with SNOM fiber probes is quite simple [99, 100]. Mounting the fiber tip on a 5-axes stage (x, y, z translation and tip/tilt) provides all degrees of freedom needed for an optimal alignment.

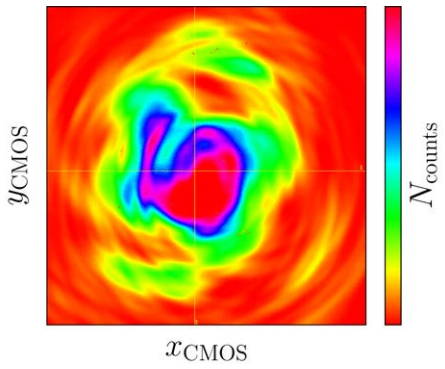

Figure 4.13: Measured intensity profile of a SNOM fiber probe.

However, in the analysis of the emission characteristic of 10 different commercial SNOM fiber probes of different producers, the results of Obermüller et al. can not be confirmed. All 10 fiber probes showed a similar emission profile as presented in Figure 4.13. The intensity distribution is irregular and changes completely when the polarization changes. Therefore, the wavefront deviates drastically from a spherical wave. This means that the usage of SNOM fibers in order to characterize optical systems is not possible.

Pinhole approach: manufactured with electron-beam lithography

Apart from SNOM fiber probes, illuminating a sub-half-wavelength pinhole operates as a high NA light source as well. In general, the transmission of light through a sub-wavelength aperture is a complicated process involving plasmonic effects [101]. Laser light excites surface plasmons on a dielectric-metal interface, which propagate through a pinhole and release energy in an unconstrained electro-magnetic mode. To describe this process, it is necessary to solve the Maxwell's equations. The emission characteristic of such a sub-wavelength aperture is nearly homogenous (see Figure 4.14) [102]. Since the pinhole must be illuminated using a focused beam, the experimental setup and the effort to align this setup expands significantly (see Section 4.4).

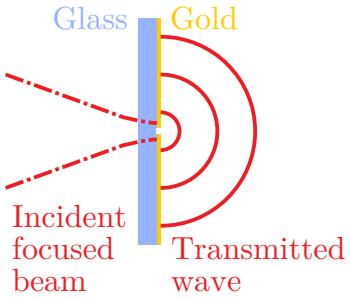

Figure 4.14: Transmission of light through a sub-wavelength aperture.

In this subsection, the plasmonic structures, e.g. the pinhole in nano scale, are produced by a method called electron-beam lithography. The functionality of this process is depicted in Figure 4.15. A glass substrate is coated with a resist (1), a common choice is polymethyl

methacrylate (PMMA). This resist layer is damaged under electron-beam exposure. By the use of electron microscopes, it is possible to write nanoscale structures with resolutions below 10 nm (2). The electron-beam breaks the long polymer chains of PMMA into smaller polymer chains which can be removed by using a suitable etching technique (3). Evaporating metal (4) and removing the resist leads to a patterning on the glass substrate according to the exposed areas (PMMA is a positive photoresist) (5). To produce pinholes, the whole PMMA layer must be exposed except of the region of the pinhole. Using a negative photoresist, the metal patterning happen on the unexposed areas. This generates pinholes only at exposed areas [103].

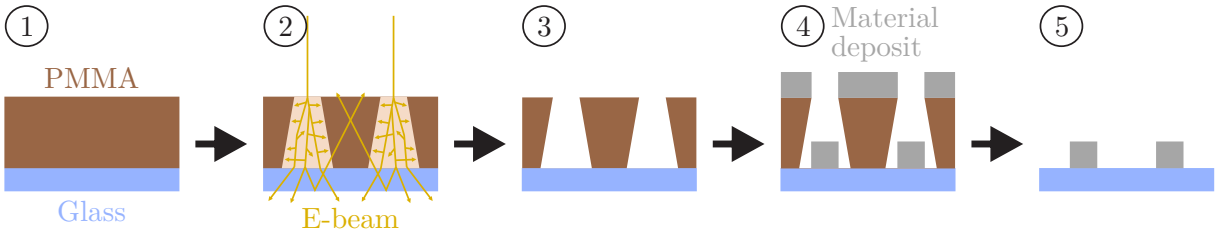

Figure 4.15: Stepwise generation of plasmonic nanostructures using electron-beam lithography with a positive photoresist.

Using this technique, Martin Zeitlmair produced sub-wavelength pinholes at the e-line of the LMU. The pinholes are placed in a gold layer since gold provides some advantages over other materials like aluminum or silver. Long propagation length of the surface plasmons leads to strong plasmonic effects. Furthermore, gold exhibits no disturbing resonances in the near infrared regime. However, it turned out, that several issues prevent a characterization of optics using pinholes generated by electron-beam lithography:

- Illuminate pinholes:
  For an illumination of the fabricated pinhole, its exact position is required. Finding a sub-wavelength pinhole is difficult, since it covers only a tiny area within the gold sample. Even by imaging the surface of the gold layer, the pinhole can not be resolved with visible light. Therefore, several markers are produced to identify the exact position of the pinhole. The setup to image the gold structure is described in Section 4.4.

- Finite dimension of the gold structure:
  To obtain pinholes with a suitable dimension, many pinholes were produced on one single glass substrate. Each pinhole is enclosed by a gold structure. Since the fabrication of pinholes using the positive resist PMMA is very time consuming (the whole area around the pinhole must be exposed), the dimension of these gold structures is limited to $\sim$ 120 µm x 120 µm. This leads to large gaps between the single gold structures. Due to internal reflections of the glass substrate (see Figure 4.14), light is leaking through these gaps. Since the intensity of the leaking light is in the same order of magnitude as the light emitted by the pinhole, a precise characterization

was not possible. Furthermore, the same effect occurred for markers identifying the position of the pinhole. It turned out that markers with a small size (1 µm x 5 µm) and a large distance to the pinhole (100 µm) suppress leaking light sufficiently.

- Thickness of the gold structure:
  Using a negative resist, it is possible to produce a sufficient large continuous gold layer with a thickness of 200 nm. According to Lambert-Beer's law, an attenuation of transmitted light due to the gold layer by a factor of 10^{-7} is assumed. This is sufficient to suppress the light which is transmitted evanescently through the gold. However, a much lower attenuation is measured such that the direct transmission through the gold layer is comparable with the transmission through the pinhole.

In the meantime, another approach using a focused ion beam led to satisfactory results.

Pinhole approach: manufactured with a focused ion beam

Metallic nanostructures can be fabricated directly by using a focused ion beam (FIB). Ions (normally Ga^+) are accelerated by high voltage electric fields and directly penetrate the metallic surface. Depending on the beam current and the accelerating potential a different amount of metal is milled. Using this technique, it is possible to produce nanostructures with a precision down to $\sim 5\,\text{nm}$ [103].
With the help of Martin Zeitlmair, a pinhole with a diameter of 362 nm inside a continuous gold layer with a thickness of 400 nm was produced at the WSI in Garching (see Figure 4.16 (a)). The attenuation by the gold layer is measured to be below 10^{-8}, which is sufficient to suppress direct transmission effects. Using small and widely separated identification markers, guarantees that light is only transmitted through the pinhole. The emission characteristic of the pinhole depicted in Figure 4.16 (b) is measured by a camera at a distance of $(7.1 \pm 0.1)\,\text{mm}$ from the pinhole. It exhibits a regular pattern, which can be well described by Gaussian intensity distribution with the width of $\sigma_\text{x} = (5.4154 \pm 0.0003)\,\text{mm}$ and $\sigma_\text{y} = (5.8273 \pm 0.0004)\,\text{mm}$. This point source enables a characterization of optical systems up to a numerical aperture of 0.64. Characterizing objectives with higher NA may lead to an underestimation of optical aberrations, since the illumination of the pupil becomes too inhomogeneous.

4.4 Characterization of the microscope objective

To measure the PSF, the point source is put in the focus of the optical system which is to be characterized. This results in a collimated beam which is focused by a lens onto a CMOS camera[7]. This way, the point source is imaged onto the camera and the PSF is obtained directly by measuring the intensity profile. Since the diameter of the Airy disk (1.9 µm) is smaller than one single pixel (5.5 µm), a lens with a long focal length ($f_\text{lens} = 2.5\,\text{m}$) is used to magnify the image by an factor of $f_\text{lens}/f_\text{objective} = 250$. Therefore,

[7] IDS UI-3370CP Rev. 2.

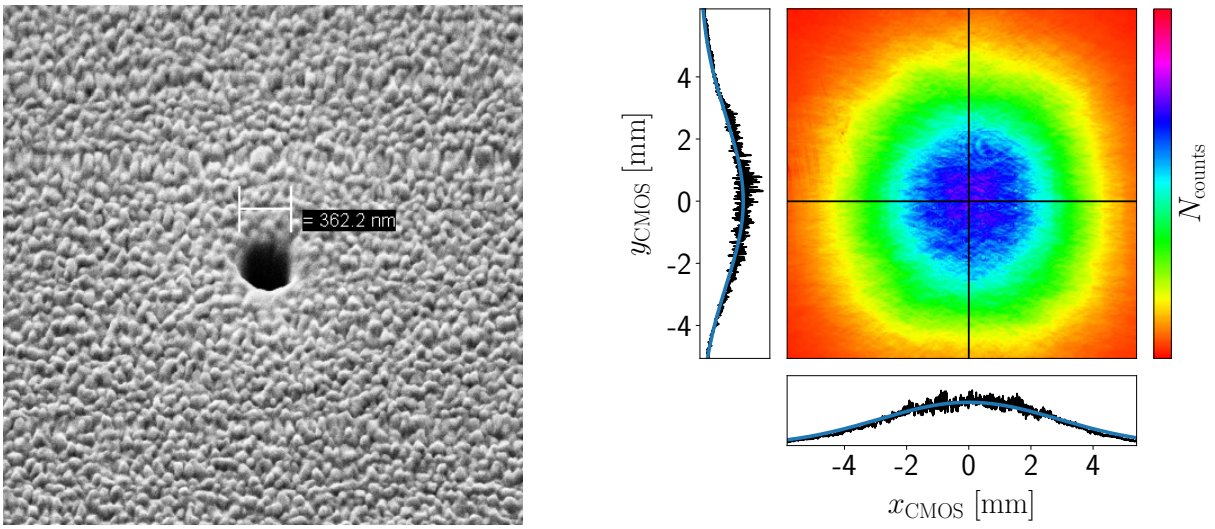

(a) SEM picture.

(b) Emission profile.

Figure 4.16: Scanning electron microscope picture and emission profile of the 362 nm pinhole produced by a FIB. In subfigure (b), the Gaussian Fit is depicted by a blue line.

the Airy disk illuminates roughly 86 pixels and effects of a finite pixel size of the camera are negligible [104]. Furthermore, the additional amount of wave aberrations induced by this lens is reduced to a minimum since the phase effect of a lens scales reciprocally with the focal length. The experimental setup is depicted in Figure 4.17. In the following, the alignment process is discussed:

First of all, the incident beam which illuminates the pinhole must be aligned. Therefore, the gold layer is shifted such that the objective operates in autocollimation configuration, i.e., the collimated incident beam is focused onto the gold layer and the reflected beam is collimated by the objective. By tilting the gold layer, an adequate overlap of incident and reflected beam is achieved. To find the position of the sub-wavelength pinhole, a camera with an eyepiece images the surface of the gold layer which is illuminated by the white light of a LED. The incident beam can be focused onto the pinhole by using the rotational and x, y translational degrees of freedom provided by the 6-axes stage of the gold sample. The same process is done to align the optical system which is to be characterized. But this time, the gold layer is fixed and the 3-axes translational and tip/tilt stage of the objective is used for alignment (for clarity, the necessary optical elements to image the gold sample seen from the objective side are neglected in Figure 4.17). Since the glass window of the vacuum chamber is included in the design of the objective, a glass plate simulating this window must be placed in front of the objective. This glass window is aligned with regard to the objective by observing the reflected interference patterns. More information of this alignment process can be found in Chapter 5 and [55]. In this process, the glass window must be mounted on a tip/tilt and longitudinal translation stage. To image the PSF onto a camera, a lens is mounted directly onto the objective.

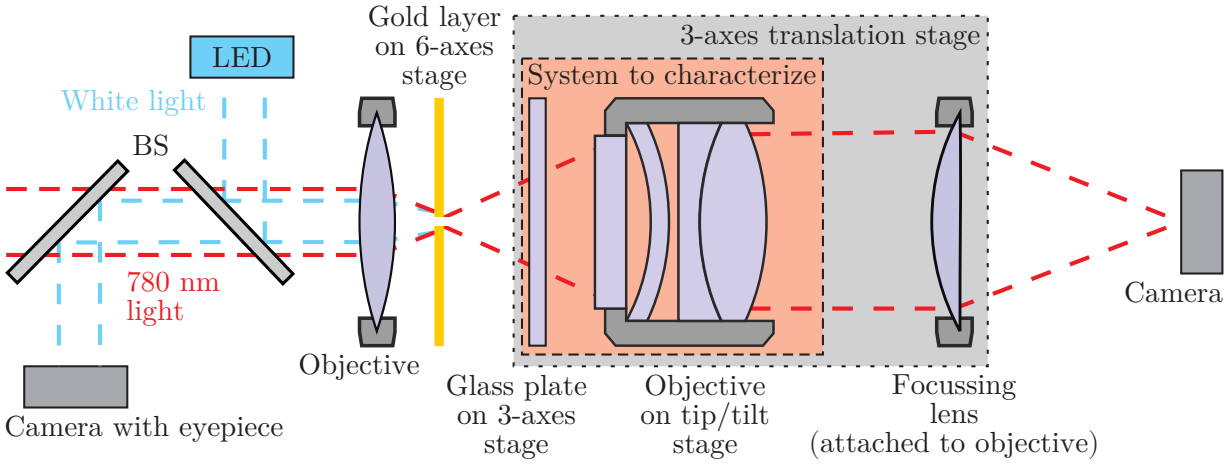

Figure 4.17: Experimental setup to characterize optical systems using the point spread function method. To image the surface of the gold layer, a camera with eyepiece, a LED and a BS are assembled in front of the objective which focuses an incident beam onto the pinhole. To perfectly align the pinhole with regard to the incident beam, the gold layer is mounted on a 6-axes stage. The optical system which is to be characterized, collimates the beam emerging from the point source. A focusing lens ($f_{\text{lens}} = 2.5\,\text{m}$) images the PSF onto a camera. For an optimal alignment, the glass plate is mounted on a 3-axes stage, the objective on a tip/tilt stage, the focusing lens is mounted on the objective and all three elements are mounted on a 3-axes translation stage.

Since the previously mentioned process only provides the possibility of a coarse alignment, the fine alignment is done by observing the intensity profile on the camera. Adjusting the translation and tip/tilt stages, the PSF is made as symmetric as possible (see Figure 4.18 (a)). In general, finding the optimal alignment is an iterative process which takes a lot of time and was aborted as soon as the results were satisfactory. It can not be excluded that there might be a better alignment. The intensity of the incident beam is tuned such that the exposure time of the camera is minimized and an overexposure of the central peak is prevented. This leads to a clear reduction of the signal-to-noise ratio. However, the remaining noise leads to a certain degree of randomness in the fit process. Therefore, a combination of a Gaussian and percentile filter[8] is used, without inducing a noticeable change in the intensity profile. The PSF is then reconstructed by using Equation 4.34 and a linear least squares minimization algorithm. The direct comparison between fitted and measured PSF can be found in Figure 4.18. In general, the intensity profile is well reproduced. Since the count-rate of the camera at areas of low intensity (e.g. 2nd or 3rd ring) is primarily determined by statistical processes, the measured PSF structure deviates from the perfect PSF in these regions. However, the intensity in these regions is so small that this does not significantly disturb the reconstruction process (see Figure 4.18 (c)).

[8]For each pixel, the p-percentile value is calculated and adopted within a given neighborhood for a given value p [105].

In the case of an ideal alignment, a numerical aperture of 0.5185 ± 0.0011 and a Strehl ratio of $0.9978\,^{+0.0022}_{-0.0075}$ is fitted[9]. The corresponding wave aberrations represented by the individual Zernike coefficients are shown in Table 4.5. In general, the absolute value of all coefficients is negligible and mainly determined by the remaining degree of randomness in the fitting process caused by statistics of the measurement process. The high Strehl ratio indicates a nearly perfect aberration free lens design which is far beyond the definition of a diffraction limited system. This agrees with the wavefront measurements of the producer. The numerical aperture is 3.8 % higher than originally assumed. Since no measurements or detailed data of the geometrical aperture are given by Photon Gear, it is not possible to retrace this deviation. It was demanded that the objective must fulfill a NA of 0.5, but it might be higher due to the consideration of manufacturing tolerances.

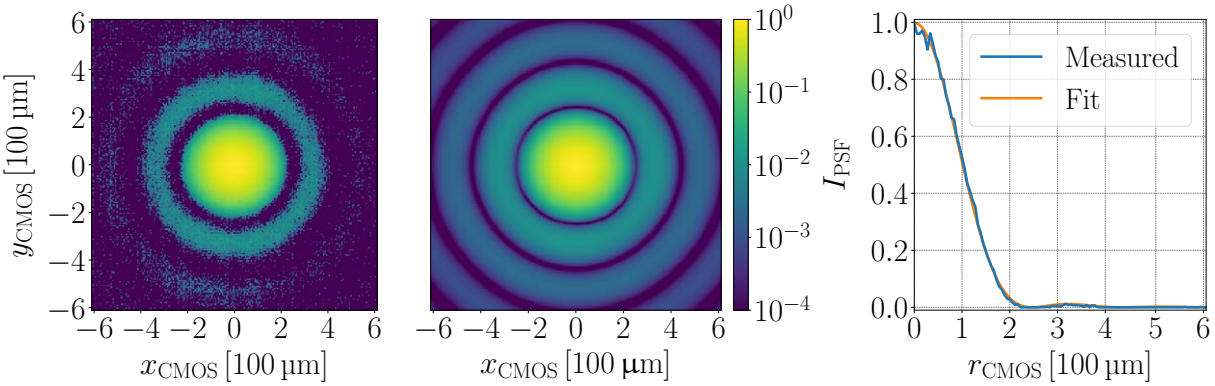

(a) Measured PSF. (b) Fitted PSF. (c) Comparison between measured and fitted PSF.

Figure 4.18: Measured PSF versus fitted PSF of the objective. Subfigure (a) and (b) show the transverse intensity profile of the measured and fitted PSF. To depict even small intensities, a log scale is chosen. The amount of noise of the measured PSF is low, but still needs to be considered. Deviations of the radial intensity distribution between the two PSFs are visible in subfigure (c). The difference is mainly caused by noise. The intensity of the 2nd ring is too small to be visualized in a normal scale. Deviations between measured and fitted PSF in regions with such low intensities do not have a crucial impact.

4.4.1 Imperfect alignment

As described previously, a negative impact on the optical performance caused by aberrations can not be expected if the microscope objective is perfectly aligned. In this subsection, the optical performance of the objective is analyzed if the alignment is not perfect.

[9] In general, the least squares algorithm underestimates the uncertainties of the fit. To obtain a better estimation of the errors, PSFs for known sets of parameters are simulated with noise and fitted afterwards. Comparing the input values to the fit results, the standard deviations of the NA and the aberrations can be calculated. The error of the Strehl ratio is obtained by propagation of uncertainty of Equation 4.28.

Aberration type	Zernike coefficients in λ	
Defocus	$c_{20} = -0.0054 \pm 0.0114$	
Astigmatism	$c_{22} = -0.0046 \pm 0.0118$,	$c_{2-2} = 0.0010 \pm 0.0110$
Coma	$c_{31} = 0.0004 \pm 0.0019$,	$c_{3-1} = 0.0005 \pm 0.0018$
Spherical	$c_{40} = -0.0044 \pm 0.0106$	
Trefoil	$c_{33} = 0.0009 \pm 0.0012$,	$c_{3-3} = 0.0002 \pm 0.0011$

Table 4.5: Results of the PSF fitting expressed in terms of Zernike polynomials.

Longitudinal displacement of the objective

In Figure 4.19 the Strehl ratio and the corresponding wave aberrations are depicted as a function of a longitudinal displacement of the objective from the optimal alignment position. A displacement of $\pm 0.5\,\mu m$ does not significantly change the optical performance. Up to a displacement of $\pm(1.75 \pm 0.13)\,\mu m$, the objective operates diffraction limited. If the objective is further displaced, the Strehl ratio and therefore the optical performance drops. As depicted in Figure 4.19 (b), the optical performance is mainly determined by the defocus aberration. Other types of wave aberrations do not change extensively and can be neglected in the process of longitudinal displacement.

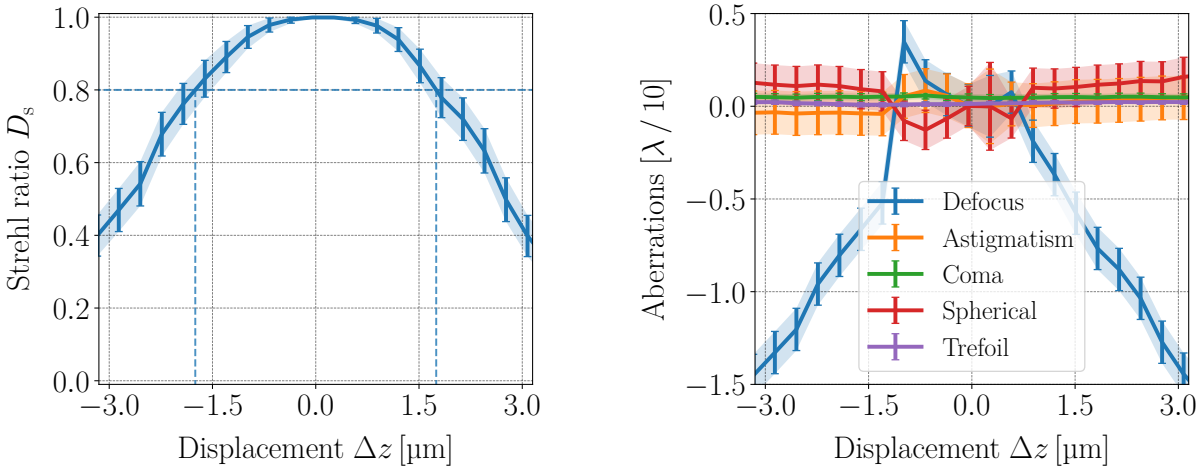

(a) Strehl ratio versus longitudinal displacement of the objective.

(b) Individual wave aberrations versus longitudinal displacement of the objective.

Figure 4.19: Optical performance of the objective under longitudinal displacement Δz. The objective operates diffraction limited up to a displacement of $\pm(1.75 \pm 0.13)\,\mu m$. The limiting wave aberration is given by the defocus.

Transverse displacement of the objective

The effect of a transverse displacement of the objective with regard to the point source is depicted in Figure 4.20. The Strehl ratio is shown as a function of longitudinal displacement for various transverse displacements. For zero longitudinal displacement, the Strehl ratio is not influenced by a transverse displacement up to 150 µm. In Figure 4.20, the Strehl ratio for a transverse displacement of 0.0 mm and 0.09 mm decreases if a negative longitudinal displacement is introduced and starts to increase again for a longitudinal displacement larger than −1.0 µm. The measurement of the curve for 0.0 mm transverse displacement and the curve of Figure 4.19 (a) are made subsequently and differ only in the measurement range of the longitudinal displacement. Therefore, it can be assumed, that the increase of Strehl ratio is a measurement artifact with no relevance to the optical performance. Most probably the reason for this is the hysteresis of the translation stages, since this effect only occurs at the beginning of the measurement interval. The measurements of the other curves of Figure 4.20 started well beyond a longitudinal displacement of −1.8 µm and therefore do not include the translation stage hysteresis artifact.

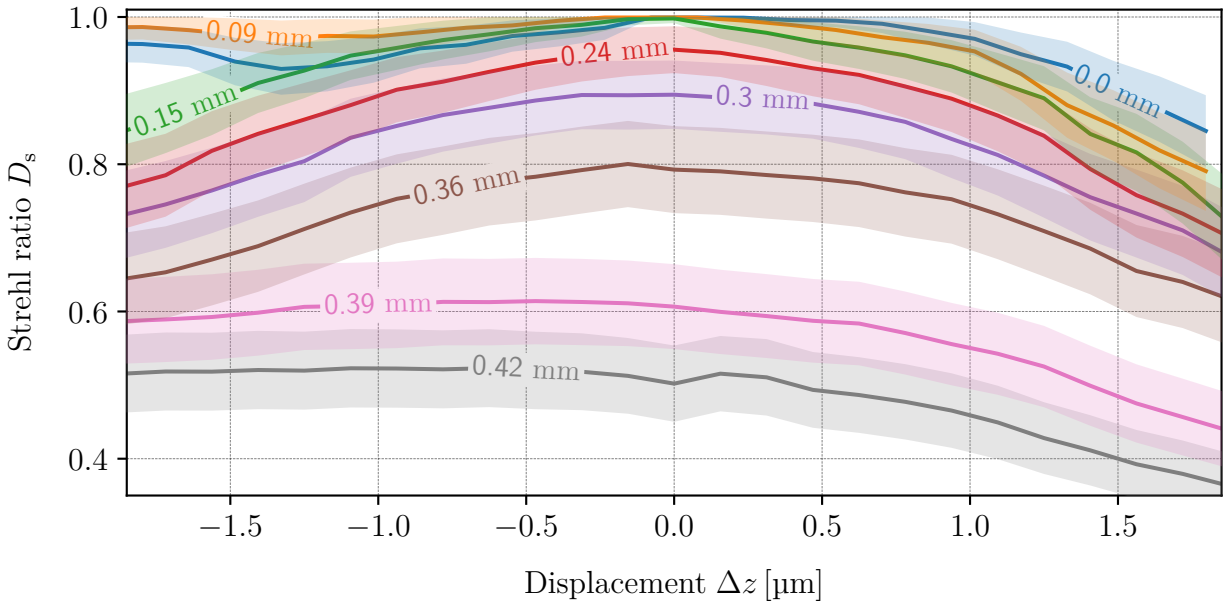

Figure 4.20: Strehl ratio as a function of longitudinal displacement for various transverse displacements of the objective.

Furthermore, a transverse shift of the objective leads to a change of beam path between focusing lens and camera (see Figure 4.17). To account for this effect, the beam emerging from the focusing lens is adjusted by mirrors such that the position of the camera can stay fixed. This process does not introduce further aberrations but may lead to a longitudinal displacement of the focus between different measurements with different transverse displacements (e.g. the curves of 0.0 mm and 0.09 mm in Figure 4.20 are shifted longitudinally against each other). The same effect of longitudinal displacements of the focal points

can turn up by a small angle between gold layer and the axis of the transverse translation stage. To separate this effect from the effect of transverse displacement, only Strehl ratios which correspond to the focal points are considered. The focus of each transverse displacement curve of Figure 4.20 is estimated by analyzing the wave aberrations and minimizing the defocus. This way, it is possible to describe the Strehl ratio as a function of transverse displacement of the objective, independent of the longitudinal displacement (see Figure 4.21 (a)). A transverse displacement of 150 µm does not influence the optical performance. Up to a displacement of (353 ± 15) µm, the objective operates diffraction limited. In this process, transverse shifts along the x-axis mainly introduce astigmatism 45° (see Figure 4.21 (b)) while shifts along the y-axis would introduce astigmatism 0°.

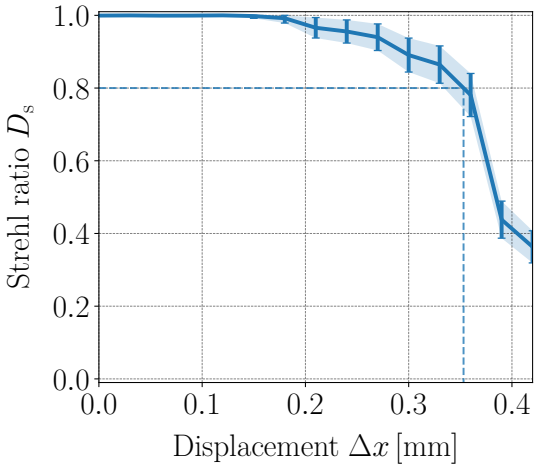

(a) Strehl ratio as a function of transverse displacement of the objective.

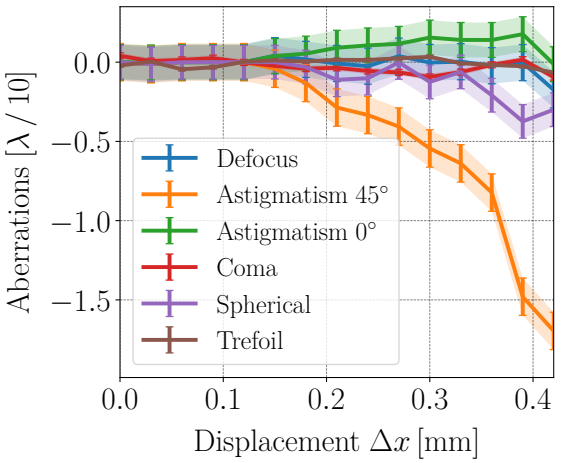

(b) Individual wave aberrations as a function of transverse displacement of the objective.

Figure 4.21: Optical performance of the objective under transverse displacements of the objective. The objective operates diffraction limited up to a transverse displacement of (353 ± 15) µm. Primarily astigmatism 45° is introduced.

Tilt of the glass plate

To complete the characterization of the objective, the effect of the glass plate tilt on the optical performance is shown in Figure 4.22. The increase of Strehl ratio beyond longitudinal displacements of −2.0 µm is caused by hysteresis of the translation stage. Considering the focal points of each curve of Figure 4.22, the Strehl ratio as a function of tilt angle ϕ of the glass plate is depicted in Figure 4.23 (a). The influence of a glass plate tilt is nearly linear to the tilt angle. The objective operates diffraction limited up to an angle of $(0.43 \pm 0.01)°$. As shown in Figure 4.23 (b), the limiting wave aberration is given by coma. Since the glass plate tilted vertically, primarily coma y is introduced. A horizontal tilt would induce coma x.

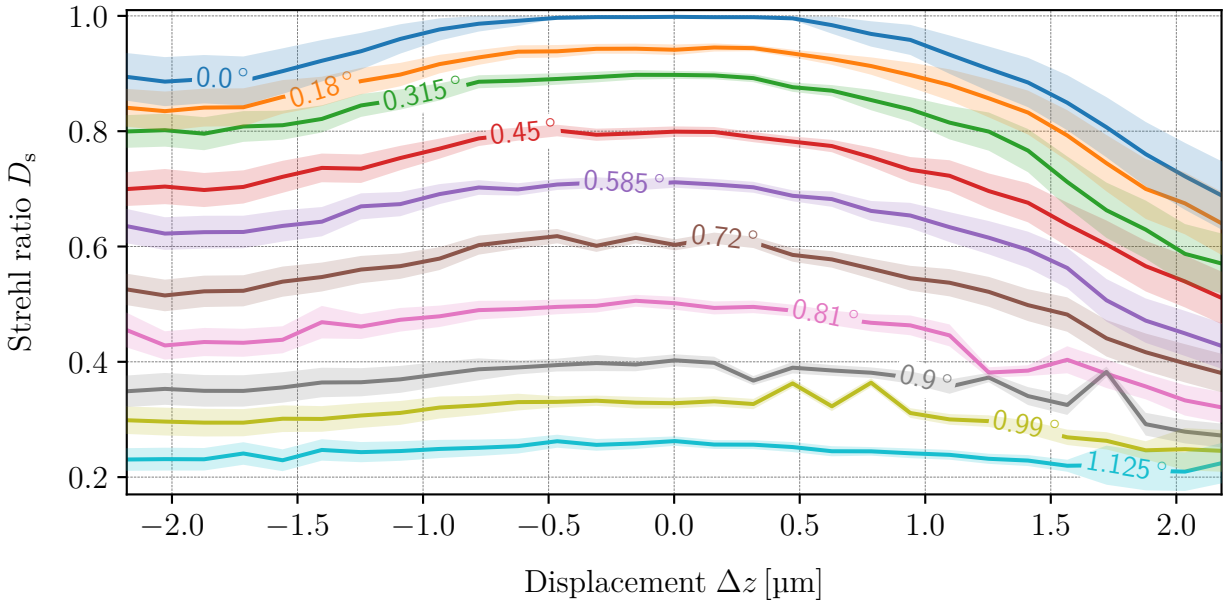

Figure 4.22: Strehl ratio as a function of longitudinal displacements of the objective for various tilt angles of the glass plate.

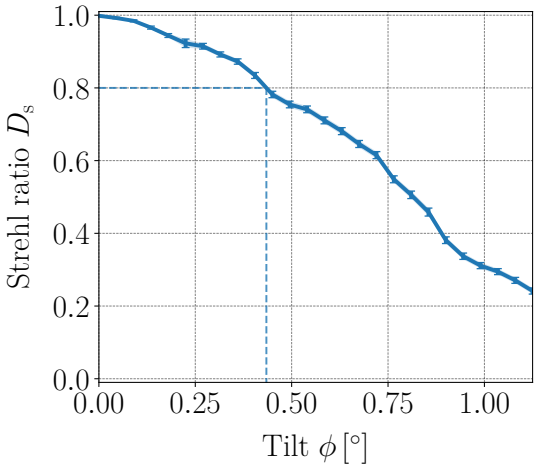

(a) Strehl ratio as a function of tilt angle of the glass plate.

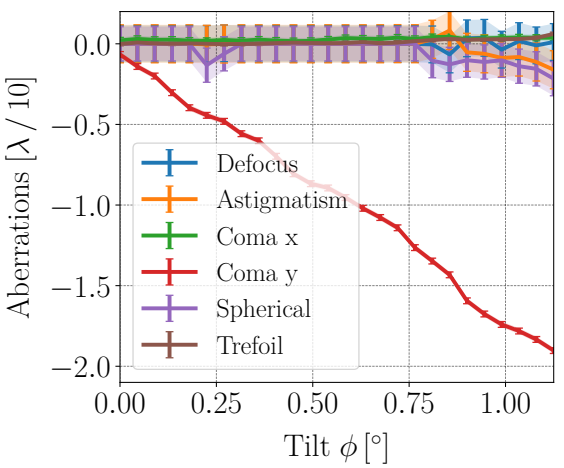

(b) Individual wave aberrations as a function of tilt angle of the glass plate.

Figure 4.23: Optical performance of the objective under tilt of the glass plate. The objective operates diffraction limited until a tilt angle of $(0.43 \pm 0.01)°$. Primarily coma y is introduced.

4.5 Characterization of the self-made fiber collimator

The self-made fiber collimator can be characterized with the same method as mentioned before. In contrast to the objective characterization, the glass plate and the objective is replaced by the fiber collimator.

In the case of the best achieved alignment, a numerical aperture of 0.1873 ± 0.0004 and a Strehl ratio of $0.9921\,^{+0.0079}_{-0.0100}$ is fitted. The measured PSF, the fitted PSF and the comparison between these two in normal scale is shown in Figure 4.24. The corresponding wave aberrations represented by the individual Zernike coefficients are shown in Table 4.6. The self-made fiber collimator is nearly aberration free and operates diffraction limited. The numerical aperture as well as the Strehl ratio agrees with the results of the Zemax simulation.

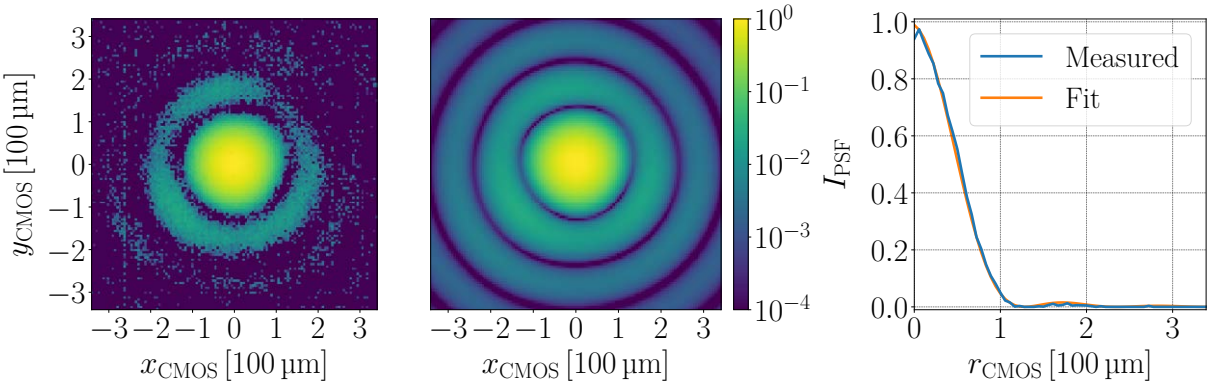

(a) Measured PSF. (b) Fitted PSF. (c) Comparison between measured and fitted PSF.

Figure 4.24: Measured PSF versus fitted PSF of the fiber collimator. Subfigure (a) and (b) show the transverse intensity profile of the measured and fitted PSF. To depict even small intensities, a log scale is chosen. The amount of noise of the measured PSF is low, but still needs to be considered. Deviations of the radial intensity distribution between the two PSFs are visible in subfigure (c). The difference is mainly caused by noise. The intensity of the 2nd ring is too small to be visualized in a normal scale. Deviations between measured and fitted PSF in regions with such low intensities do not have a crucial impact.

4.5.1 Imperfect alignment

In general, the fiber collimator is designed to be robust against any manufacturing tolerance. Therefore, it can be expected, that the optical performance is insensitive under misalignment.

Aberration type	Zernike coefficients in λ	
Defocus	$c_{20} = -0.0072 \pm 0.0109$	
Astigmatism	$c_{22} = -0.0062 \pm 0.0119$,	$c_{2-2} = -0.0044 \pm 0.0107$
Coma	$c_{31} = -0.0036 \pm 0.0016$,	$c_{3-1} = -0.0053 \pm 0.0017$
Spherical	$c_{40} = -0.0043 \pm 0.0104$	
Trefoil	$c_{33} = 0.0028 \pm 0.0012$,	$c_{3-3} = 0.0065 \pm 0.0011$

Table 4.6: Results of the PSF fitting expressed in terms of Zernike polynomials.

Longitudinal displacement of the fiber collimator

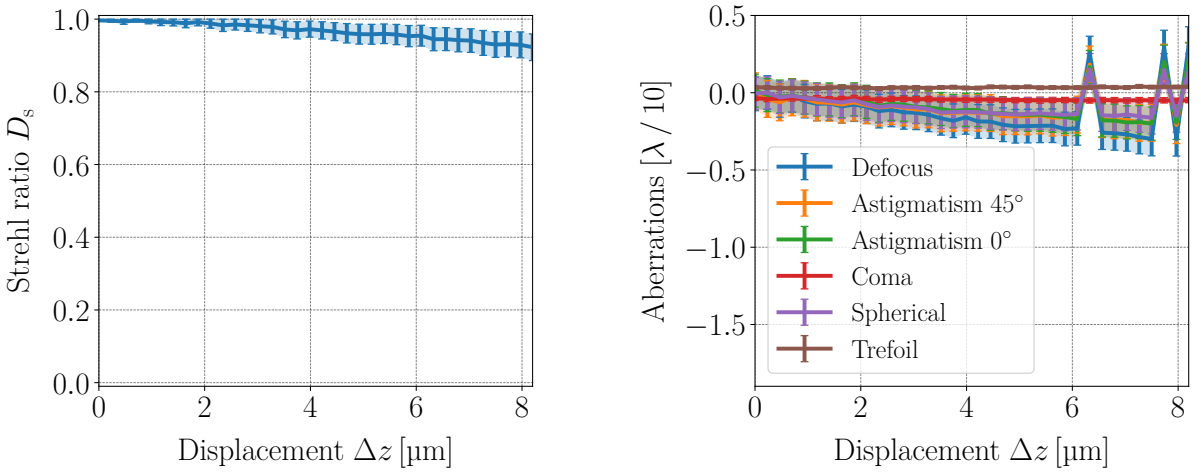

(a) Strehl ratio versus longitudinal displacement of the fiber collimator.

(b) Individual wave aberrations versus longitudinal displacement of the fiber collimator.

Figure 4.25: Optical performance of the fiber collimator under longitudinal displacement Δz. The optical performance of the fiber collimator is very insensitive under longitudinal displacement. Since the alignment is not perfect, defocus, spherical and both astigmatisms are introduced by the longitudinal shift.

The Strehl ratio as a function of the longitudinal displacement of the fiber collimator is shown in Figure 4.25 (a). At the moment when the measurements were performed, the fitting algorithm was not available yet. Therefore, it was not possible to analyze the data quantitatively, which leads to the fact that the measurement interval was chosen too small to identify the threshold of a diffraction limited operation. Moreover, it was necessary to implement the fiber collimator as soon as possible in the experiment (see Chapter 5) which made a remeasurement of the same optical system impossible. However, a displacement of 8.2 µm only leads to a reduction in Strehl ratio of 0.0775. Nevertheless, a remeasurement of

the lens design with larger measurement interval is desirable. Since the amount of defocus, spherical aberrations and astigmatism increases with the longitudinal displacement, it can be expected that the coupler is not perfectly aligned to the point source. The graph of Figure 4.25 (b) reveals an interesting 'symmetry', if the sign of the coefficients for defocus, spherical and both astigmatisms are inverted, the total PSF changes not significantly. Therefore, it is not possible for the fitting algorithm to distinguish between positive or negative sign, which leads to the depicted oscillations.

Transverse displacement of the fiber collimator

The Strehl ratio of the fiber collimator as a function of transverse displacement is shown in Figure 4.26 (a). The optical performance of the collimator is nearly unaffected up to a displacement of 0.4 mm. It operates diffraction limited within a transverse shift of (0.71 ± 0.08) mm from the ideal alignment. Similar to the objective, astigmatism 45° is primarily induced by the transverse displacement (see Figure 4.26 (b)).

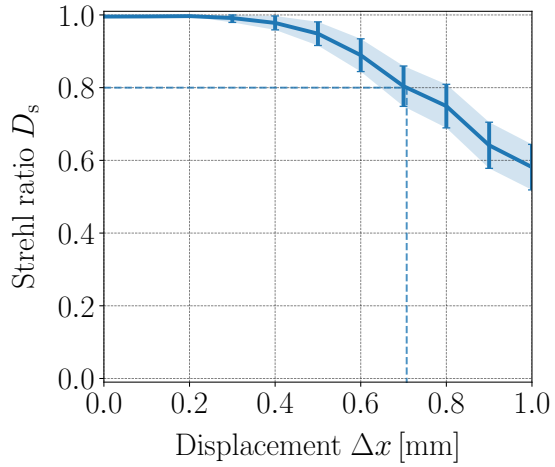

(a) Strehl ratio as a function of transverse displacement of the fiber collimator.

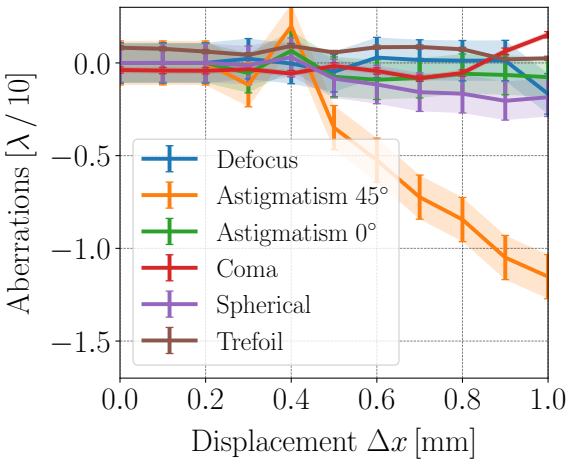

(b) Individual wave aberrations as a function of transverse displacement of the fiber collimator.

Figure 4.26: Optical performance of the fiber collimator under transverse displacements of the objective. The fiber collimator operates diffraction limited up to a transverse displacement of (0.71 ± 0.08) mm. Primarily astigmatism 45° is introduced.

Tilt of the fiber collimator

Tilting the fiber collimator with respect to the point source does not significantly influence the optical performance. As shown in Figure 4.27, the Strehl ratio and the individual wave aberrations are nearly constant within a change of rotation angle up to 1.2°. It was not possible to further tilt the collimator, since the stage was maximally tilted. It can be expected that this robustness against rotation is caused by the assumption of the large manufacturing tolerances (see Section 3.4). However, this should be subject of further investigation.

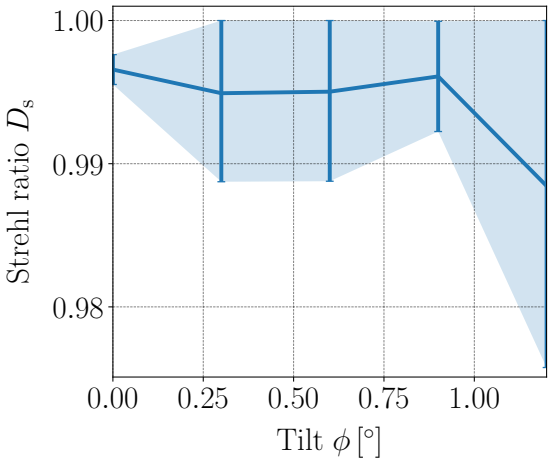

(a) Strehl ratio as a function of tilt angle of the fiber collimator.

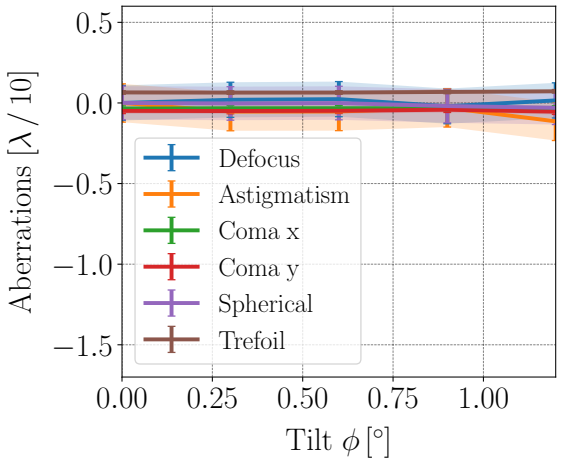

(b) Individual wave aberrations as a function of tilt angle of the fiber collimator.

Figure 4.27: Optical performance of the fiber collimator under tilt. Within the measurement interval, the optical performance is nearly unchanged.

Chapter 5

New high NA microscope optical setup

As mentioned in the previous chapters, for future quantum communication applications, it is crucial to increase the atom-atom entanglement rate. To achieve this, a new optical setup containing the custom designed microscope objective and the self-made fiber collimator, is implemented in the second laboratory. In the following chapter, all optical elements of this setup are described. Since the optical performance depends significantly on the alignment of the glass cell as well as of the relative displacement of atom and objective (see Chapter 3 and 4), several alignment techniques are presented, guaranteeing a diffraction limited operation and maximizing the collection and coupling efficiency. Finally the increase in collection and coupling efficiency and therefore in entanglement rate is presented.

5.1 Optical setup

In general, the optical setup (see Figure 5.1) combines the functionality of the 780 nm fluorescence collection, the trapping of atoms by an 857 nm ODT[1] and the read-out process using a 473 nm ionization laser. The three wavelengths are superimposed by two dichroic mirrors and focused respectively collimated by the microscope objective. This objective is custom-made by Photon Gear, satisfying all requirements needed for this experiment. It is specified to provide a NA of at least 0.5 for 780 nm, although the characterization leads to an even higher NA of 0.5185 (see Section 4.4). Furthermore, it is required to operate diffraction limited for all three wavelengths and have a transmission higher than 90 %. In the lens design, the window of the vacuum chamber is already included, leading to a working distance[2] of 14 mm. One of the dichroic mirrors is 2 ” in diameter and coated such that it features a high reflectivity for 857 nm light while transmitting 473 nm and 780 nm light. The other dichroic mirror is 1 ” in diameter, fixed on a precision mirror

[1]The wavelength of the ODT is different for the two laboratories. In laboratory 1, the wavelength is 850 nm and in the second laboratory the ODT operates at 857 nm.

[2]Distance between focal point and objective.

mount and is highly reflective for 780 nm light and transmissive for 473 nm. The fidelity of the atom-photon entanglement strongly depends on the indistinguishability of H and V photons. Therefore, the transmission and reflection of 780 nm light must be independent of its polarization. It is measured that the transmission respectively the reflection is equal for different polarizations up to 99.9 % [55]. Furthermore, the absolute polarization of the ODT is maintained very well in the reflection process. This is crucial for the atomic state evolution (see Subsection 2.5.1), since circular polarized light introduces a state dependent Zeeman splitting of the atomic energy levels which leads to decoherence. More information about the polarization dependent analysis of the dichroic mirrors can be found in [55]. The new optical setup is assembled in a modular form. All optical elements are mounted on a single nonmagnetic breadboard. If the complete setup is pre-aligned, a simple integration in the single atom trap experiment is possible by aligning only the complete breadboard with regard to the vacuum glass cell (see Subsection 5.2.4). Whenever possible, optomechanical components constructed of nonmagnetic stainless steel are used to minimize the state dependent influence of magnetic fields (Subsection 2.5.1) and guarantee low hysteresis of the extension of stainless steal even if the temperature fluctuates moderately. For the adjustment of the objective the focal points of the three wavelengths must be overlapped. In this process, it is necessary to invert the order of optical elements involved in the fluorescence collection process. The 780 nm light coming from the fiber is collimated by the self-made fiber collimator and guided to the objective. Thus, the focal point corresponds to the optimal position for collecting light from the atom. Using 473 nm and 857 nm light from diode lasers, the beam paths of these two wavelengths can be aligned with regard to the 780 nm focal point. Figure 5.1 depicts the optical setup in the alignment process. A glass plate simulates the effect of the window of the vacuum chamber. In the following, the three different beam paths are described in detail.

Fluorescence beam path

First of all, the 780 nm light is collimated by the self-made fiber collimator. The alignment of the fiber with regard to the collimator is done by using the technique of optical beam propagation. The best results are obtained by adjusting a full set of degrees of freedom (DOFs) (the five DOFs from the collimator mount, see Section 3.4) such that the deformation of the intensity profile is minimized (see Section 4.2). To reduce losses, an anti-reflective coated fiber end is used. The four DOFs of the mirror and the dichroic mirror provides the possibility to align the beam with respect to the optical axis of the microscope objective (see Subsection 5.2.1). To suppress polarization dependent effects during the reflection process, a silver mirror is used [41]. The dimension of the 1 ” optics is precisely sufficient such that the collimated beam with a waist of 4.1 mm is not truncated. The focal point of this beam indicates the position of the highest collection and coupling efficiency. Since the ODT beam defines the position of the atom, the focal points of the ODT and ionization beam must be aligned with regard to the 780 nm focal point.

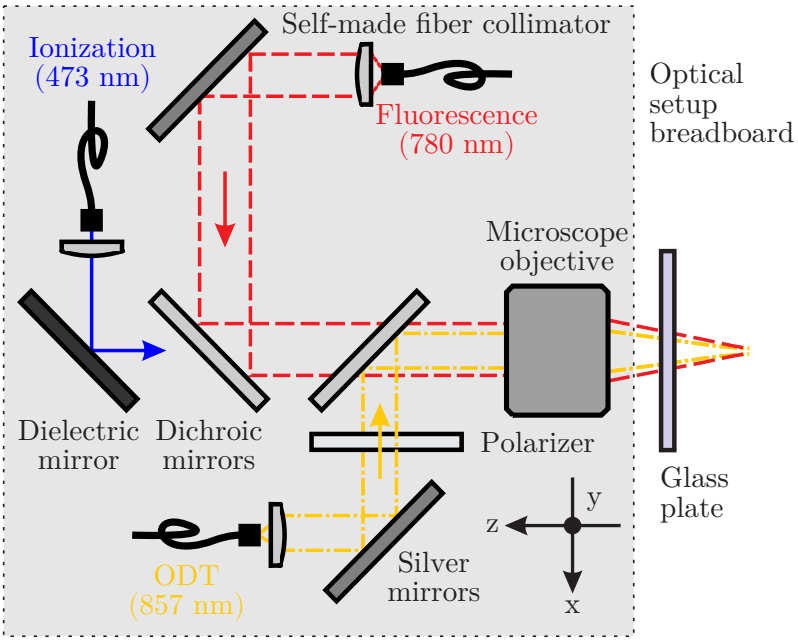

Figure 5.1: The optical setup mounted on a single breadboard. Dichroic mirrors superimpose the three different wavelengths 473 nm, 780 nm and 857 nm. The microscope objective is designed for all three wavelengths and focuses the beams. To overlap the three focal points, the fiber collimators of the ionization and ODT beams, as well as all mirrors except of the dichroic mirror, which reflects the ODT laser, are mounted on mirror mounts. To increase the collection and coupling efficiency the self-made fiber collimator is used for the 780 nm light. To enhance the atomic state coherence, a polarizer is placed in the ODT beam path. A glass plate simulates the effect of the window of the vacuum chamber.

ODT beam path

An achromat fiber collimator[3] with a focal length of 15 mm is used to collimate the ODT beam at a waist of 1.15 mm. Since the polarization is crucial for the atomic state evolution (see Subsection 2.5.1), a polarizer is placed into the beam path to transmit only H polarized light with a measured extinction ratio of 1/130000 [55]. In general, the polarization is much more affected by transmission processes than by reflection processes. Therefore, the beam path is chosen such that only reflection occurs, i.e., that this beam couples into the path towards the microscope objective last. Since the position of the atom is defined by the focal point of this beam path, it is essential for the collection and coupling efficiency (see Chapter 3) that the position of the atom and the focus of the 780 nm light coincide. Therefore, the five DOFs (the mirror mount of the silver mirror, the mirror mount of the collimator and the distance between collimator and fiber) are chosen such that the focused beam overlaps with the reference beam in position and angle

[3]Schäfter Kirchhoff 60FC-4-M15-37.

(see Section 5.2). Since the collimator is not characterized due to lack of time, the collimator potentially introduces optical aberration which would disturb the trapping process respectively the atomic state evolution inside the ODT. It is recommended to replace this fiber collimator with a self-made fiber collimator adapting the needs of this experiment. Within the framework of this thesis, a suitable lens design was created (see Appendix D) but due to the limited time it was not possible to accomplish this intention. Furthermore, it is crucial for the atomic state evolution, that the intensity of the ODT is as stable as possible. For this reason, the light which is transmitted through the dichroic mirror ($T \sim 10^{-4}$) is focused onto a fast amplified photodiode. This photodiode is linked to a feedback loop, which stabilizes the intensity.

Ionization beam path

For the ionization beam, a monochromatic collimator[4] with a focal length of 12 mm is used to collimate the ionization laser to a waist of 1.14 mm. Together with the two DOFs of the mirror and the three DOFs of the collimator, it is possible to overlap the ionization beam with the two former ones. Since the ionization process only depends on the local intensity of the ionization laser at the position of the atom, it is not necessary to take action against polarization fluctuation effects or wave aberrations. However, wave aberrations induce deformations in the intensity profile of the beam, which makes it more difficult to overlap with the other two beams.

5.2 Alignment of the optical setup

To obtain the necessary entanglement rates for long distance applications, the optical setup must satisfy several alignment requirements. Most importantly, the three incident beams and the glass cell must be aligned with regard to the optical axis of the microscope objective. Furthermore, the focal points of the three beams must overlap in position and beam angle.

5.2.1 Incident beam alignment

If the incident beam and the optical axis of the objective differ by a small angle α, the focal point is transversely displaced by $\Delta x = \tan(\alpha)\, f$, where f denotes the focal length. According to this simple approximation, the angle between incoming beam and optical axis must be smaller than 2.02°, to guarantee a diffraction limited operation of the objective (see Section 4.4). This alignment requirement can be easily obtained by using a simple technique shown in Figure 5.2 (a). An iris and a combination of an iris and a mirror are directly mounted on the fiber collimator and respectively the microscope objective. Due to the iris, the beam emerging from the fiber collimator is on-axis. This beam is adjusted by two mirrors such that it passes the iris of the objective and gets reflected by the mirror. If

[4] Schäfter Kirchhoff 60FC-4-M12-33.

the reflected beam passes the iris of the fiber collimator, the incident and reflected beam are overlapped in angle and position. This automatically leads to the alignment with respect to the optical axis of the objective, if the mirror is mounted perpendicularly to the objective. It must be noted that there is always a small misalignment of the mirror due to oblique planes or threads. However, it can be estimated, that the angle between incident beam and optical axis of the objective is smaller than $\lesssim 0.1°$.

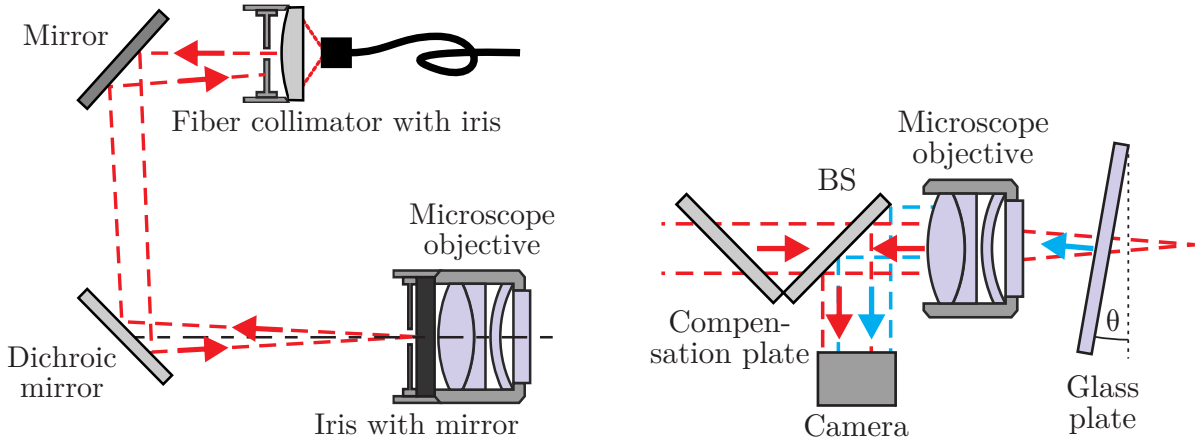

(a) Scheme for aligning the incident beam with respect to the optical axis of the objective.

(b) Scheme for the alignment of the glass plate.

Figure 5.2: Alignment techniques for the incident beam and the glass cell. The incident beam is overlapped with a reflected beam by mounting an iris and an iris with a mirror onto the fiber collimator and respectively the objective. Therefore, the incident beam can be aligned with respect to the optical axis of the objective, if the mirror is perpendicular to the objective. To align the glass plate, a beam splitter images the reflected light of the objective and the glass plate onto a camera. If the glass plate is sufficiently pre-aligned, an interference pattern appears, which can be used for alignment.

5.2.2 Glass cell alignment

As described in Section 4.4, a misalignment of the glass cell leads to coma. Therefore, the angle between glass cell and objective must be smaller than 0.43° to guarantee a diffraction limited operation. Observing the interference pattern of the back reflected light from the objective and the glass cell (see Figure 5.2 (b)), it is possible to align the glass cell up to a precision of $\sim 0.02°$. In this process, the glass plate is mounted on a longitudinal translation and a tip/tilt stage. At the beginning, it is necessary to pre-align the angle of the glass plate such that an interference pattern appears. This is done by using a 50 µm thick lens cleaning tissue. The glass plate is moved directly in front of the objective and the angle is adjusted in a way that the overall distance between objective and glass plate is equal and corresponds

to the thickness of the cleaning tissue. Afterwards the glass plate is moved 3 mm away from the objective, which is specified by the lens design. Placing a beam splitter with a compensation plate into the beam path, makes it possible to image the back reflected light with a camera without affecting the alignment of the incident beam. If the incoming beam is pre-aligned according to Subsection 5.2.1, concentric rings appear due to the interference fringes of the lenses of the objective. Furthermore, a substructure is visible, which indicates the interference between glass plate and objective. The better the glass plate is aligned, the larger is this structure. Since the objective and the glass plate are both anti-reflective coated, the interference pattern is easily overexposed by scattering light. Therefore, it is necessary to sufficiently isolate the transmitted beam. In practice, it is reasonable to use the ODT beam for alignment because the structure of the interference fringes scales with the wavelength. A detailed description containing figures of the interference patterns is given in [55].

5.2.3 Overlap of the foci

Since the focus of the ODT determines the position of the atom and the focus of the 780 nm light defines the spot of highest collection and coupling efficiency (see Chapter 3), it is essential for the atom-atom entanglement rate that these two points overlap. Furthermore, the ionization laser must be overlapped as well to ensure an efficient read-out scheme. For the following alignment process, it is necessary that the 780 nm beam (the reference beam) as well as the glass cell are pre-aligned according to the previously mentioned methods. A coarse alignment of all three beams can be achieved by overlapping the intensity profiles at a short ($\sim$ 30 cm) and long ($\sim$ 9 m) distance. In this process, it is necessary that all beams are nearly collimated and the 780 nm beam, as a reference, is not adjusted at all. Since all three beams coincide in two different positions, they should overlap in position and angle. However, an imperfect alignment of the reference beam with respect to the optical axis might lead to a different focal point due to chromatic effects. Moreover, the lens design determines that a common focal point is only achieved, if the fluorescence beam is collimated, the ODT beam is convergent and the ionization beam is slightly divergent. Anyway, it is necessary to measure the overlap at the position of the focus. Since the beam waist at the foci is less than 1 µm, it is not possible to resolve the intensity profile with a camera. However, this is possible by performing a knife-edge measurement.

Knife-edge method

The knife-edge measurement is a standard technique which allows a fast and accurate determination of beam parameters such as focal position and waist [106]. A sharp edge truncates the beam completely in one dimension and is moveable in the orthogonal dimension. Measuring the power of the clipped beam while changing the position of the sharp edge, it is possible to reconstruct the beam parameters. In this thesis, a photodiode which is partially coated with sharp gold structures, truncates the beam and measures the power at the same time [107]. Assuming a Gaussian beam, the total incident power depends on

the position x_e and z of the edge and is given by:

$$P(x_\mathrm{e}, z) = \int_{-\infty}^{\infty} \mathrm{d}y \int_{-\infty}^{x_\mathrm{e}} \mathrm{d}x \, I_\mathrm{Gauss}(x, y, z) = P_0 + P_\mathrm{l} \, \mathrm{erf}\left(\frac{\sqrt{2}(x_\mathrm{e} - x_0)}{w(z)}\right), \tag{5.1}$$

where P_0 is the background power, P_l the laser power, x_0 the transverse focal position and $w(z)$ the waist of the Gaussian beam at longitudinal position z. Measuring $P(x_\mathrm{e}, z)$ for various values of x_e, the four variables (P_0, P_l, x_0, $w(z)$) can be determined by a least squares fit. Using the same technique and measuring along the y-axis, the vertical focal position y_0 can be obtained. If this procedure is repeated for several different longitudinal positions z of the edge, the longitudinal focus z_0 and focal beam waist w_0 are obtained by fitting the following function to this dataset:

$$w(z) = w_0 \sqrt{1 + \left(\frac{M^2 \, (z - z_0)}{z_\mathrm{R}}\right)^2}. \tag{5.2}$$

The beam quality M^2 quantifies the deviation of the measured beam with regard to a perfect Gaussian beam ($M^2 = 1$). A 3D translation stage with a step size of 20 nm enables the precise measurement of beams with waists of several hundred nanometers.

This knife-edge measurement is applied to each of the three beams separately. By changing the distance between fiber and fiber collimator (longitudinal adjustment) or tilting the mirror mounts (transverse adjustment), the overlap of the three beams can be iteratively improved. The results of the final M^2 measurements (fitting Equation 5.2) are shown in Figure 5.3 and 5.4. Since it was not possible to provide a laser source with a wavelength of 473 nm shortly, a wavelength of 450 nm is used. Zemax simulations showed that the focal position changes by −13 µm if the wavelength is changed from 450 nm to 473 nm. That is the reason for the longitudinal offset of (12.95 ± 0.35) µm between the ionization beam and 780 nm beam. In z-direction, the focal points of the ODT and fluorescence beam overlap up to a precision of $^{+0.3}_{-1.5}$ µm in vertical respectively horizontal position. Note, that the exact difference of the focal points strongly fluctuates (~ 1 µm) from measurement to measurement without changing the setup. Reasons for this behavior might be temperature fluctuations or imprecisions of the translation stage. Furthermore, the fit strongly depends on the chosen measurement interval. Nevertheless, the large longitudinal separation of 1.8 µm between the horizontal and vertical focal point of the ODT indicates astigmatism. The transverse overlap of the three beams is given by ±250 nm. After the new optical setup is integrated in the main experiment, it is anyhow necessary that the ODT and ionization beam are adjusted to optimize the collection and coupling respectively the ionization efficiency (see Subsection 5.2.4). Therefore, it is only necessary that the alignment is sufficient to obtain a signal (trap atoms and collect fluorescence light) which can be optimized. However, it is possible to overlap the three beams longitudinally with a precision of 0.3 µm and transversely with a precision of 50 nm as described in [55].

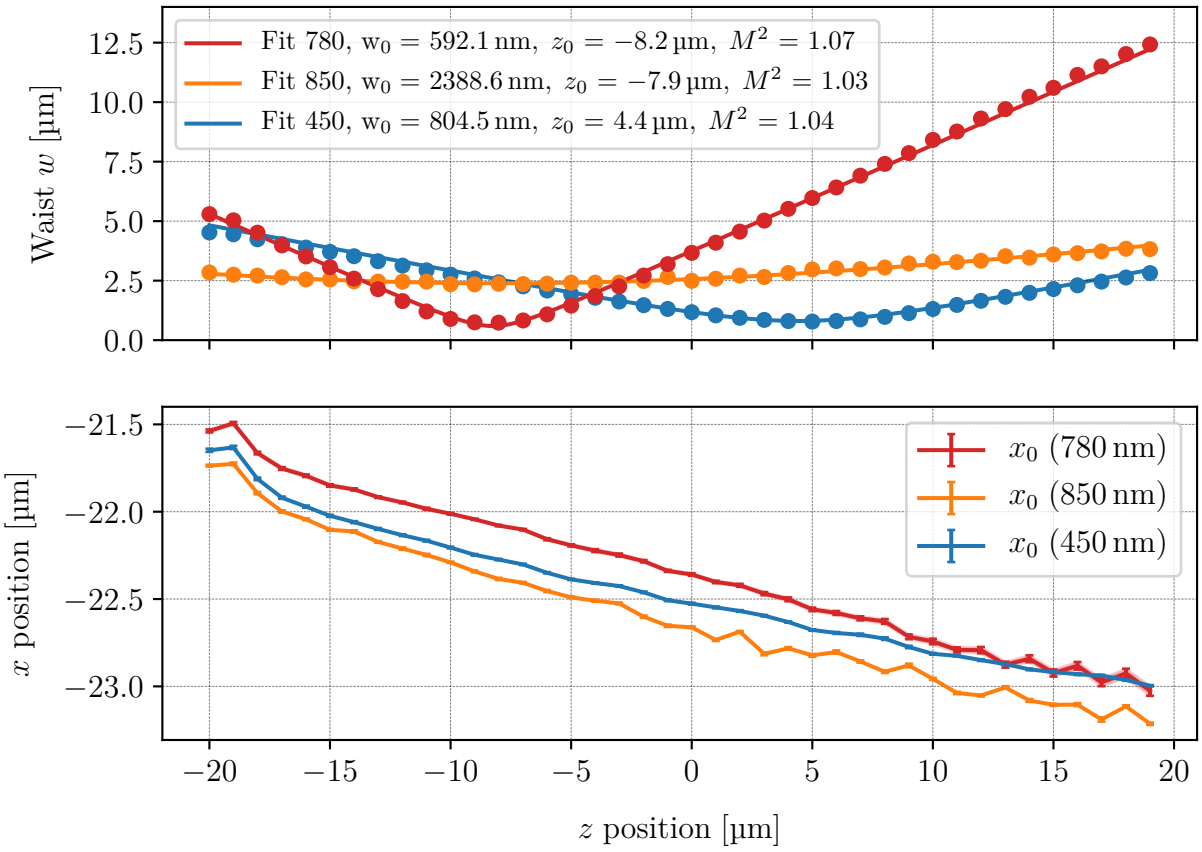

Figure 5.3: Horizontal focus scan.
(top) The beam waist is shown as a function of longitudinal displacement for all three beams. Since it was not possible to provide a 473 nm laser source, the ionization laser was adjusted with an offset of 13 µm to account for the chromatic effect between 450 nm and 473 nm. The other two beams are overlapped longitudinally with a precision of 0.3 µm.
(bottom) The horizontal focus position is shown as a function of longitudinal displacement for all three beams. The three beams are horizontally overlapped with a precision of 250 nm.

5.2.4 Assembly in the main experiment

Since the complete optical setup is pre-aligned on a single breadboard, the implementation in the main experiment is rather simple. It is only necessary to replace the old optical setup with the new breadboard and align it accordingly to the rest of the setup. In contrast to Section 5.2, the glass cell of the vacuum chamber can not be tilted. Therefore, the complete breadboard of the optical setup must be tilted to achieve the necessary alignment of the glass cell. The same technique as described in Section 5.2 is used for the alignment. Since

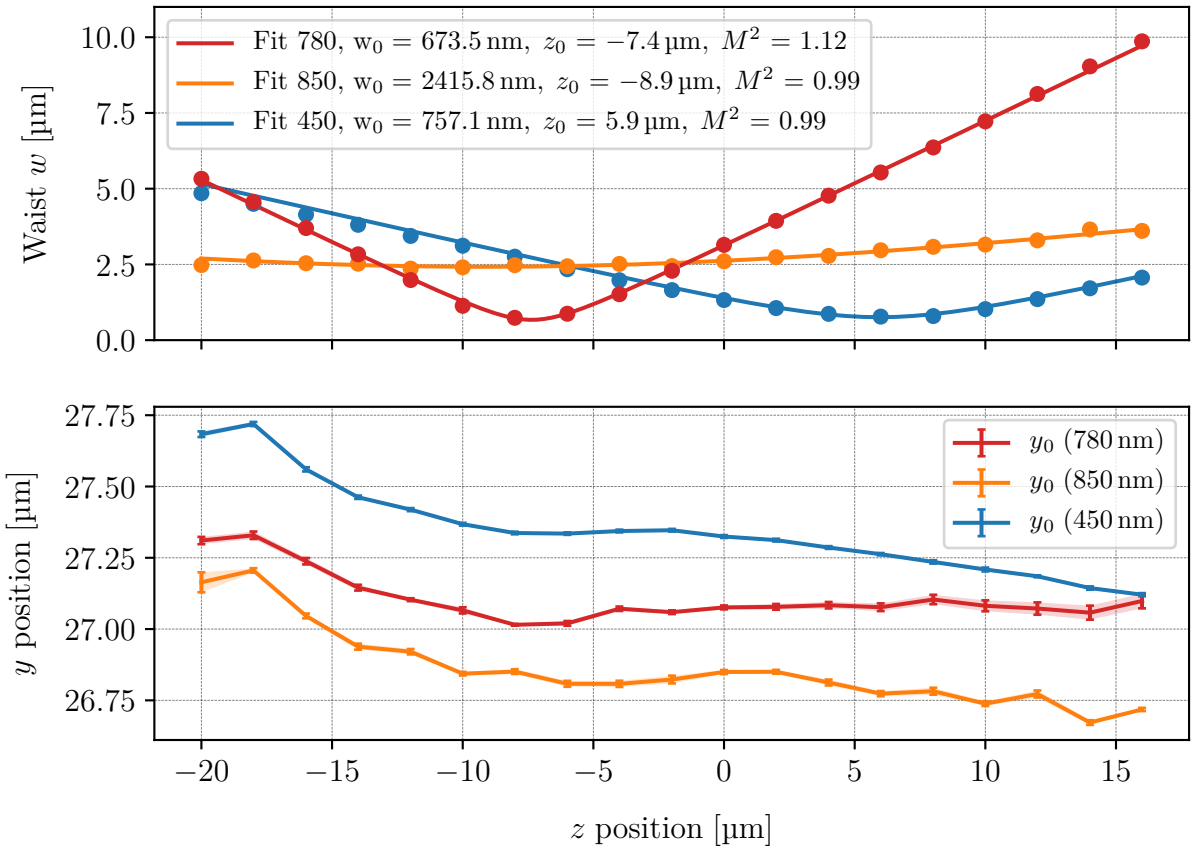

Figure 5.4: Vertical focus scan.
(top) The beam waist is shown as a function of longitudinal displacement for all three beams. Since it was not possible to provide a 473 nm laser source, the ionization laser was adjusted with an offset of 13 µm to account for the chromatic effect between 450 nm and 473 nm. The other two beams are overlapped longitudinally with a precision of 1.5 µm.
(bottom) The vertical focus position is shown as a function of longitudinal displacement for all three beams. The three beams are vertically overlapped with a precision of 500 nm.

the breadboard is mounted on feet which are adjustable for height, it is possible to adjust the height and vertical tilt. With the help of fine thread screws, the necessary precision of the horizontal position and horizontal rotation is achieved. Once atoms are trapped and fluorescence light is collected by the objective, it is possible to optimize the transverse position of the ODT beam with this signal. A fine adjustment of different laser frequencies and intensities can be done by suitable measurements. Thus it is possible to optimize the process of state preparation and read-out.

5.3 Performance analysis of the new setup

In contrast to the optical setup[5] described in [55] and built-in laboratory 1, the waist of the ODT of the new optical setup is slightly larger $w_0 = (2402.2 \pm 13.6)\,\mathrm{nm}$. Therefore, the measured trap frequencies ($\omega_\mathrm{r} = 2\pi \cdot 62.5\,\mathrm{kHz}$, $\omega_\mathrm{z} = 2\pi \cdot 5.0\,\mathrm{kHz}$) and standard deviations of the thermal distribution ($\sigma_\mathrm{r} = 172.5\,\mathrm{nm}$, $\sigma_\mathrm{z} = 2.15\,\mu\mathrm{m}$) are different. This leads to a decrease in collection and coupling efficiency $\eta_\mathrm{cc}^{(\mathrm{H,H})\vee(\mathrm{V,V})}(w_\mathrm{coll}/R_\mathrm{eff} = 0.82) = 3.10\,\%$ and success probability $P_\mathrm{A,P,sim}(d \approx 3\,\mathrm{m}) \approx (1.00 \pm 0.19)\,\%$ after taking all loss mechanisms into account (see Section 3.3). Even if the larger ODT waist decreases the success probability by a factor of 0.84, this tradeoff is necessary to decrease longitudinal field components of the ODT and therefore increase the coherence of the atomic qubit (see Subsection 2.5.1). Furthermore, it is necessary to consider the impact of astigmatism on the ODT. A simple approximation to include the measured longitudinal separation of horizontal and vertical focus in the simulations is given by the density distribution of a sum of two spatially separated harmonic oscillators[6]. If the ODT is perfectly aligned with respect to the fluorescence beam, but the measured separation of horizontal, respectively vertical focus ($z_1 - z_2 = 1.8\,\mu\mathrm{m}$) is assumed, the collection and coupling efficiency and the success probability further drop $\eta_\mathrm{cc}^{(\mathrm{H,H})\vee(\mathrm{V,V})}(w_\mathrm{coll}/R_\mathrm{eff} = 0.82) = 2.97\,\%$ respectively $P_\mathrm{A,P,sim}(d \approx 3\,\mathrm{m}) \approx (0.96 \pm 0.18)\,\%$. Simulating the measured system, which is misaligned longitudinally and transversely[7], yields $\eta_\mathrm{cc}^{(\mathrm{H,H})\vee(\mathrm{V,V})}(w_\mathrm{coll}/R_\mathrm{eff} = 0.82) = 1.99\,\%$, $P_\mathrm{A,P,sim}(d \approx 3\,\mathrm{m}) \approx (0.65 \pm 0.12)\,\%$. An overview of the collection and coupling efficiencies as well as the success probabilities are shown in Table 5.1.

After optimizing the pumping process as well as the collection and coupling process (see Subsection 5.2.4), it is possible to measure a success probability of $P_\mathrm{A,P,exp}(d \approx 3\,\mathrm{m}) = 0.86\,\%$ by scanning the optical power of the excitation laser (see Figure 5.5). This result is somehow astonishing, since the success probability is improved by a factor of 1.26 in contrast to the setup described in [55]. It could be assumed that the self-made fiber collimator leads to an improvement of 1.04, but the higher waist of the ODT decreases the success probability by a factor of 0.84. This should lead to a net decrease of 0.87 and therefore a success probability of 0.59 %. Further effects which could explain this difference are given by: the unknown efficiencies of the APDs, the losses of fiber to fiber connectors and the uncoated fiber tip of the fluorescence collection of the setup described in [55]. However, the measured success probability of 0.86 % nearly reflects the simulated value of $(0.96 \pm 0.18)\,\%$ in case of optimal alignment. The reasons for this difference might be residual misalignment, the impact of wave aberrations or so far unconsidered effects, e.g. longitudinal field components, which might influence the coupling efficiency. These

[5] The waist of the ODT is given by $w_0 = (2059.5 \pm 17.7)\,\mathrm{nm}$ [55], the trap frequencies by $\omega_\mathrm{r} = 2\pi \cdot 79.5\,\mathrm{kHz}$, $\omega_\mathrm{z} = 2\pi \cdot 7.4\,\mathrm{kHz}$ and the standard deviations of the density distribution by $\sigma_\mathrm{r} = 135.7\,\mathrm{nm}$, $\sigma_\mathrm{z} = 1.45\,\mu\mathrm{m}$ (see Subsection 2.2.3).

[6] $n(r,z,T) = \frac{1}{2\,(2\pi)^{3/2}\,\sigma_\mathrm{z}\,\sigma_\mathrm{r}^2}\,(e^{-\frac{(z-z_1)^2}{2\sigma_\mathrm{z}^2}}\,e^{-\frac{(x-x_1)^2+(y-y_1)^2}{2\sigma_\mathrm{r}^2}} + e^{-\frac{(z-z_2)^2}{2\sigma_\mathrm{z}^2}}\,e^{-\frac{(x-x_2)^2+(y-y_2)^2}{2\sigma_\mathrm{r}^2}})$.

[7] $z_1 = 0.3\,\mu\mathrm{m}$, $z_2 = -1.5\,\mu\mathrm{m}$, $x_1 = 0.25\,\mu\mathrm{m}$, $x_2 = 0.25\,\mu\mathrm{m}$, $y_1 = 0.25\,\mu\mathrm{m}$, $y_2 = 0.25\,\mu\mathrm{m}$.

effects as well as the difference between expected and measured performance of the optical system described in [55] (see Table 5.1), should be part of future research.

	Collection and coupling efficiency $\eta_{\mathrm{cc}}^{(\mathrm{H,H})\vee(\mathrm{V,V})}$	Success probability $P_{\mathrm{A,P,sim}}(d \approx 3\,\mathrm{m})$
Optical setup described in [55]		
Simulation for optimal alignment	3.67 %	(1.19 ± 0.23) %
Measurement	-	0.68 %
New optical setup		
Simulation for optimal alignment	3.10 %	(1.00 ± 0.19) %
Simulation for optimal alignment and astigmatism effects of ODT	2.97 %	(0.96 ± 0.18) %
Simulation for measured alignment (see Section 5.2)	1.99 %	(0.65 ± 0.12) %
Measurement	-	0.86 %

Table 5.1: Overview of the collection and coupling efficiency as well as the success probability for the optical setup described in [55] and the new optical setup.

In contrast to the atom-atom entanglement rate of 2.13 events/min in the Bell test of 2016 [10], a rate of 8.36 events/min is measured after implementing the two new high NA microscope optical setups described in [55] and in this thesis. Even if the entanglement rate is the most relevant number with respect to quantum communication applications, the comparison using it can be misleading. The event rate reflects the overall performance of the experiment (e.g. involving the duty cycle probability P_{duty}, see Subsection 2.5.2) and not only the optical performance. Therefore, it is more reasonable to consider the atom-atom entanglement efficiency, which relates the number of excitation tries to the number of successfully entangled atom pairs. In 2016, the efficiency was given by 1.104 ppm, while using the new optical setups, it increased to 6.154 ppm. This corresponds to an improvement factor of 5.57 which is slightly lower than the expected value of 6.25. Nevertheless, this success confirms all the effort, which was made in the recent years to optimize the optical performance and demonstrates the validity of the alignment techniques and the optical characterization.

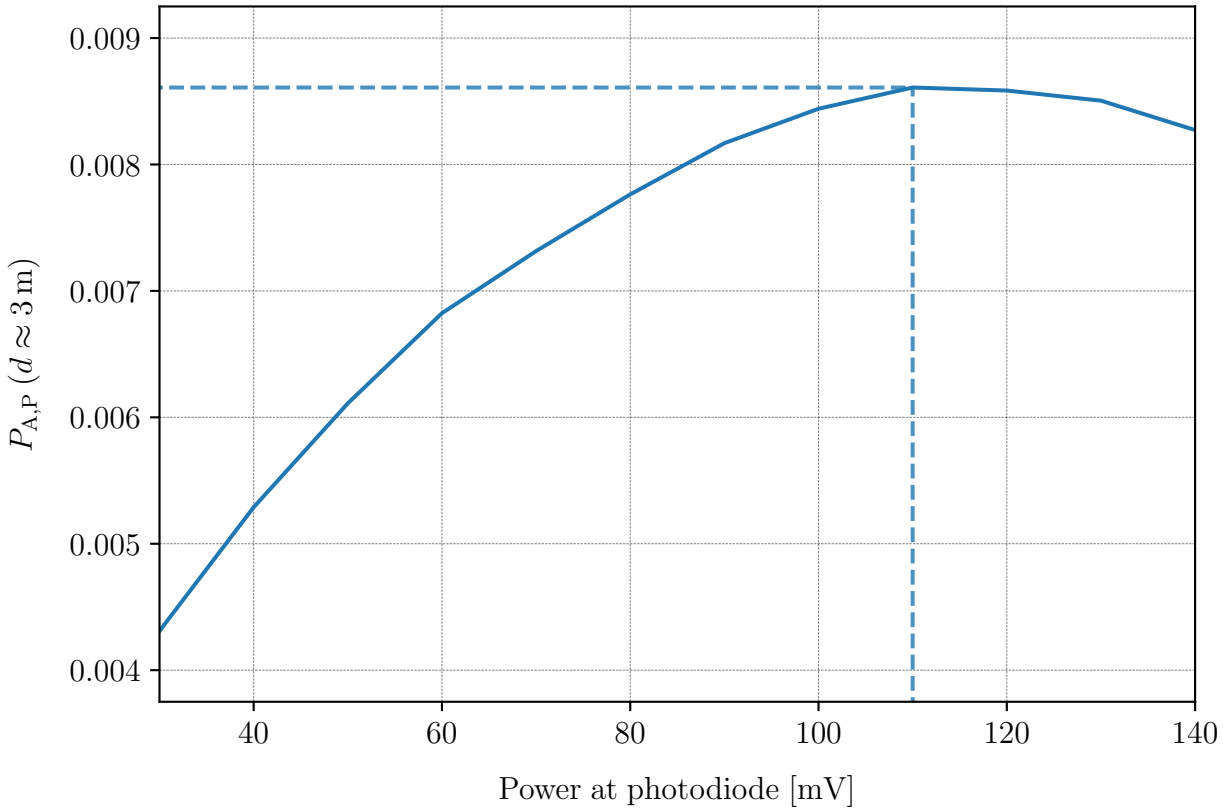

Figure 5.5: Optical power scan of the excitation laser. The success probability $P_{\mathrm{A,P}}$ is shown as a function of the power of the ionization laser at the photodiode. A maximal success probability of 0.86 % is achieved.

Chapter 6

Conclusion and outlook

For future quantum communication applications, it is mandatory to increase the distance of entangled quantum memories. In entanglement generation schemes based on entanglement swapping, this distance is mainly limited by the event rate. This thesis, describes an increase in entanglement rate by analyzing and optimizing the process of collection and coupling of single photons. A new optical setup was implemented, involving a custom made objective and a self-made fiber collimator. Implementing quantum frequency conversion, it is presumably possible to increase the distance between two entangled ^{87}Rb atoms from 398 m to 20 km.

First of all, a method was developed to describe the process of collection and coupling of single photons. The collection and coupling efficiency consists of two nearly independent factors: the probability that a photon is emitted into the entrance pupil of the objective and the probability that an already collected photon is coupled into a single mode fiber. It was shown that the coupling efficiency depends on the polarization of the photon and fiber mode. In principle three different possibilities can occur. Most likely the same polarization as emitted is coupled into the fiber. However, if the atom is displaced from the center of the trap, there is a finite probability that the orthogonal polarization as emitted or a π photon is coupled in. In consideration of the thermal distribution of the atom inside an optical dipole trap at a temperature of $T = 48\,\mu\mathrm{K}$, the total collection and coupling efficiency of the new objective is given by $\eta_{\mathrm{cc}}^{(\mathrm{H,H})\vee(\mathrm{V,V})} = 3.81\,\%$. The probability that either the orthogonal polarization as emitted or π photons are coupled into the fiber are negligible. This reflects the experimental findings. A significant decrease in atom-photon fidelity caused by a coupling of the wrong polarization could not be observed. The collection and coupling efficiency of the simulation differed by a factor of 1.75 from the experimentally observed efficiency obtained by the setup described in [55]. Since a lot of effects are not considered in these simulations (e.g. misalignment, wave aberrations) and the uncertainty of the experimental value (e.g. detection efficiency, transmission of the interference filter) could not be estimated properly, the congruence between simulated and experimental efficiency might be even better. Furthermore, these simulations revealed that the maximal collection and coupling efficiency is only obtained by choosing a suitable fiber collimator with

a collimated fiber waist of $w_{\mathrm{coll}} = 4.1\,\mathrm{mm}$. This leads to a relative improvement of 3.7 % with regard to the previously used fiber collimator with a waist of $w_{\mathrm{coll}} = 3.5\,\mathrm{mm}$. Since there was no commercially available fiber collimator that satisfied all the requirements for this experiment, a lens system for a suitable fiber collimator was designed and assembled under clean room conditions.

The intensity profiles of this fiber collimator revealed a small amount of wave aberrations at a collimated waist of $w_{\mathrm{coll}} = 4.1\,\mathrm{mm}$. To quantify the aberrations of the fiber collimator and fully characterize the objective, the point spread functions of these two optical elements were measured and analyzed. For this measurement it was necessary to create a point source. After several failures, a pinhole with a diameter of 362 nm milled by a focused ion beam achieved a satisfactory emission profile. To measure the point spread function, a suitable experimental setup was established. The development of a fitting algorithm, involving a linear least squares minimization process between the measured and simulated point spread function, enabled the determination of the most important parameters of an optical system. A numerical aperture of 0.5185 ± 0.0011 and a Strehl ratio of $0.9978\,^{+0.0022}_{-0.0075}$ was obtained for the objective. The objective operates diffraction limited up to a longitudinal displacement of 1.75 µm, a transverse displacement of $(353 \pm 15)\,\mu\mathrm{m}$ and a tilt of the window of the vacuum chamber of $(0.43 \pm 0.01)°$. This agrees with the measurements by Photon Gear in many aspects. Nevertheless, the numerical aperture is 3.8 % higher than originally assumed. The self-made fiber collimator revealed a numerical aperture of 0.1873 ± 0.0004, a Strehl ratio of $0.9921\,^{+0.0079}_{-0.0100}$ and operates diffraction limited up to a longitudinal shift of $> 8\,\mu\mathrm{m}$, a transverse shift of $(0.71 \pm 0.08)\,\mathrm{mm}$ and a tilt of $> 1.2°$. This robustness against misalignment most likely turns up due to the large manufacturing tolerances considered in the lens design.

Finally, the optical setup containing the custom made objective and the self-made fiber collimator was pre-aligned and implemented in the single atom trap experiment. The measurement of the success probability revealed a value of 0.86 %. This closely reflects the simulated value of $(0.96 \pm 0.18)\,\%$ in case of optimal alignment. In contrast to previous measurements, a gain of 3.7 in collection efficiency was obtained with the new setup. This led to an increase of 5.57 in atom-atom entanglement efficiency. Implementing a second apparatus for quantum frequency conversion, with the same external device conversion efficiency as described in [71], an event rate of 7.93 events/min should be obtained within a fiber length of 700 m. Assuming a symmetric setup and a distance of 20 km, an entanglement rate of 0.60 events/min can be expected. This is a feasible value for demonstrating long distance entanglement of atomic qubits and a first step towards quantum communication applications using entanglement swapping protocol.

While the new optical setup nearly reflects the simulated values, the success probability of the optical setup built-in laboratory 1 differs significantly from the simulations. Therefore, a first part of future research will be the investigation of this difference. A possible reason for this difference might be the performance of the single atom trap experiment apart from

the collection process. The success probability is not only influenced by the collection and coupling efficiency but also by the detection efficiency and several loss mechanisms between objective and detectors, e.g. a non anti-reflection coated fiber tip and a fiber to fiber connector. Moreover, the objective, the 780 nm fiber collimator as well as the 850 nm fiber collimator are not characterized so far. Wave aberrations might affect the collection and coupling process.

If the involved optical systems operate diffraction limited, a significant influence on the collection and coupling efficiency caused by aberrations can not be expected. However, the exact impact of wave aberrations on the mode overlap has not been investigated so far. Due to numerical issues, this might be a challenging task. Nevertheless, two crucial effects on the collection and coupling efficiency simulations are left for consideration. First, a tightly focused beam leads to longitudinal field components. It is not quite sure, how this affects the coupling process. Secondly, the beam profile of the ODT might be distorted by the influence of aberrations. This leads to a change in density distribution which needs to be considered. In first approximations, the influence of astigmatism reduces the collection and coupling efficiency by a factor of 0.96. However, to estimate the overall influence of ODT wave aberrations, it is necessary to characterize the fiber collimator of the ODT. Thus, it is possible to simulate the outcome of wave aberrations on the density distribution and thereby the effect on collection and coupling efficiency. Nevertheless, it is recommended to build a fiber collimator for the optical dipole trap according to the needs of this experiment. Since the process of designing and assembling a fiber collimator for the 780 nm light was already successful, this know-how can be used to build a ODT fiber collimator. A suitable lens design for 849 nm up to 862 nm light is already prepared (see Appendix D), however due to lack of time, it was not realized yet.

An increase of the overall performance of the experiment can be obtained by using a standing wave dipole trap (SWDT). If the counter propagating beams are sufficiently aligned, atomic state dephasing effects caused by longitudinal field components can be highly suppressed [69]. Moreover, the density distribution of the atom within this dipole trap changes completely. By analyzing the amount of fluorescence light, it is possible to estimate the location of the atom. If it is possible to select atoms, which are located within a few centered pockets, the collection and coupling efficiency can be increased compared to the running wave dipole trap. The change in collection and coupling efficiency induced by localizing the atom within the SWDT is shown in Figure 6.1. The standing wave approach is the most promising one for a further increase of the distance between the two quantum memories.

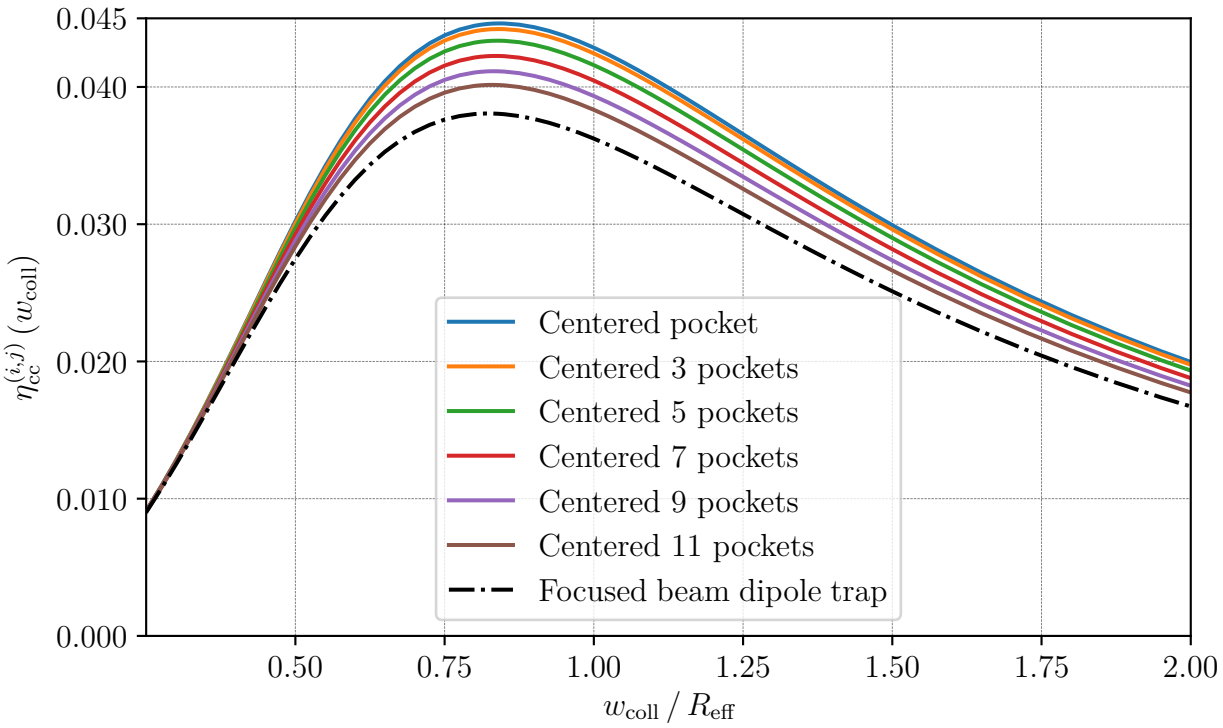

Figure 6.1: The collection and coupling efficiency versus the width of the fiber mode for several delocalizations within a standing wave dipole trap. If it is possible to localize the atom within the SWDT, the efficiency can be increased up to 4.46 %, this is an increase of 17 % compared to the current focused beam dipole trap.

Appendices

A Overview of the laser system and transition frequencies

To control and manipulate the ^{87}Rb quantum state, different laser beams with frequencies addressing different atomic transitions are used (see Figure A.1). Each beam is generated by one of three diode-lasers which are frequency stabilized using Doppler-free saturation spectroscopy. Additionally, the laser system consists of the free running dipole trap and ionization laser. A combination of a half-wave plate and a PBS makes it possible to set the relative power ratio between the PBS outputs. This is used for a coarse power tuning. Acousto-optical modulators (AOMs) fine-tune the optical power and switch the beams on and off. To address single hyperfine levels, AOMs fine-tune the laser frequency [48]. The following listing illustrates the different lasers of the laser system and their transitions.

Cooling laser: Drives the $5^2S_{1/2}$, F = 2 $\rightarrow$ $5^2P_{3/2}$ transitions at a wavelength of 780.24 nm. Using AOMs, the following hyperfine transitions are addressed:

- Cooling
- Pump $_{2\rightarrow1}$
- Cycling

Repump laser: Drives the $5^2S_{1/2}$, F = 1 $\rightarrow$ $5^2P_{3/2}$ transitions at a wavelength of 780.24 nm. Using AOMs, the following hyperfine transitions are addressed:

- Repump
- Pump $_{1\rightarrow1}$
- Excitation

Readout laser: Drives the $5^2S_{1/2}$, F = 1 $\rightarrow$ $5^2P_{1/2}$, F' = 1 transition at a wavelength of 794.98 nm.

Ionization laser: Ionizes atoms at a wavelength of 473 nm.

Dipole trap laser: Optically traps atoms at a wavelength of 850 nm respectively 857 nm.

In total, 5 different lasers drive 9 different transitions. An application sorted overview of the transitions is shown in Figure A.1. The transitions are colored according to the laser which drives the transition.
For some applications, the direction of incidence of the laser beam onto the atom is crucial, e.g. MOT or π polarized light. Figure A.2 gives an overview of the different laser beams within the optical setup with a view from the top A.2 (a) and front A.2 (b).

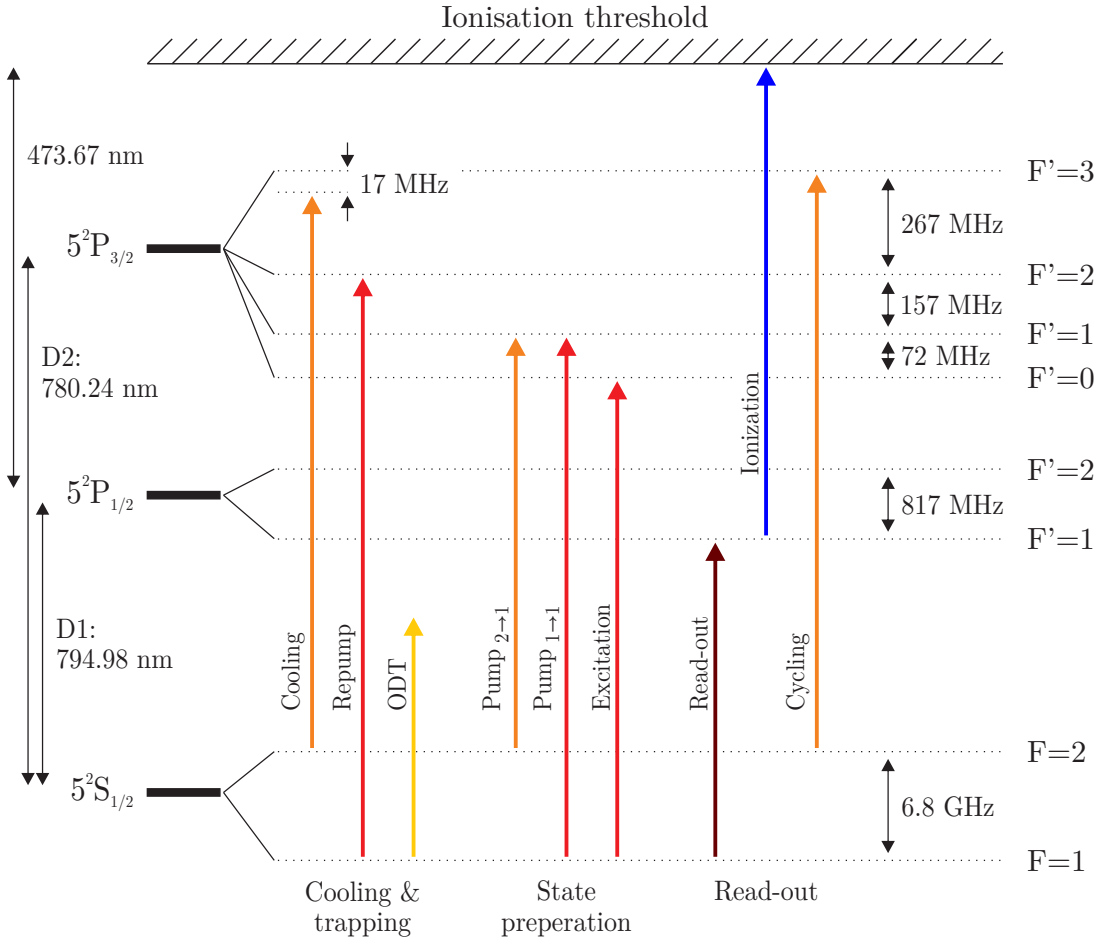

Figure A.1: Overview of all transitions used in the experiment. The different transitions are sorted by their application: "Cooling & trapping", "State preparation" and "Read-out". The color of the transitions indicate the laser which drives the individual transition: "Cooling": orange, "Repump": red, "Read-out": brown, "ODT": yellow and "Ionization": blue.

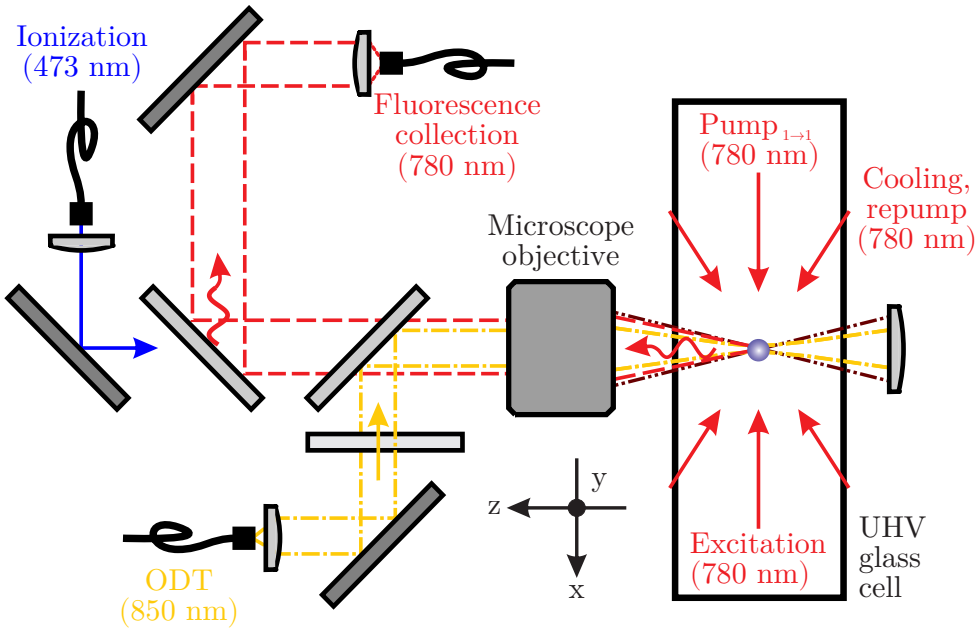

(a) Top view of the optical setup.

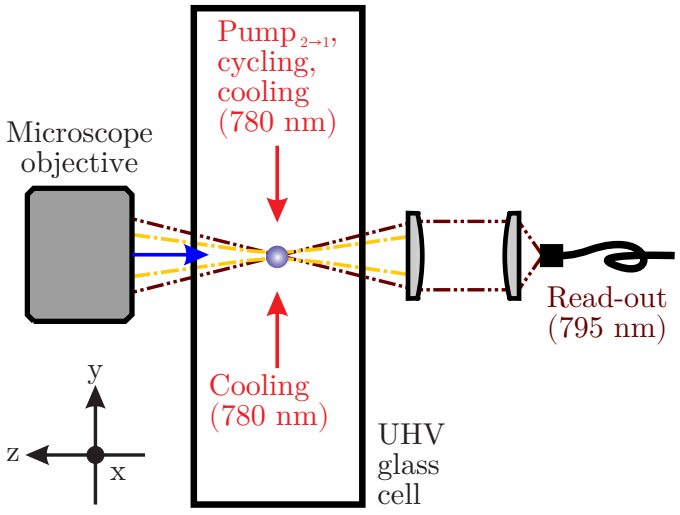

(b) Front view of the optical setup.

Figure A.2: Schematic of the optical setup containing all nine laser beams with a view from the top and front.

B Basis definitions of photonic and atomic qubits

Photon and atom measurements performed in different bases require a consistent definition of the bases, their eigenstates and transformations between them. The direction of photon collection, in that case the optical axis of the microscope objective, defines the quantization axis of the atom. As customary, this direction is referred to the z-axis in the laboratory frame. The x-axis is defined parallel to the optical table and orthogonal to the z-axis. The y-axis is defined perpendicular to the x-z-plane (optical table). This coordinate system is right-hand oriented.

Photon polarizations and basis transformations for photonic qubits

The following definitions for π polarized light and the three different photon polarizations qubit sets ($\{\sigma^+, \sigma^-\}$, {H, V}, {+, -}) are used [38]:

σ^+: Right-handed circular polarized light in direction of propagation. It carries a momentum of $m_F = +1$. σ^+ polarized light is also referred to as L polarized light.

σ^-: Left-handed circular polarized light in direction of propagation. It carries a momentum of $m_F = -1$. σ^- polarized light is also referred to as R polarized light.

π: Linear polarized light with the electric field vector parallel to the z-axis. It carries a momentum of $m_F = 0$.

H: Linear polarized light with the electric field vector parallel to the x-axis.

V: Linear polarized light with the electric field vector parallel to the y-axis.

+: Linear polarized light with the electric field vector rotated by 45° right-hand side in direction of propagation with respect to V.

-: Linear polarized light with the electric field vector rotated by 45° left-hand side in direction of propagation with respect to V.

Since the propagation direction for collected photons emitted by the atom as well as the read-out laser is +z, these definitions match for both. Basis transformations of the photonic qubit between different polarizations are defined according to [38] are shown in Table B.1.

Atomic qubit states

The basis of measurements of the atomic qubit is set by the polarization of the read-out pulse. Three different sets of basis vectors ($\{|\uparrow\rangle_x, |\downarrow\rangle_x\}$, $\{|\uparrow\rangle_y, |\downarrow\rangle_y\}$, $\{|\uparrow\rangle_z, |\downarrow\rangle_z\}$) will be defined. These sets of basis vectors are the eigenvectors of the Pauli-operators $\hat{\sigma}_x$, $\hat{\sigma}_y$ and $\hat{\sigma}_z$ [48]. The transformation rules for a change of basis set are shown in Table B.2 [65].

Polarization state	Decomposition in $\|\sigma^+\rangle$ and $\|\sigma^-\rangle$	E-field for light propagating in z-direction
$\|\mathrm{L}\rangle$	$\|\sigma^+\rangle$	$\frac{1}{\sqrt{2}}\,\|\|E\|\| \begin{pmatrix} 1 \\ e^{-i\frac{\pi}{2}} \\ 0 \end{pmatrix} e^{i(wt-kz)}$
$\|\mathrm{R}\rangle$	$\|\sigma^-\rangle$	$\frac{1}{\sqrt{2}}\,\|\|E\|\| \begin{pmatrix} 1 \\ e^{+i\frac{\pi}{2}} \\ 0 \end{pmatrix} e^{i(wt-kz)}$
$\|\mathrm{H}\rangle$	$\frac{1}{\sqrt{2}}\left(\|\sigma^+\rangle + \|\sigma^-\rangle\right)$	$\|\|E\|\| \begin{pmatrix} 1 \\ 0 \\ 0 \end{pmatrix} e^{i(wt-kz)}$
$\|\mathrm{V}\rangle$	$\frac{i}{\sqrt{2}}\left(\|\sigma^+\rangle - \|\sigma^-\rangle\right)$	$\|\|E\|\| \begin{pmatrix} 0 \\ 1 \\ 0 \end{pmatrix} e^{i(wt-kz)}$
$\|+\rangle$	$\frac{1}{\sqrt{2}}\, e^{i\frac{\pi}{4}}\left(\|\sigma^+\rangle - i\,\|\sigma^-\rangle\right)$	$\frac{1}{\sqrt{2}}\,\|\|E\|\| \begin{pmatrix} 1 \\ 1 \\ 0 \end{pmatrix} e^{i(wt-kz)}$
$\|\text{-}\rangle$	$\frac{-1}{\sqrt{2}}\, e^{-i\frac{\pi}{4}}\left(\|\sigma^+\rangle + i\,\|\sigma^-\rangle\right)$	$\frac{1}{\sqrt{2}}\,\|\|E\|\| \begin{pmatrix} -1 \\ 1 \\ 0 \end{pmatrix} e^{i(wt-kz)}$

Table B.1: Definitions for basis transformations of the phtonic qubit.

Atomic qubit state	Decomposition in $\|\uparrow\rangle_\mathrm{z}$ and $\|\downarrow\rangle_\mathrm{z}$
$\|\uparrow\rangle_\mathrm{z}$	$\|\uparrow\rangle_\mathrm{z}$
$\|\downarrow\rangle_\mathrm{z}$	$\|\downarrow\rangle_\mathrm{z}$
$\|\uparrow\rangle_\mathrm{x}$	$\frac{1}{\sqrt{2}}\left(\|\uparrow\rangle_\mathrm{z} + \|\downarrow\rangle_\mathrm{z}\right)$
$\|\downarrow\rangle_\mathrm{x}$	$\frac{i}{\sqrt{2}}\left(\|\uparrow\rangle_\mathrm{z} - \|\downarrow\rangle_\mathrm{z}\right)$
$\|\uparrow\rangle_\mathrm{y}$	$\frac{1}{\sqrt{2}}\, e^{i\frac{\pi}{4}}\left(\|\uparrow\rangle_\mathrm{z} - i\,\|\downarrow\rangle_\mathrm{z}\right)$
$\|\downarrow\rangle_\mathrm{y}$	$\frac{-1}{\sqrt{2}}\, e^{-i\frac{\pi}{4}}\left(\|\uparrow\rangle_\mathrm{z} + i\,\|\downarrow\rangle_\mathrm{z}\right)$

Table B.2: Definitions for basis transformations of the atomic qubit.

Entangled pair of photonic and atomic qubit

The relations given in Table B.1 and B.2 lead to the following basis transformation for the entangled atom-photon state:

$$|\Psi\rangle_{\mathrm{A,P}} = \frac{1}{\sqrt{2}}(|\mathrm{L}\rangle\,|\downarrow\rangle_{\mathrm{z}} + |\mathrm{R}\rangle\,|\uparrow\rangle_{\mathrm{z}}) \tag{B.1}$$

$$= \frac{1}{\sqrt{2}}(|\mathrm{H}\rangle\,|\downarrow\rangle_{\mathrm{x}} + |\mathrm{V}\rangle\,|\uparrow\rangle_{\mathrm{x}}) \tag{B.2}$$

$$= \frac{1}{\sqrt{2}}(|+\rangle\,|\downarrow\rangle_{\mathrm{y}} + |\text{-}\rangle\,|\uparrow\rangle_{\mathrm{y}}). \tag{B.3}$$

Therefore, basis transformations maintain entanglement.

Bright and dark states of different read-out polarizations

The bright and dark states define the ionized respectively not ionized atomic qubit states in the ideal ionization scheme (see Section 2.3.3) for a given read-out polarization. Basis transform the Equations 2.8 and 2.9 by using the relations given in Table B.1 and B.2, bright and dark states can be expressed in three previously presented bases [65]. The corresponding bright and dark states for the six different read-out polarizations are given in Table B.3:

Read-out state	Bright state $\lvert\Psi_{\mathrm{B}}\rangle$	Dark state $\lvert\Psi_{\mathrm{D}}\rangle$
$\lvert\mathrm{L}\rangle$	$\lvert\downarrow\rangle_{\mathrm{z}}$	$\lvert\uparrow\rangle_{\mathrm{z}}$
$\lvert\mathrm{R}\rangle$	$\lvert\uparrow\rangle_{\mathrm{z}}$	$\lvert\downarrow\rangle_{\mathrm{z}}$
$\lvert\mathrm{H}\rangle$	$\lvert\downarrow\rangle_{\mathrm{x}} = \frac{i}{\sqrt{2}}(\lvert\uparrow\rangle_{\mathrm{z}} - \lvert\downarrow\rangle_{\mathrm{z}})$	$\lvert\uparrow\rangle_{\mathrm{x}} = \frac{1}{\sqrt{2}}(\lvert\uparrow\rangle_{\mathrm{z}} + \lvert\downarrow\rangle_{\mathrm{z}})$
$\lvert\mathrm{V}\rangle$	$\lvert\uparrow\rangle_{\mathrm{x}} = \frac{1}{\sqrt{2}}(\lvert\uparrow\rangle_{\mathrm{z}} + \lvert\downarrow\rangle_{\mathrm{z}})$	$\lvert\downarrow\rangle_{\mathrm{x}} = \frac{i}{\sqrt{2}}(\lvert\uparrow\rangle_{\mathrm{z}} - \lvert\downarrow\rangle_{\mathrm{z}})$
$\lvert+\rangle$	$\lvert\downarrow\rangle_{\mathrm{y}} = \frac{-1}{\sqrt{2}}\,e^{-i\frac{\pi}{4}}(\lvert\uparrow\rangle_{\mathrm{z}} + i\,\lvert\downarrow\rangle_{\mathrm{z}})$	$\lvert\uparrow\rangle_{\mathrm{y}} = \frac{1}{\sqrt{2}}\,e^{i\frac{\pi}{4}}(\lvert\uparrow\rangle_{\mathrm{z}} - i\,\lvert\downarrow\rangle_{\mathrm{z}})$
$\lvert\text{-}\rangle$	$\lvert\uparrow\rangle_{\mathrm{y}} = \frac{1}{\sqrt{2}}\,e^{i\frac{\pi}{4}}(\lvert\uparrow\rangle_{\mathrm{z}} - i\,\lvert\downarrow\rangle_{\mathrm{z}})$	$\lvert\downarrow\rangle_{\mathrm{y}} = \frac{-1}{\sqrt{2}}\,e^{-i\frac{\pi}{4}}(\lvert\uparrow\rangle_{\mathrm{z}} + i\,\lvert\downarrow\rangle_{\mathrm{z}})$

Table B.3: Bright and dark states for the six different read-out polarizations.

C General expressions of the dipole emission characteristic

The dipole emission characteristic $\mathrm{d}P^{(\mathrm{i})}_{\mathrm{photon}}(\mathbf{r})$ is defined in Equation 3.9. Assuming an arbitrary oscillation direction $\mathbf{e}_{\mathrm{p}} = (e_{\mathrm{x}}, e_{\mathrm{y}}, e_{\mathrm{z}})$ with $|e_{\mathrm{x}}|^2 + |e_{\mathrm{y}}|^2 + |e_{\mathrm{z}}|^2 = 1$, the general expression for the emission characteristics is obtained:

$$\mathrm{d}P^{(\mathrm{p})}_{\mathrm{photon}}(\mathbf{r}) = \frac{1}{N_{\mathrm{norm}}}\,\mathrm{d}\Omega\, r^2\, \mathbf{E}^{(\mathrm{i})}(\mathbf{r}) \cdot (\mathbf{E}^{(\mathrm{i})}(\mathbf{r}))^* \tag{C.1}$$

$$\begin{aligned} = \mathrm{d}\Omega\, \frac{3}{16\pi} \Big(& 1 + \cos(2\theta) - 2\,|e_{\mathrm{z}}|^2 \cos(2\theta) \\ & + 2\,[e_{\mathrm{y}}\cos(\phi) - e_{\mathrm{x}}\sin(\phi)]^*\,[e_{\mathrm{y}}\cos(\phi) - e_{\mathrm{x}}\sin(\phi)]\sin^2(\theta) \\ & - \{e_{\mathrm{z}}\,(e_{\mathrm{x}})^*\cos(\phi) + e_{\mathrm{z}}\,(e_{\mathrm{y}})^*\sin(\phi) \\ & \quad + (e_{\mathrm{z}})^*\,[e_{\mathrm{x}}\cos(\phi) + e_{\mathrm{y}}\sin(\phi)]\}\sin^2(2\theta)\Big)\,. \end{aligned} \tag{C.2}$$

Projection onto the Cartesian coordinate system

In Cartesian coordinates, the dipole emission characteristic for an arbitrary oscillation direction $\mathbf{e}_{\mathrm{p}} = (e_{\mathrm{x}}, e_{\mathrm{y}}, e_{\mathrm{z}})$ lead to the following expression:

$$\mathrm{d}P^{(\mathrm{p})}_{\mathrm{photon}}(\mathbf{r}) = \frac{1}{N_{\mathrm{norm}}}\,\mathrm{d}A\, \frac{z}{\sqrt{x^2+y^2+z^2}}\,(x^2+y^2+z^2)\,\mathbf{E}^{(\mathrm{i})}(\mathbf{r}) \cdot (\mathbf{E}^{(\mathrm{i})}(\mathbf{r}))^*, \tag{C.3}$$

$$\begin{aligned} = \mathrm{d}A\, \frac{3\,z}{8\pi\,(x^2+y^2+z^2)^{3/2}} \Big(& y^2 + z^2 - x\,(e_{\mathrm{y}}\,y + e_{\mathrm{z}}\,z)\,(e_{\mathrm{x}})^* \\ & - [e_{\mathrm{x}}\,x\,y + e_{\mathrm{y}}\,(y^2 - x^2) + e_{\mathrm{z}}\,y\,z]\,(e_{\mathrm{y}})^* \\ & - [e_{\mathrm{x}}\,x\,z + e_{\mathrm{y}}\,y\,z + e_{\mathrm{z}}\,(z^2 - x^2)]\,(e_{\mathrm{z}})^*\Big)\,. \end{aligned} \tag{C.4}$$

D Self-designed fiber collimators

The self-made fiber collimator designed for 780 nm light consists of four spherical lenses given in Table D.1. The working distance is given by 10 mm, the effective focal length by 49 mm.

	Surface	Radius [mm]	Thickness [mm]	Material
Fiber	Surface 0	Infinity	10.000	Air
Lens 1	Surface 1	Infinity	2.000	N-BK7
	Surface 2	225.183	17.630	Air
Lens 2	Surface 3	−30.760	10.000	N-SF6
	Surface 4	−25.350	10.660	Air
Lens 3	Surface 5	−102.090	6.280	N-SF6
	Surface 6	−57.540	0.530	Air
Lens 4	Surface 7	635.000	2.900	N-BK7
	Surface 8	−122.460	Infinity	Air

Table D.1: Lens data of the 780 nm self-made fiber collimator.

The fiber collimator designed for 849 - 862 nm light consists of three spherical lenses and one doublet given in Table D.2. The working distance is given by 4 mm, the effective focal length by 16 mm.

	Surface	Radius [mm]	Thickness [mm]	Material
Fiber	Surface 0	Infinity	3.999	Air
Lens 1	Surface 1	Infinity	7.152	N-SF57
	Surface 2	−15.872	0.200	Air
Lens 2	Surface 3	−386.206	6.818	N-SF57
	Surface 4	−45.843	2.520	Air
Lens 3	Surface 5	252.085	10.000	N-SF57
	Surface 6	−46.595	8.057	Air
Doublet 1	Surface 7	41.106	10.000	N-BK10
	Surface 8	−13.044	8.050	N-SF57
	Surface 9	−38.842	Infinity	Air

Table D.2: Lens data of the 849 − 862 nm self-designed fiber collimator.

E Seidel aberrations

In this appendix, monochromatic aberrations of rotationally symmetric optical systems are categorized and characterized by their impact on the image quality. Assuming a wavefront emerging from the exit pupil of an optical system. For a single image point $(x_\mathrm{i}, y_\mathrm{i})$, the wave aberration only depends on the coordinates of the exit pupil $(x_\mathrm{p}, y_\mathrm{p})$. Since for each emitting object point, there is a wavefront with different aberrations converging towards a corresponding image point, the wave aberration is in general a function of pupil and image coordinates $W(x_\mathrm{p}, y_\mathrm{p}, x_\mathrm{i}, y_\mathrm{i})$. For a rotationally symmetric optical system, it is possible to find a coordinate system transformation in which the x_i coordinate vanishes. According to [84, 108], the resulting wave aberration can be expanded as a power series[1] in the three coordinates $x_\mathrm{p}, y_\mathrm{p}, y_\mathrm{i}$:

$$\begin{aligned} W(x_\mathrm{p}, y_\mathrm{p}, y_\mathrm{i}) \equiv\, & W(x_\mathrm{p}^2 + y_\mathrm{p}^2, y_\mathrm{p}\, y_\mathrm{i}, y_\mathrm{i}^2) \\ =\, & a_0 + b_1\,(x_\mathrm{p}^2 + y_\mathrm{p}^2) + b_2\, y_\mathrm{p}\, y_\mathrm{i} \\ & + c_1\,(x_\mathrm{p}^2 + y_\mathrm{p}^2)^2 + c_2\,(x_\mathrm{p}^2 + y_\mathrm{p}^2)\, y_\mathrm{p}\, y_\mathrm{i} + c_3\, y_\mathrm{p}^2\, y_\mathrm{i}^2 + c_4\,(x_\mathrm{p}^2 + y_\mathrm{p}^2)\, y_\mathrm{i}^2 + c_5\, y_\mathrm{p}\, y_\mathrm{i}^3 \\ & + \text{higher order terms}\,. \end{aligned} \tag{E.1}$$

In Equation E.1, the coefficients a_i, b_i, c_i are denoted according to their order of the power series. These terms represent the following well-known aberrations. Their functional expression in polar coordinates of the pupil ($x_\mathrm{p} = r_\mathrm{p}\sin(\phi)$, $y_\mathrm{p} = r_\mathrm{p}\cos(\phi)$) are shown as well:

a_0: 1 term with a sum of exponents of 0.

- a_0: **Piston**: $W = \text{const}$
  This aberration leads to a global phase offset.

b_i: 2 terms with a sum of exponents of 2.

- b_1: **Defocus**: $W = r_\mathrm{p}^2$
  This aberration leads to a longitudinal shift of the focus (see Figure 4.3).
- b_2: **Tilt**: $W = y_\mathrm{i}\, r_\mathrm{p}\cos(\phi)$
  This aberration leads to a transverse shift of the wavefront (see Figure 4.2).

c_i: 5 terms with a sum of exponents of 4.
These terms represent the third order[2] aberrations or Seidel aberrations.

- c_1: **Spherical aberrations**: $W = r_\mathrm{p}^4$
  This aberration leads to different focal lengths for paraxial and marginal rays.

[1] For clarity, irrelevant terms e.g. b_3, c_6 were neglected [86].

[2] This historical expression goes back to the research of Seidel. Since he investigated transverse aberrations, which are obtained by differentiation with respect to the pupil coordinate, the exponential number decreases by one. Therefore, the wave aberrations with order four are called third order aberrations.

c_2: **Coma**: $W = y_\mathrm{i}\, r_\mathrm{p}^3 \cos(\phi)$
This aberration leads to a deviation of magnification within the pupil.

c_3: **Astigmatism**: $W = y_\mathrm{i}^2\, r_\mathrm{p}^2 \cos^2(\phi)$
This aberration leads to different focal length for tangential and sagittal rays.

c_4: **Field curvature**: $W = y_\mathrm{i}^2\, r_\mathrm{p}^2$
This aberration leads to a curvature of the image plane.

c_5: **Distortion**: $W = y_\mathrm{i}^3\, r_\mathrm{p} \cos(\phi)$
This aberration leads to a deformation of the scale across the image field.

The zeroth order (piston) and first order (defocus and tilt) aberrations can be corrected trivially. Adjusting the position of the image plane or the underlying image scale, leads to an unaberrated image. The lowest expansion order introducing real aberrations is the third order, containing the five Seidel aberrations. Moreover, the expansion of Equation E.1 can be continued to 9 fifth order terms. For further information about the individual aberrations, specialist literature is recommended [84, 89].

Comparison to Zernike polynomials

Most of the readers are more familiar with classical Seidel aberrations than with Zernike polynomials. Therefore, a small comparison between these two wave aberration representations is shown in Table E.1.

Property	Seidel aberrations	Zernike polynomials
Possible description of classical wave aberrations	Yes	Yes
Orthogonality	No	Yes
Number of orders	Originally 3 (infinity with power expansion)	Infinity
Dependency on	Image field and aperture	Aperture
Additivity for surface contributions	Yes	No

Table E.1: Comparison between Seidel aberrations and Zernike polynomials. [109]

Bibliography

[1] P. Dirac. The Principles of Quantum Mechanics. Oxford University Press, 1930.

[2] J. von Neumann. Mathematische Grundlagen der Quantenmechanik. Die Grundlehren der mathematischen Wissenschaften. Verlag von Julius Springer, 1932.

[3] M. Planck. Zur Theorie des Gesetzes der Energieverteilung im Normalspectrum. Verhandlungen der deutschen physikalischen Gesellschaft. *FAKSIMILE AUS DEN VERHANDLUNGEN DER DEUTSCHEN PHYSIKALISCHEN GESELLSCHAFT 2*, 1900.

[4] L. de Broglie. Recherches sur la théorie des quanta. PhD thesis, Migration- universit e en cours d'affectation, 1924.

[5] A. Einstein, B. Podolsky, and N. Rosen. Can quantum-mechanical description of physical reality be considered complete? *Phys. Rev.*, 47:777–780, May 1935. DOI: 10.1103/PhysRev.47.777.

[6] J. S. Bell. On the einstein podolsky rosen paradox. *Physics Physique Fizika*, 1:195–200, Nov 1964. DOI: 10.1103/PhysicsPhysiqueFizika.1.195.

[7] B. Hensen, H. Bernien, A. E. Dréau, et al. Loophole-free bell inequality violation using electron spins separated by 1.3 kilometres. *Nature*, 526(7575):682–686, 2015. DOI: 10.1038/nature15759.

[8] M. Giustina, M. A. M. Versteegh, S. Wengerowsky, et al. Significant-loophole-free test of bell's theorem with entangled photons. *Phys. Rev. Lett.*, 115:250401, Dec 2015. DOI: 10.1103/PhysRevLett.115.250401.

[9] L. K. Shalm, E. Meyer-Scott, B. G. Christensen, et al. Strong loophole-free test of local realism. *Phys. Rev. Lett.*, 115:250402, Dec 2015. DOI: 10.1103/PhysRevLett.115.250402.

[10] W. Rosenfeld, D. Burchardt, R. Garthoff, et al. Event-ready bell test using entangled atoms simultaneously closing detection and locality loopholes. *Phys. Rev. Lett.*, 119:010402, Jul 2017. DOI: 10.1103/PhysRevLett.119.010402.

[11] R. P. Feynman. Simulating physics with computers. *International Journal of Theoretical Physics*, 21(6):467–488, 1982. DOI: 10.1007/BF02650179.

[12] D. Deutsch and R. Penrose. Quantum theory, the Church-Turing principle and the universal quantum computer. *Proceedings of the Royal Society of London. A. Mathematical and Physical Sciences*, 400(1818):97–117, 1985. DOI: 10.1098/rspa.1985.0070.

[13] P. W. Shor. Polynomial-time algorithms for prime factorization and discrete logarithms on a quantum computer. *SIAM Review*, 41(2):303–332, 1999. DOI: 10.1137/S0036144598347011.

[14] L. K. Grover. Quantum computers can search arbitrarily large databases by a single query. *Phys. Rev. Lett.*, 79:4709–4712, Dec 1997. DOI: 10.1103/PhysRevLett.79.4709.

[15] W. K. Wootters and W. H. Zurek. A single quantum cannot be cloned. *Nature*, 299(5886):802–803, 1982. DOI: 10.1038/299802a0.

[16] C. Bennett and G. Brassard. Quantum cryptography: Public key distribution and coin tossing. *International Conference on Computers, Systems & Signal Processing, Bangalore, India, Dec 9-12, 1984*, 560:175–179, Jan 1984. DOI: 10.1016/j.tcs.2011.08.039.

[17] E. SCHRÖDINGER. ARE THERE QUANTUM JUMPS ?: PART II*. *The British Journal for the Philosophy of Science*, III(11):233–242, Nov 1952. DOI: 10.1093/bjps/III.11.233.

[18] W. Neuhauser, M. Hohenstatt, P. E. Toschek, and H. Dehmelt. Localized visible ba^+ mono-ion oscillator. *Phys. Rev. A*, 22:1137–1140, Sep 1980. DOI: 10.1103/PhysRevA.22.1137.

[19] A. L. Migdall, J. V. Prodan, W. D. Phillips, T. H. Bergeman, and H. J. Metcalf. First observation of magnetically trapped neutral atoms. *Phys. Rev. Lett.*, 54:2596–2599, Jun 1985. DOI: 10.1103/PhysRevLett.54.2596.

[20] J. I. Cirac, P. Zoller, H. J. Kimble, and H. Mabuchi. Quantum state transfer and entanglement distribution among distant nodes in a quantum network. *Phys. Rev. Lett.*, 78:3221–3224, Apr 1997. DOI: 10.1103/PhysRevLett.78.3221.

[21] C. Nölleke, A. Neuzner, A. Reiserer, et al. Efficient teleportation between remote single-atom quantum memories. *Phys. Rev. Lett.*, 110:140403, Apr 2013. DOI: 10.1103/PhysRevLett.110.140403.

[22] S. Ritter, C. Nölleke, C. Hahn, et al. An elementary quantum network of single atoms in optical cavities. *Nature*, 484(7393):195–200, 2012. DOI: 10.1038/nature11023.

[23] M. Żukowski, A. Zeilinger, M. A. Horne, and A. K. Ekert. "event-ready-detectors" bell experiment via entanglement swapping. *Phys. Rev. Lett.*, 71:4287–4290, Dec 1993. DOI: 10.1103/PhysRevLett.71.4287.

[24] H. Bernien, B. Hensen, W. Pfaff, et al. Heralded entanglement between solid-state qubits separated by three metres. *Nature*, 497(7447):86–90, 2013. DOI: 10.1038/nature12016.

[25] P. Lodahl. Quantum-dot based photonic quantum networks. *Quantum Science and Technology*, 3(1):013001, Oct 2017. DOI: 10.1088/2058-9565/aa91bb.

[26] R. Valivarthi, M. l. G. Puigibert, Q. Zhou, et al. Quantum teleportation across a metropolitan fibre network. *Nature Photonics*, 10(10):676–680, 2016. DOI: 10.1038/nphoton.2016.180.

[27] X.-S. Ma, T. Herbst, T. Scheidl, et al. Quantum teleportation over 143 kilometres using active feed-forward. *Nature*, 489(7415):269–273, 2012. DOI: 10.1038/nature11472.

[28] S.-K. Liao, W.-Q. Cai, W.-Y. Liu, et al. Satellite-to-ground quantum key distribution. *Nature*, 549(7670):43–47, 2017. DOI: 10.1038/nature23655.

[29] J. Yin, Y. Cao, Y.-H. Li, et al. Satellite-based entanglement distribution over 1200 kilometers. *Science*, 356(6343):1140–1144, 2017. DOI: 10.1126/science.aan3211.

[30] German Federal Ministry of Education and Research (BMBF). The joint project quantum link extension (q.link.x). Url: `https://qlinkx.de`, `https://www.forschung-it-sicherheit-kommunikationssysteme.de/projekte/q-link.x`.

[31] M. Uphoff, M. Brekenfeld, G. Rempe, and S. Ritter. An integrated quantum repeater at telecom wavelength with single atoms in optical fiber cavities. *Applied Physics B*, 122(3):46, 2016. DOI: 10.1007/s00340-015-6299-2.

[32] H.-J. Briegel, W. Dür, J. I. Cirac, and P. Zoller. Quantum repeaters: The role of imperfect local operations in quantum communication. *Phys. Rev. Lett.*, 81:5932–5935, Dec 1998. DOI: 10.1103/PhysRevLett.81.5932.

[33] D. Kielpinski, C. Monroe, and D. J. Wineland. Architecture for a large-scale ion-trap quantum computer. *Nature*, 417(6890):709–711, 2002. DOI: 10.1038/nature00784.

[34] F. Arute, K. Arya, R. Babbush, et al. Quantum supremacy using a programmable superconducting processor. *Nature*, 574(7779):505–510, 2019. DOI: 10.1038/s41586-019-1666-5.

[35] H. J. Kimble. The quantum internet. *Nature*, 453(7198):1023–1030, 2008. DOI: 10.1038/nature07127.

[36] A. G. J. MacFarlane, J. P. Dowling, and G. J. Milburn. Quantum technology: the second quantum revolution. *Philosophical Transactions of the Royal Society of London. Series A: Mathematical, Physical and Engineering Sciences*, 361(1809):1655–1674, 2003. DOI: 10.1098/rsta.2003.1227.

[37] D. P. DiVincenzo. The physical implementation of quantum computation. *Fortschritte der Physik*, 48(9-11):771–783, Sep 2000. DOI: 10.1002/1521-3978(200009)48:9/11<771::aid-prop771>3.0.co;2-e.

[38] K. Redeker. Entanglement of single rubidium atoms: From a bell test towards applications. PhD thesis, Ludwig-Maximilians-Universität München, Feb 2020.

[39] D. A. Steck. Rubidium 87 d line data. Url: `https://steck.us/alkalidata/rubidium87numbers.1.6.pdf`, 2003.

[40] L. Ricci, M. Weidemüller, T. Esslinger, et al. A compact grating-stabilized diode laser system for atomic physics. *Optics Communications*, 117(5):541 – 549, 1995. DOI: 10.1016/0030-4018(95)00146-Y.

[41] N. Ortegel. State readout of single Rubidium-87 atoms for a loophole-free test of Bell's inequality. PhD thesis, Ludwig-Maximilians-Universität München, Aug 2016.

[42] K. Redeker. Detektion von Ionisationsfragmenten von Rb-87 Atomen. Diplomarbeit, Ludwig-Maximilians-Universität München, Sep 2012.

[43] C. J. Pethick and H. Smith. Bose–Einstein Condensation in Dilute Gases. Cambridge University Press, 2 edition, 2008. DOI: 10.1017/CBO9780511802850.

[44] S. Chu, L. Hollberg, J. Bjorkholm, A. Cable, and A. Ashkin. Three-dimensional viscous confinement and cooling of atoms by resonance radiation pressure. *Physical review letters*, 55:48–51, Aug 1985. DOI: 10.1103/PhysRevLett.55.48.

[45] E. L. Raab, M. Prentiss, A. Cable, S. Chu, and D. E. Pritchard. Trapping of neutral sodium atoms with radiation pressure. *Phys. Rev. Lett.*, 59:2631–2634, Dec 1987. DOI: 10.1103/PhysRevLett.59.2631.

[46] T. Hänsch and A. Schawlow. Cooling of gases by laser radiation. *Optics Communications*, 13(1):68 – 69, 1975. DOI: 10.1016/0030-4018(75)90159-5.

[47] P. Koschmieder. Efficient control of magnetic fields in single atom experiments. Master's thesis, Ludwig-Maximilians-Universität München, Feb 2019.

[48] D. Burchardt. A rigorous test of bell's inequality and quantum teleportation employing single atoms. PhD thesis, Ludwig-Maximilians-Universität München, Dec 2017.

[49] J. Dalibard and C. Cohen-Tannoudji. Laser cooling below the doppler limit by polarization gradients: simple theoretical models. *J. Opt. Soc. Am. B*, 6(11):2023–2045, Nov 1989. DOI: 10.1364/JOSAB.6.002023.

[50] J. Volz. Atom-photon entanglement. PhD thesis, Ludwig-Maximilians-Universität München, Mar 2006.

[51] M. Weber. Quantum optical experiments towards atom-photon entanglement. PhD thesis, Ludwig-Maximilians-Universität München, Jun 2005.

[52] C. Gerry and P. Knight. Introductory Quantum Optics. Cambridge University Press, 2004. DOI: 10.1017/CBO9780511791239.

[53] S. Chu, J. E. Bjorkholm, A. Ashkin, and A. Cable. Experimental observation of optically trapped atoms. *Phys. Rev. Lett.*, 57:314–317, Jul 1986. DOI: 10.1103/PhysRevLett.57.314.

[54] R. Grimm, M. Weidemüller, and Y. B. Ovchinnikov. Optical dipole traps for neutral atoms. volume 42 of *Advances In Atomic, Molecular, and Optical Physics*, pages 95 – 170. Academic Press, 2000.

[55] T. Hummel. Increasing photon collection efficiency for generating long-distance entanglement of atoms. Master's thesis, Ludwig-Maximilians-Universität München, Oct 2018.

[56] N. Schlosser, G. Reymond, I. Protsenko, and P. Grangier. Sub-poissonian loading of single atoms in a microscopic dipole trap. *Nature*, 411(6841):1024–1027, 2001. DOI: 10.1038/35082512.

[57] N. Schlosser, G. Reymond, and P. Grangier. Collisional blockade in microscopic optical dipole traps. *Phys. Rev. Lett.*, 89:023005, Jun 2002. DOI: 10.1103/PhysRevLett.89.023005.

[58] J. Volz, M. Weber, D. Schlenk, et al. Observation of entanglement of a single photon with a trapped atom. *Phys. Rev. Lett.*, 96:030404, Jan 2006. DOI: 10.1103/PhysRevLett.96.030404.

[59] J. Hofmann. Heralded atom-atom entanglement. PhD thesis, Ludwig-Maximilians-Universität München, Oct 2014.

[60] F. Henkel, M. Krug, J. Hofmann, et al. Highly efficient state-selective submicrosecond photoionization detection of single atoms. *Phys. Rev. Lett.*, 105:253001, Dec 2010. DOI: 10.1103/PhysRevLett.105.253001.

[61] F. Henkel. Photoionisation detection of single Rb-87 atoms using channel electron multipliers. PhD thesis, Ludwig-Maximilians-Universität München, Sep 2011.

[62] M. Krug. Ionization Based State Read Out of a single Rb-87 Atom. PhD thesis, Ludwig-Maximilians-Universität München, Dec 2018.

[63] J.-W. Pan, D. Bouwmeester, H. Weinfurter, and A. Zeilinger. Experimental entanglement swapping: Entangling photons that never interacted. *Phys. Rev. Lett.*, 80:3891–3894, May 1998. DOI: 10.1103/PhysRevLett.80.3891.

[64] C. K. Hong, Z. Y. Ou, and L. Mandel. Measurement of subpicosecond time intervals between two photons by interference. *Phys. Rev. Lett.*, 59:2044–2046, Nov 1987. DOI: 10.1103/PhysRevLett.59.2044.

[65] W. Rosenfeld. Experiments with an entangled system of a single atom and a single photon. PhD thesis, Ludwig-Maximilians-Universität München, Sep 2008.

[66] R. Dorn, S. Quabis, and G. Leuchs. The focus of light - linear polarization breaks the rotational symmetry of the focal spot. *Journal of Modern Optics*, 50, May 2003. DOI: 10.1080/09500340308235246.

[67] E. Wolf and D. Gabor. Electromagnetic diffraction in optical systems - i. an integral representation of the image field. *Proceedings of the Royal Society of London. Series A. Mathematical and Physical Sciences*, 253(1274):349–357, 1959. DOI: 10.1098/rspa.1959.0199.

[68] B. Richards, E. Wolf, and D. Gabor. Electromagnetic diffraction in optical systems, ii. structure of the image field in an aplanatic system. *Proceedings of the Royal Society of London. Series A. Mathematical and Physical Sciences*, 253(1274):358–379, 1959. DOI: 10.1098/rspa.1959.0200.

[69] D. Taray. Towards increasing atomic coherence times with a standing wave dipole trap. Master's thesis, Ludwig-Maximilians-Universität München, May 2020.

[70] N. Shebani and S. Albouch. Estimation of the bending and scattering loss in single mode fiber based on the variation in operating wavelength, core radius and curvature of the fiber. Apr 2017.

[71] T. van Leent, M. Bock, R. Garthoff, et al. Long-distance distribution of atom-photon entanglement at telecom wavelength. *Phys. Rev. Lett.*, 124:010510, Jan 2020. DOI: 10.1103/PhysRevLett.124.010510.

[72] W. Demtröder. Experimentalphysik 3, volume 5. Springer International Publishing, 2016.

[73] I. V. Hertel and C.-P. Schulz. Atome, Moleküle und optische Physik 1. Springer International Publishing, 2008.

[74] W. Nolting. Theoretical Physics 3, volume 1. Springer International Publishing, 2016.

[75] J. D. Jackson. Classical electrodynamics. Wiley, New York, NY, 3rd ed. edition, 1999.

[76] K. Zimmerman. Developing the rendering equations. Url: https://www.cs.princeton.edu/courses/archive/fall10/cos526/papers/zimmerman98.pdf, 2010.

[77] M. Wilson. Collecting light: The importance of numerical aperture in microscopy. Url: https://www.leica-microsystems.com/science-lab/collecting-light-the-importance-of-numerical-aperture-in-microscopy/, Jul 2017.

[78] N. C. Schmidt, M. Kahms, J. Hüve, and J. Klingauf. Intrinsic refractive index matched 3d dstorm with two objectives: Comparison of detection techniques. *Scientific Reports*, 8(1):13343, 2018. DOI: 10.1038/s41598-018-31595-z.

[79] K. Kawano and T. Kitoh. Introduction to Optical Waveguide Analysis. John Wiley & Sons, Ltd, 2002. DOI: 10.1002/0471221600.ch2.

[80] D. Keffer. Numerical Techniques for the Evaluation of Multi-Dimensional Integral Equations. University of Tennessee, Sep 1999.

[81] L. J. Stephenson, D. P. Nadlinger, B. C. Nichol, et al. High-rate, high-fidelity entanglement of qubits across an elementary quantum network. *Phys. Rev. Lett.*, 124:110501, Mar 2020. DOI: 10.1103/PhysRevLett.124.110501.

[82] Schott AG. Optical glass, data sheets. Url: https://www.schott.com/d/advanced_optics/ac85c64c-60a0-4113-a9df-23ee1be20428/1.1/schott-optical-glass-collection-datasheets-english-17012017.pdf.

[83] P. L. von Seidel. Ueber die Theorie der Fehler, mit welchen die durch optische Instrumente gesehenen Bilder behaftet sind, und über die mathematischen Bedingungen ihrer Aufhebung. Abhandlungen der Naturwissenschaftlich-Technischen Commission bei der Königl. Bayerischen Akademie der Wissenschaften in München. Cotta, 1857.

[84] H. Gross. Handbook of Optical Systems, volume 3: Aberration Theory and Correction of Optical Systems. WILEY-VCH, 2006.

[85] H. Gross. Handbook of Optical Systems, volume 1: Fundamentals of Technical Optics. WILEY-VCH, 2005.

[86] R. R. Shannon and J. C. Wyant. Applied optics and optical engineering, volume XI. Academic Press, 1992.

[87] R. Barakat. Rayleigh wavefront criterion. *J. Opt. Soc. Am.*, 55(5):572–573, May 1965. DOI: 10.1364/JOSA.55.000572.

[88] R. J. Noll. Zernike polynomials and atmospheric turbulence∗. *J. Opt. Soc. Am.*, 66(3):207–211, Mar 1976. DOI: 10.1364/JOSA.66.000207.

[89] E. Hecht. Optics. Pearson, 2012.

[90] J. Alda. Laser and gaussian beam propagation and transformation. *Encyclopedia of Optical Engineering*, Jan 2003.

[91] H. Gross. Handbook of Optical Systems. WILEY-VCH, 2006.

[92] H. Gross. Imaging and aberration theory, lecture 12: Point spread function. Url: `https://www.iap.uni-jena.de/iapmedia/de/Lecture/Imaging+and+aberration+theory1583017200/IAT19_Imaging+and+Aberration+Theory+Lecture+13+Point+spread+functioin.pdf`, Jan 2020.

[93] M. Gu. Advanced Optical Imaging Theory. Springer International Publishing, 2000.

[94] S.-U. Hwang and Y.-G. Lee. Simulation of an oil immersion objective lens: A simplified ray-optics model considering abbe's sine condition. *Opt. Express*, 16(26):21170–21183, Dec 2008. DOI: 10.1364/OE.16.021170.

[95] J. H. Burge, C. Zhao, and M. Dubin. Use of the abbe sine condition to quantify alignment aberrations in optical imaging systems. In *International Optical Design Conference and Optical Fabrication and Testing*, page ITuD5. Optical Society of America, 2010. DOI: 10.1364/IODC.2010.ITuD5.

[96] J. A. Veerman, M. F. Garcia-Parajo, L. Kuipers, and N. F. Van Hulst. Single molecule mapping of the optical field distribution of probes for near-field microscopy. *Journal of Microscopy*, 194(23):477–482, 1999. DOI: 10.1046/j.1365-2818.1999.00520.x.

[97] C. Obermüller and K. Karrai. Far field characterization of diffracting circular apertures. *Applied Physics Letters*, 67(23):3408–3410, 1995. DOI: 10.1063/1.115262.

[98] C. Obermüller, K. Karrai, G. Kolb, and G. Abstreiter. Transmitted radiation through a subwavelength-sized tapered optical fiber tip. *Ultramicroscopy*, 61(1):171 – 177, 1995. DOI: 10.1016/0304-3991(95)00128-X. Selected Papers from the 3rd International Conference on Near-Field Optics and Related Techniques.

[99] C. Robens, S. Brakhane, W. Alt, et al. High numerical aperture (NA = 0.92) objective lens for imaging and addressing of cold atoms. *Opt. Lett.*, 42:1043, 2017.

[100] C. Robens. Testing the Quantumness of Atom Trajectories. PhD thesis, Universität Bonn, 2017.

[101] J. Weiner. The physics of light transmission through subwavelength apertures and aperture arrays. *Reports on Progress in Physics*, 72(6):064401, May 2009. DOI: 10.1088/0034-4885/72/6/064401.

[102] L. Martín-Moreno, F. J. García-Vidal, H. J. Lezec, A. Degiron, and T. W. Ebbesen. Theory of highly directional emission from a single subwavelength aperture surrounded by surface corrugations. *Phys. Rev. Lett.*, 90:167401, Apr 2003. DOI: 10.1103/PhysRevLett.90.167401.

[103] N. C. Lindquist, P. Nagpal, K. M. McPeak, D. J. Norris, and S.-H. Oh. Engineering metallic nanostructures for plasmonics and nanophotonics. *Reports on Progress in Physics*, 75(3):036501, feb 2012. DOI: 10.1088/0034-4885/75/3/036501.

[104] A. Alberti, C. Robens, W. Alt, et al. Super-resolution microscopy of single atoms in optical lattices. *New J. Phys.*, 18:053010, 2016.

[105] R. van den Boomgaard. Lecture Notes: Image Processing. Url: `https://staff.fnwi.uva.nl/r.vandenboomgaard/IPCV20172018/LectureNotes/IP/LocalOperators/percentilefilter.html`, 2017.

[106] M. Araújo, R. Silva, E. Lima, D. Pereira, and P. De Oliveira. Measurement of gaussian laser beam radius using the knife-edge technique: Improvement on data analysis. *Applied optics*, 48:393–6, Feb 2009. DOI: 10.1364/AO.48.000393.

[107] P. Marchenko, S. Orlov, C. Huber, et al. Interaction of highly focused vector beams with a metal knife-edge. *Opt. Express*, 19(8):7244–7261, Apr 2011. DOI: 10.1364/OE.19.007244.

[108] W. T. Welford. Aberrations of Optical Systems. CRC Press, 1986.

[109] H. Gross. Imaging and aberration theory, lecture 12: Zernike polynomials. Url: `https://www.iap.uni-jena.de/iapmedia/Lecture/Imaging+and+aberration+theory1583017200/IAT19_Imaging+and+Aberration+Theory+Lecture+12+Zernike+polynomials.pdf`, Jan 2020.

Erklärung zur Masterarbeit

Hiermit erkläre ich, die vorliegende Masterarbeit selbständig verfasst zu haben und keine anderen als die in der Arbeit angegebenen Quellen und Hilfsmittel benutzt zu haben.

München, den 13.06.2020

(Matthias Manfred Seubert)